In Vitro Cell Irradiation with Low Energy Protons

DNA Double Strand Break Induction and Repair Kinetics in Human Glioblastoma Cells

Agnes Baker

A Thesis presented for the degree of
Master of Science

Department of Physics
Faculty of Mathematics and Natural Sciences
University of Oslo
Norway

June 2018

Abstract

Traditionally treatment of cancer has been delivered using high energy x-rays, but an increasing number of proton therapy centers are being built worldwide. Due to its relatively recent introduction to clinical practice, it is necessary to further develop our understanding of this treatment technique.

This study investigates the effects of high and low LET protons on T98G brain cancer (glioblastoma multiforma) cells. The main objectives of the present cell irradiation experiments have been to study the mechanisms underlying the known survival data. This has been done by recording the amount of unrepaired DNA double strand breaks (DSBs) as a function of time after irradiation.

Irradiations of the cells were performed at Oslo Cyclotron Laboratory using a 16 MeV proton beam. These were done using three different positions, with varying LET values, along the proton track. These results were also compared to 220 kV x-ray irradiations of the same doses. Two flow cytometry cell assays were used in the analysis of these cells, γH2AX in order to detect DNA DSBs and Annexin-V as a marker for apoptosis detection. The experimental procedure for γH2AX cell assay was adapted over the course of this project in order to optimise the detection of DNA DSBs, while it was found that this cell line does not undergo apoptosis.

As expected, T98G cells showed increased levels of phosphorylation after high LET irradiation compared to low LET irradiation at the same doses. From these findings, an RBE value of at least 4.4 was found to describe the differences in effect seen by irradiation in the back of the Bragg peak compared to the top. A ratio for the amount of damage induced for high LET irradiation compared to low LET irradiation was also found. After 5 Gy this was found to be 2.6 ± 0.5 compared to 2.8 ± 0.6 for 10 Gy. These values demonstrate how much more damage is induced by the higher LET in the back of the Bragg peak compared to the front of the Bragg peak.

An unexpected finding was an increase in γH2AX fluorescence seen at 72 hours. The potential reasons behind this are discussed. Flow cytometric analysis of the DNA content in the different phases of the cell cycle revealed a distinct arrest of cells in G2 phase at 24 hours post irradiation. This was particularly significant for

cells irradiated with higher LET values.

Declaration

The work in this thesis is based on research carried out in collaboration between the Biophysics and Medical Physics and Nuclear Physics research groups, within the Department of Physics. No part of this thesis has been submitted elsewhere for any other degree or qualification and it is all my own work unless referenced to the contrary in the text.

Acknowledgements

First, I would like to thank my supervisors Nina F. Edin, Eirik Malinen and Sunniva Siem for their professional guidance throughout this project. Particular thanks to Nina F. Edin for all of her help, support and insight during both experiments and writing.

Thanks also to Joe A. Sandvik for his assistance and expertise in Laboratory techniques and the engineers at Oslo Cyclotron Laboratory for their help setting up the cyclotron. I would also like to thank Anne Marit Rykkelid whose help and company during experiments and data analysis have been greatly appreciated.

Finally, thanks to all at the Biophysics and Medical Physics group for an inspiring two years. Special thanks to Ole Gunnar Johansen, Eirik Ramsli Hauge, Tore Hoeiland and Joakim Kalsnes for all of the quiz breaks and great company.

Contents

Abstract **iii**

Declaration **v**

Acknowledgements **vi**

1 Introduction **1**

2 Theory **4**

2.1 Cell Biology 4

2.1.1 Cell Cycle Regulation 6

2.2 Radiation Therapy 7

2.2.1 Radiation Physics 9

2.2.2 Ionising Radiation Devices 9

2.2.3 Dose Calculations 13

2.2.4 X-rays 14

2.2.5 Protons 16

2.2.6 LET and RBE 19

2.2.7 Dosimetry 20

2.3 Radio-biology 22

2.3.1 Direct and Indirect Action of Radiation 22

2.3.2 Radiation Damage & Repair 24

2.3.3 Repair Kinetics 26

2.3.4 Tumour biology 27

2.3.5 Dose-Survival Measurements 28

2.4 Methods of Analysis . . . 30
  2.4.1 Flow Cytometry . . . 30
  2.4.2 Cell assays . . . 32

3 Materials and Methods 35

3.1 Materials . . . 35
3.2 The Cell Line . . . 35
  3.2.1 Cell cultivation . . . 35
  3.2.2 Maintenance of the Cell Line . . . 37
3.3 Experimental Procedure . . . 38
  3.3.1 Preparations . . . 38
  3.3.2 Irradiation . . . 39
  3.3.3 Incubation and Fixation . . . 43
  3.3.4 Flow Cytometry . . . 43
  3.3.5 γH2AX Assay . . . 44
  3.3.6 Presentation of Data . . . 48

4 Results 50

4.1 Developing Method . . . 50
  4.1.1 Cell Seeding . . . 50
  4.1.2 Preparation . . . 50
  4.1.3 Irradiation . . . 51
  4.1.4 Flow Cytometry Assays . . . 52
4.2 Results . . . 53
  4.2.1 DSB Measurements . . . 54
  4.2.2 γH2AX Fluorescence . . . 55
  4.2.3 γH2AX Fluorescence per Gy . . . 57
  4.2.4 Apoptosis Measurements . . . 62
4.3 Additional Experimental Results . . . 64

5 Discussion 67

5.1 Methodological Considerations . . . 67

5.1.1 Cellular Variations 67
5.1.2 Proton Irradiations 68
5.1.3 Flow Cytometer Assays 71
5.2 γH2AX experiment results 73
5.2.1 Initial γH2AXluorescence (0.5 hours) 73
5.2.2 γH2AX Fluorescence at 24 Hours 76
5.2.3 γH2AX Fluorescence at 48 Hours 76
5.2.4 γH2AX Fluorescence at 72 Hours 76
5.2.5 Peak Width and Skewness 78
5.2.6 Cell cycle arrest 80
5.3 Apoptosis experiment results 81
5.4 Data Analysis 82
5.4.1 Flow Cytometry Analysis 82
5.4.2 LET and RBE 82
5.4.3 Cell Survival 84
5.4.4 Future Considerations 85

6 Conclusion **87**

Appendix **98**

A Method **98**

A.1 γH2AX Assay 98
A.2 Apoptosis Assay 99
A.3 Cell Barcoding 100

B Additional Results **102**

C Annexin V-FITC Assay **104**

D Dosimetry **107**

D.1 Finding the Bragg peak 108

Chapter 1

Introduction

There are a wide range of curative and palliative treatments for cancer patients, used alone or as combined treatments and these include surgery, chemotherapy, immunotherapy and radiation therapy. Radiation therapy is widely used to both control and treat tumours, with the most common type of radiation being high energy x-rays. This type of RT has been around for a long period of time and clinical outcomes and effectiveness are now well known through large amounts of clinical data.

Proton therapy however, due to its relatively recent introduction to clinical practice [1], has a somewhat limited amount of clinical data compared to other therapies. With the increasing number of clinical proton centres being built, it is necessary to develop a greater understanding of this treatment through research [1]. Through studies into the effects of protons, on both normal and tumour cells, it is possible to determine the benefits and risks associated with this treatment. Such studies will also be an invaluable resource for patient treatment planning and the subsequent results obtained.

Compared to X-rays, which distribute their dose uniformly along their path through matter, protons have a much more defined distribution. Depositing the vast majority of their energy in a very specific region, called the Bragg peak, with no distal dose after this. It is due to this dose distribution that proton therapy can be used to deliver an appropriate dose to the tumour while sparing the surrounding healthy tissue and organs at risk.

The highly precise dose distribution makes proton therapy a seemingly ideal treatment for tumours located in sensitive areas [2, 3]. One key example is brain tumours, where the risk of damage to neurologically active regions is an extremely important consideration. Proton therapy has already become a widely used method of treatment for such tumours [4], the most common and aggressive of which is glioblastoma multiforme [5].

Cells from this type of tumour, from the T98G cell line, have been used previously in studies at the University of Oslo Biophysics department. The results of these studies have shown the greatly varying Relative Biological Effectiveness (RBE) values produced from irradiating with different positions along the proton track. It was found that the RBE of protons varied from 2.3 before the Bragg peak to between 4 and 10 in the back of the Bragg peak [6]. These are all significantly greater than the value of 1.1 being used clinically today [7]. It is important to note the much higher energy of clinical beams (80 - 230 MeV [NHS, 2018]) to those used in this study (16 MeV). The LET values of the low energy beam used are much higher than the values seen clinically and will therefore be expected to produce higher levels of damage in the cells studied. However, the relationship between the high LET and low LET effects produced will be relevant. It is these effects which could have a serious impact upon patient results.

Developing our understanding of the damage and repair undergone in these cells, will ultimately improve our understanding of the variable RBE values found. Being able to better predict the change in RBE with the different Linear Energy Transfer (LET) values could allow for improved treatment planning for patients. This will be further investigated in this thesis, by looking at the mechanisms of cell damage and repair after proton and x-ray irradiation. For both proton and x-ray irradiation the induction of DNA double strand breaks (DSBs) and apoptosis will be compared for different doses. The repair of the irradiated cells after different time points will also be looked at, in relation to the known survival outcomes.

The aim of this work is to gain a greater insight into the effects of varying proton LET on the survival mechanisms of T98G cells. Being able to more accurately describe the relative effects of protons in comparison to x-rays will ideally lead to improved patient outcomes and more efficient clinical treatments.

Chapter 2

Theory

2.1 Cell Biology

The organisation of all living organisms begins with cells and their constituents. The survival of organisms, and the species to which they belong, is dependent upon the proliferation of cells and the transmission of the genetic information stored in the cell nucleus to their progeny.

This vital information is stored within DNA, a molecule consisting of two complementary polymer chains. These chains are built up of the same four nucleotides - Adenine, Thymine, Cytosine and Gunanine (A, T, C and G) - linked in varying sequences by a phosphate backbone. The base pairs of A and T, C and G are each attached by a phosphate group to a sugar (deoxyribose) as depicted in Figure 2.1.

The replication of DNA uses a single strand as a template, the second complementary strand is then built onto the original, running in the opposite direction. These two complete strands twist around one another to form the DNA double helix. This DNA helix is then tightly wound around histone proteins, this structure is termed a nucleosome which is condensed to form chromatin. It is these chromatin which make up chromosomes. It is vital that DNA is replicated accurately, as any deviation from the original code will lead to a mutation and possible loss of function. This can have lethal consequences for both the cell and the system to which it belongs.

Replication of DNA occurs in proliferating cells during the cell cycle. This cycle

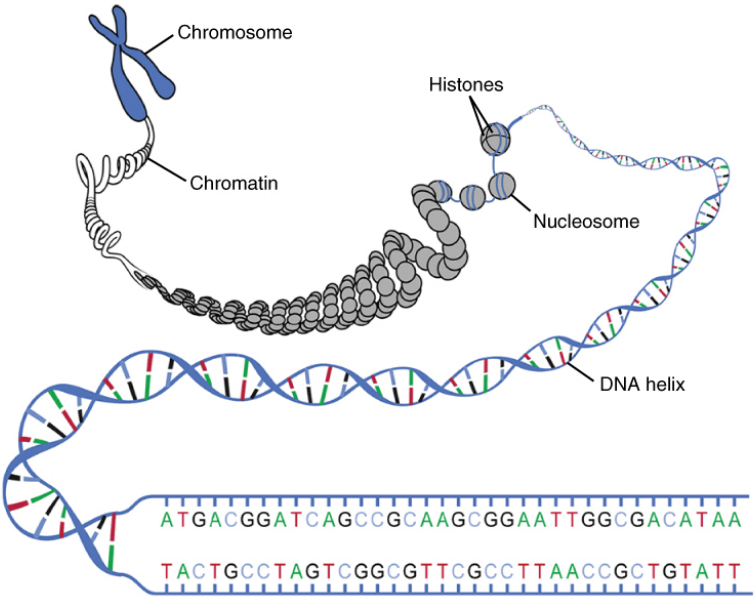

Figure 2.1: *Chromosome Macrostructure, showing chromatin, nucleosome, histones, the DNA double helix and the DNA bases (A, T, C and G) [8]*

is split into two stages, interphase during which the cell increases in size and its chromosomes are replicated and segregated, and mitosis, where the contents are then divided into two identical daughter cells. For eukaryotic cells, interphase can be further separated into G1, S and G2 phase. Figure 2.2 shows the detailed progression of a cell through the cell cycle. In G1, the contents of the cell is doubled, excluding chromosomes which are duplicated in S phase. During G2 phase, any damage or replication errors are checked for, thus providing a safety checkpoint for the cell as it prepares to go into mitosis.

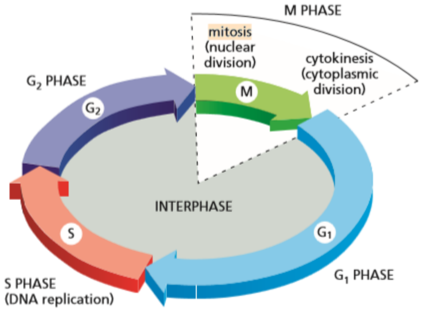

Figure 2.2: *Phases of the cell cycle [9]*

From G2 phase the cell then passes through to mitosis and onto cytokinesis. Mitosis can again be further divided into prophase, prometaphase, anaphase and telophase as shown in Figure 2.3. During prophase the centrosomes within the cell begin to move to separate sides of the cell while the duplicated chromosomes condense into chromatids. Attached to the centrosomes are microtubuli which become elongated during this phase and aid the cell division. During prometaphase the nuclear envelope becomes fragmented allowing the microtubule to attach to the chromatid within. Then, as the cell enters metaphase the chromatids become aligned along the centre of the cell before being drawn to opposite poles during anaphase. At this stage of anaphase the microtubule become shorter, as the duplicate sets of chromotids are separated. Finally, during telophase two nuclear envelopes are formed around the separated chromatids. Cytokinesis is then undergone as proteins called myosin and actin divide the cell into two identical daughter cells.

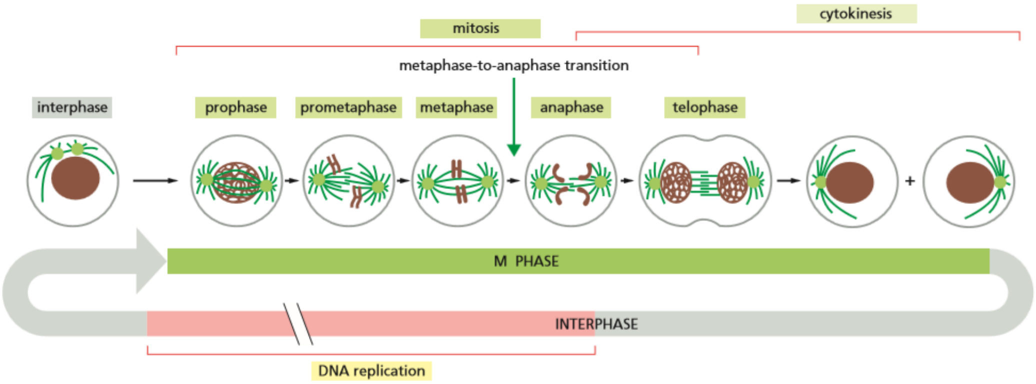

Figure 2.3: *Stages of Mitosis in the cell cycle [9]*

2.1.1 Cell Cycle Regulation

The entry to each phase of the cell cycle is regulated by a complex system of biochemical controls. These are able to delay or prevent the cell from passing from one phase to the next in the case of any detected malfunction or mutation. If any mutations occur during DNA synthesis, they must be repaired before the cell divides as these can lead to loss of function in the cell. Therefore, if a mutated cell is allowed to proliferate it can have serious implications for the organism as a whole.

There are three main transitions within the cell cycle where the cell either commits to it's progression or arrests the cell cycle. These are the start transition, situated at the end of G1 where, depending upon a favourable environment, the cell decides whether or not it should continue into the cell cycle. Second is the G2/M transition, located between the two phases, where the decision to enter mitosis is made. This transition depends on whether or not all of the DNA has been accurately replicated and again on a favourable environment. Finally the metaphase to anaphase transition, where if all the chromosomes are connected to the spindle, as seen in Figure 2.4a, the cell progresses to anaphase and ultimately cytokinesis.

Each of these transitions relies on cyclin dependent kinases (Cdks), which are phosphorylated and dephosphorylated at the various stages of the cell cycle. This activation of Cdks at various stages acts as transcription factors to express enzymes required for the next cell cycle phase. The activity of the Cdks is controlled by a number of enzymes and proteins, the most important proteins being cyclins. Cyclins are synthesised and degraded throughout the cell cycle while the Cdk levels remain constant. Cdks depend upon cyclins for activation. Figure 2.4b shows the rise and fall of the cyclins in relation to the progression of the cell throughout the cell cycle.

2.2 Radiation Therapy

Radiation therapy, or radiotherapy, is one of the main techniques used for the curative and palliative treatment of cancer. This form of treatment uses ionising radiation to deliver a dose to the tumour volume in order to induce irreparable damage and destroy the cancer cells. The treatment can be delivered using external beams of radiation, radioactive implants or injections. For radiation to be considered ionising it must have the ability to release a valence electron from the atom or molecule with which it is interacting.

The majority of clinical treatments use high energy x-rays. However, over the past few years proton therapy has become a more wide spread treatment option, with many countries investing in new proton therapy centres. Although the amount of clinical data for proton therapy is lacking compared to that available from x-ray treatments, a large amount of research has been built up, showing the benefits of the more specific dose distribution afforded by protons.

Prior to treatment, detailed plans are made in order to map the dose distribution

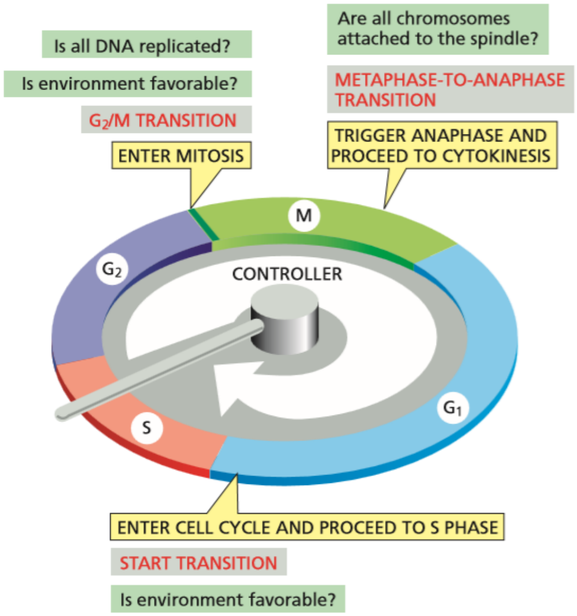

(a) *Cell cycle checkpoints*

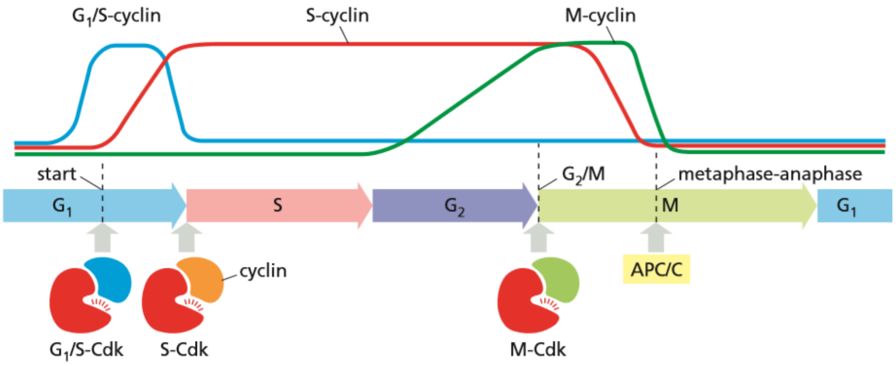

(b) *Cyclin variations during cell cycle*

Figure 2.4: *Cell cycle checkpoints [9]*

within the patient. Using the spread out Bragg peak technique, a succession of proton beams, beginning in the distal edge of the tumour and moving forward, are used to irradiated the whole tumour volume with maximum dose [10]. An ideal treatment provides maximum tumour control while sparing the surrounding tissues and organs from harm. Therefore plans must take into account tumour size, volume and aggressiveness as well as location and position within the patient. The sensitivity and potential long term effects of all surrounding tissues, organs and structures at risk must also be considered. The lack of clinical data available for proton therapy is a limiting factor for dose planning, making research in this area particularly valuable. In order to produce accurate dose plans, the interactions and effects of protons within the body must be fully understood.

2.2.1 Radiation Physics

For the work done in this thesis, two types of radiation were used. Cells were irradiated with 220 kV x-rays and 16 MeV protons. These fall into the two categories of radiation - indirectly and directly ionising. Indirectly ionising radiation, such as x-rays and neutrons, transfer relatively large amounts of their energy to secondary charged particles through a few interactions. It is these secondary charged particles, typically electrons, which then go on to cause an ionisation close to the initial interaction site.

Directly ionising radiation interacts with matter through a large number of small coulomb interactions. These interactions will be described in further detail in Sections 2.2.4 and 2.2.5 for x-rays and protons respectively.

2.2.2 Ionising Radiation Devices

Clinically there are a number of devices used for the acceleration of ionising radiation which can be used for both research purposes and clinically to treat patients. For the delivery of high energy x-rays or electrons a linear accelerator (LINAC) is the most common clinical device. However, for this research the x-rays were produced using a simple x-ray tube and the high energy proton beams were produced by the MC-35 Scanditronix cyclotron at OCL.

2.2.2.1 X-ray Tube

An example schematic diagram of a typical tube is as shown in Figure 2.5. A spectrum of x-rays is produced after thermionic electrons released from the cathode are accelerated through the evacuated tube and interact with the anode. Both the cathode and anode are typically made of Tungsten, due to its high heat capacity and atomic number which increases the likelihood of interaction.

The two types of x-rays being released are characteristic and bremsstrahlung x-rays. Bremsstrahlung x-rays, accounting for around 80% of x-rays produced, are

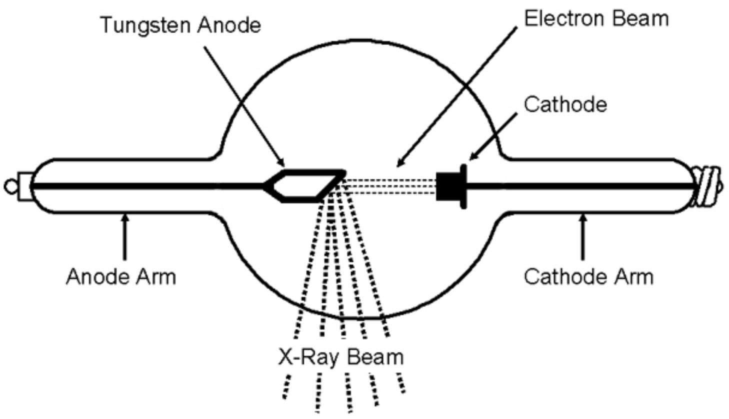

Figure 2.5: *Schematic diagram of the components of an x-ray tube [11]*

created when electrons interact with the nuclei of atoms. In the presence of the nucleus the electrons slow down and change direction, losing energy which is released as bremsstrahlung radiation. Due to the energy spectrum of these produced x-rays, filtration of the beam is required in order to produce a more even dose distribution. The effects of this filtration are as demonstrated in Figure 2.6.

Characteristic radiation is x-rays emitted after an atomic electron transitions between lower atomic energy levels. This occurs after an incoming electron transfers enough energy to an atomic electron to enable its release from the atom. The atom then de-excites from this unstable state via an outer shell electron transitioning down to fill the hole left behind. In order to conserve energy, the binding energy difference between the two shells is then emitted as a photon. Figure 2.6 shows the distinct peaks produced by characteristic x-rays along with the continuous spectrum produced by bremsstrahlung x-rays.

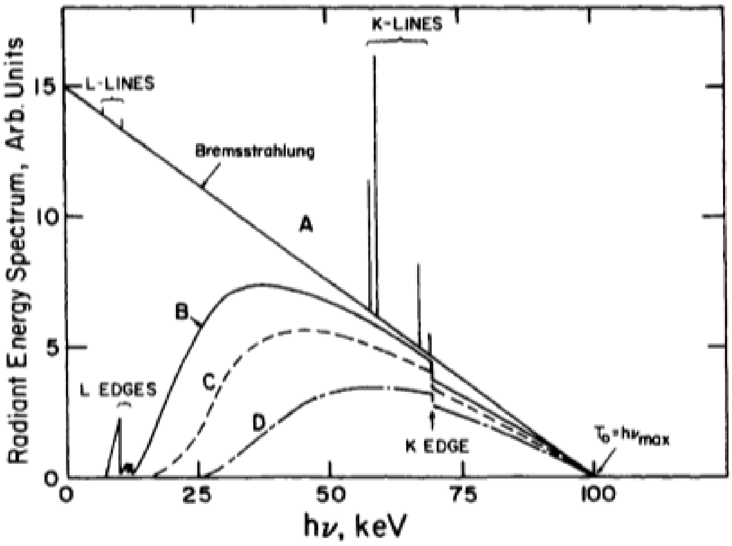

Figure 2.6: *Typical x-ray spectra produced by 100 keV electrons, with increasing levels on filtration from A - D. A: Unfiltered. B: Filtered through 0.01 mm W in escaping the target. C: Additionally filtered through 2 mm Al. D: Filtered through 0.15 mm Cu and 3.9 mm A1 in addition to inherent target filtration. To avoid confusion, the K-fluorescence lines are not shown in curves B, C, and D, but are attenuated from their heights in curve A in the same proportion as the bremsstrahlung is attenuated at the same energies. [12]*

2.2.2.2 LINAC

For treatment of patients with high energy x-rays, it is most likely that a Linear Accelerator, or LINAC, will be used. LINACs are used clinically to produce both beams of high energy electrons and x-rays. Figure 2.7 shows an example of the components of a typical LINAC. Electrons are released from an electron gun at intervals timed with the production of RF waves from a Magnetron or Klysotron. The electrons then gain energy from the waves as they are accelerated along the gantry of the machine. Bending magnets are used to create a homogeneous beam in the direction of the treatment table. With the use of a target, such as Tungsten, this electron beam can then be converted into one of high energy x-rays.

2.2.2.3 Cyclotron

For the acceleration of heavy charged particles, particularly protons for clinical purposes, a cyclotron is used. Figure 2.8 shows an example of the various components of a cyclotron. The applied magnetic field ensures that the particles follow a circular

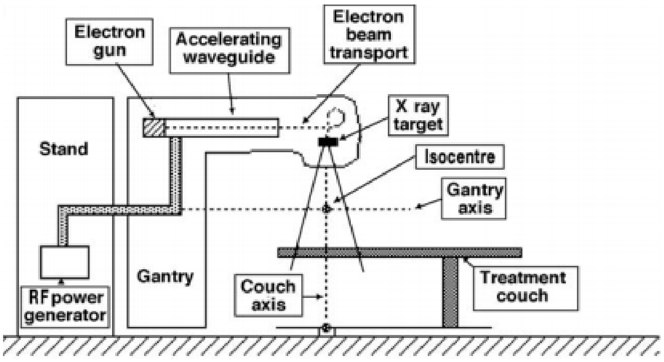

Figure 2.7: *Schematic diagram showing the components of a clinical LINAC [13]*

path through the electrode before being accelerated across the gap. This acceleration is induced by an alternating electric field applied to the two dees. This field is timed with the phase of the cyclotron to ensure the particles are constantly accelerated across the gap. The spiral path of the particle, as seen in Figure 2.8 is caused by the angular frequency, qB/m, of the applied electric field.

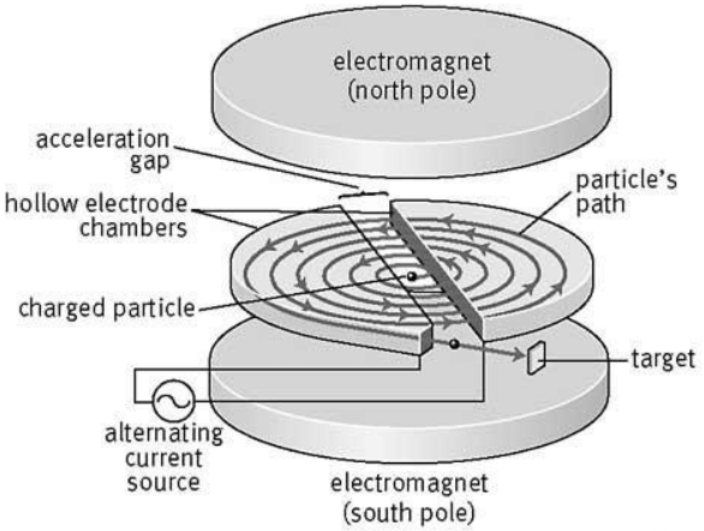

Figure 2.8: *Schematic diagram of a cyclotron [14]*

Once the particles have reached a maximum possible energy they are directed out of the cyclotron in the form of a beam. Sets of magnets are then used to shape and steer the beam before it is used. This aims to produce a homogeneous distribution of particles in the beam exiting the cyclotron.

2.2.3 Dose Calculations

Radiation therapy is planned around the desired outcomes or endpoints of the proposed treatment. Before treatment, detailed dose plans are created, taking into account tumour size, volume and aggressiveness. Also important are the location and position of the tumour, surrounding tissues, sensitive organs and structures at risk. These considerations will lead to the choice of ionising radiation to be used for treatment. It is therefore vital to understand the interactions of these types of radiation within matter. For optimum treatment planning and results, a detailed understanding both of the benefits and disadvantages of the type of radiation being used is required. Due to the different characteristics and properties of the ionising radiation discussed, the transfer of energy and thus the delivered dose distributions vary greatly. This can be visualised in figure 2.9

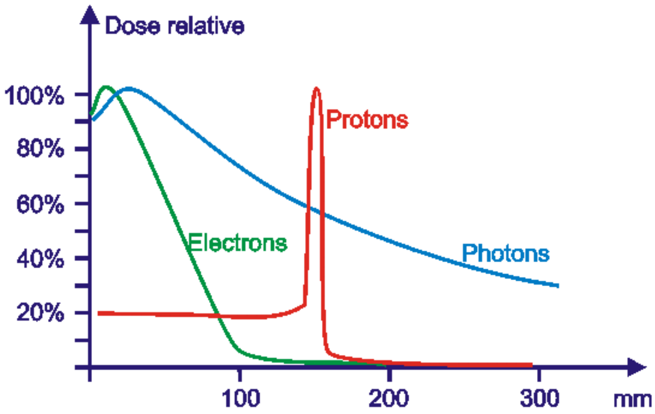

Figure 2.9: *Example plot of percentage dose distribution against depth for electrons, photons and protons. [15]*

This demonstrates the significant differences in the depth at which the maximum dose to matter is delivered by these three types of radiation. These dose depth distributions are dependent on the energy of the particles, which will be discussed further in Section 2.2.4 and 2.2.4.

The following sections will focus upon explaining the differences in dose distribution seen for photons and protons as it is these which will be investigated in this thesis. The interactions for both x-rays and protons in matter will be described, in relation to developing a calculation for the dose delivered to patients. The main source for information used for these calculations is an *Introduction to Radiological*

Physics and Radiation Dosimetry by Frank H. Attix. Finally, techniques for measuring these values will also be described, with regards to confirming the delivery of the desired dose.

Absorbed dose (eqn 2.2.1), the value of interest in most clinical treatments, is defined as the energy imparted (ϵ) per unit mass (m), as seen in equation 2.2.2. This is always specified at a particular point, P, within a finite volume, V.

$$D = \frac{d\epsilon}{dm} \tag{2.2.1}$$

$$\epsilon = ((R_{in})_u - (R_{out})_u + (R_{in})_c - (R_{out})_c + \Sigma Q, \tag{2.2.2}$$

where $(\mathrm{R}_{in})_u$ and $(\mathrm{R}_{out})_u$ are the total radiant energy of uncharged particles entering and leaving the volume, while $(\mathrm{R}_{in})_c$ and $(\mathrm{R}_{out})_c$ are the total radiant energy of charged particles entering and leaving the volume respectively. Finally, ΣQ is the net energy converted from mass within the volume, V.

Therefore, in order to calculate the dose delivered to matter it is vital to understand the mechanisms through which they transfer energy.

2.2.4 X-rays

The only way to distinguish x-rays from gamma rays is by understanding their origin. With equal energy they have identical properties, however gamma rays are the result of nuclear interactions while x-rays are emitted from the interactions of charged particles.

Photons undergo five types of interactions within matter; Compton scattering, photoelectric effect, pair production, Rayleigh scattering and photonuclear interactions. Of these, only the first three interactions listed will be described fully in this section. Rayleigh (coherent) scattering and photonuclear interactions do not result in a transfer of energy to electrons and will therefore be ignored.

As it is unlikely that the initial photon transfers all of its energy to the electron in the primary interaction, the incoming photon - now with reduced energy and altered direction - will go on to interact again. The number of interactions a photon undergoes, and the average amount of energy it loses per interaction, is dependent upon the interaction cross section of the material it is traversing and the initial photon energy.

Considering the main three interactions, it is possible to begin calculations towards the dose delivered to matter by photons. First, the mass energy transfer coefficient (eqn 2.2.3), describes how much energy equivalent mass is transferred to a medium. This is the sum of the energy equivalent mass transferred through each of the three main processes.

$$\frac{\mu_{tr}}{\rho} = \frac{\tau_{tr}}{\rho} + \frac{\sigma_{tr}}{\rho} + \frac{\kappa_{tr}}{\rho}\left(\frac{cm^2}{g}\right), \tag{2.2.3}$$

where $\frac{\mu_{tr}}{\rho}$ is the total value for the mass energy transfer cofficient and $\frac{\tau_{tr}}{\rho}$, $\frac{\sigma_{tr}}{\rho}$ and $\frac{\kappa_{tr}}{\rho}$ are the coefficients for photoelectric effect, Compton scattering and pair production interactions respectively.

If only the energy imparted within a volume is to be considered, any radiative losses by secondary electrons must be discounted from the total energy coefficient. This is done via the mass energy absorption coefficient (2.2.4). The average energy transferred to secondary electrons which go on to interact outside of the region of interest will result in a decreased amount of energy delivered. This value is defined as g and accounts for losses due to bremsstrahlung and in flight annihilation of positrons.

$$\frac{\mu_{en}}{\rho} = \frac{\mu_{tr}}{\rho}(1-g)\left(\frac{cm^2}{g}\right) \tag{2.2.4}$$

These values are dependent upon both the absorbing material and energy of the incoming particles. Therefore the next step is to consider both the energy and number of interacting photons, passing through the volume of interest.

The energy fluence of the beam, Ψ, is defined by the flux of the incoming beam, φ, multiplied by the energy of the particles. The total amount of energy, and thus the total dose delivered, will depend upon the number of photons interacting in that region and also their energy. Therefore, by multiplying the mass energy absorption coefficient by the fluence of the beam we can find the total value. The absorbed dose, D, delivered by particles of a specific energy is then defined by the energy fluence of the beam multiplied by the mass energy transfer coefficient of the particles, as shown below.

$$D = \frac{\mu_{en}}{\rho}\Psi\left(\frac{MeV}{g}\right) = 1.602 \times 10^{-10}\mu_{en}\rho(Gy) \tag{2.2.5}$$

Another quantity of interest for treatment planning is KERMA, the kinetic energy released per unit mass. This quantity is used during dosimetry in order to calculate the total amount of energy transferred within a volume. Unlike absorbed dose this includes energy which is later lost through radiative interactions. Therefore the total KERMA, K, is the sum of both collisional and radiative interactions as described in equation 2.2.6.

$$K = K_c + K_r \tag{2.2.6}$$

From this and equation 2.2.7 the dose delivered, D, can be shown to be equal to the collisional KERMA, K_c (eqn 2.2.8).

$$K = \frac{\mu_{tr}}{\rho}\Psi = D + \frac{\mu_{tr}}{\rho}g = D + K_r \tag{2.2.7}$$

$$D = K_c \tag{2.2.8}$$

2.2.5 Protons

Protons are a type of directly ionising radiation and exhibit a much more specific distribution of dose compared to x-rays and electrons. This distribution can be described using the varying linear energy transfer (LET) of protons. LET is the average amount of energy, dE, lost per unit path length, dx to the material which it is traversing (eqn 2.2.9). For protons this value increases with increasing distance travelled, which is why the majority of energy is lost to matter within the final Bragg peak of the curve as shown in Figure 2.9.

$$LET = \frac{dE}{dx} \tag{2.2.9}$$

Protons interact with atoms and molecules either through excitation or ionisation. The most important interaction for heavy charged particles (HCPs) occurs with electrons through Coulomb interactions. This is related to the impact parameter, b, which is the distance between the trajectory of the charged particle and the centre of the atomic nucleus as shown in figure 2.10.

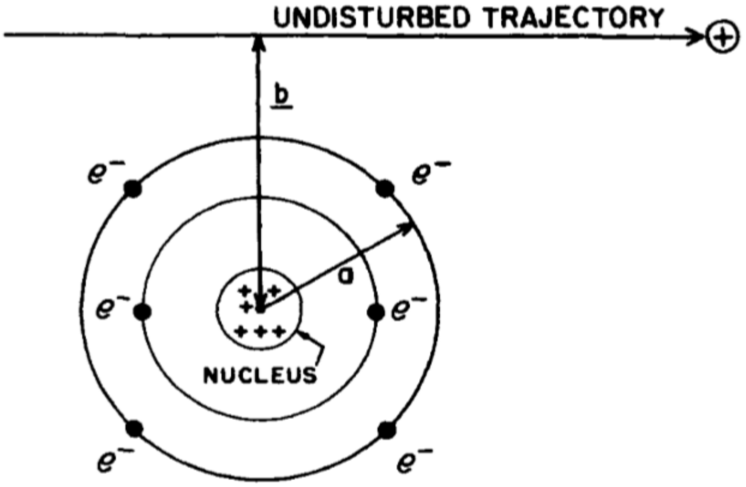

Figure 2.10: *Diagram demonstrating the collision of a charged particle with an atom. Showing impact parameter, b, and classical atomic radius, a.*

Considering the impact parameter, b, in relation to the atomic radius, a, it is possible to describe the collisions of particles in more detail. When $b >> a$ there is a large distance between the incoming particle and the nucleus of the atom. This interaction is considered a soft collision as there are only weak forces involved and a small energy transfer to the atom. Transferred energy is from Emin to H, where H is the maximum amount of energy transferred by soft collisions.

In cases where $b \approx a$, the charged particle effectively passes through the atom. This will result in large, but few, energy transfers. These are described to be between H up to Emax.

Therefore, in order to calculate the dose delivered to matter by HCPs such as protons, both soft and hard collisions must be taken into account. This is done by using the mass collision stopping power of the particles (eqn 2.2.10). This defines the rate at which particles lose energy due to both soft and hard collisions. This value is dependent on both the energy and type of the particles and the atomic composition of the material with which it is interacting.

$$\left(\frac{dT}{\rho dx}\right)_c = \left(\frac{dT_s}{\rho dx}\right)_c + \left(\frac{dT_h}{\rho dx}\right)_c \left(\frac{MeV}{cm}\right), \tag{2.2.10}$$

where dT is the amount of kinetic energy lost within a material of density ρ after travelling a distance dx. For heavy charged particles, such as protons, there are a number of corrections which must be made. Equation 2.2.11 shows the simplified mass collision stopping power for HCPs.

$$\left(\frac{dT}{\rho dx}\right)_c = 0.3071\frac{Zz^2}{A\beta^2}\left[13.8373 + ln\left(\frac{\beta^2}{1-\beta^2}\right) - \beta^2 - lnI - \frac{C}{Z}\right], \tag{2.2.11}$$

where Z and A are the atomic and mass numbers of the stopping medium respectively, z and β are the charge and relativistic velocity of the incoming particle, I is the mean excitation potential of the stopping material and $\frac{C}{Z}$ is the shell correction for the material.

As only collisional losses are of interest for heavy charged particles, the total stopping power may be simplified to the collisional stopping power (eqn 2.2.12). However, for light charged particles, such as electrons, radiative losses may occur due to bremsstrahlung production, and therefore the total stopping power must account for this (eqn 2.2.13). Total stopping power for HCPs:

$$HCP : \left(\frac{dT}{\rho dx}\right) \approx \left(\frac{dT}{\rho dx}\right)_c \tag{2.2.12}$$

Total stopping power for electrons:

$$e^- : \left(\frac{dT}{\rho dx}\right) = \left(\frac{dT}{\rho dx}\right)_c + \left(\frac{dT}{\rho dx}\right)_r \tag{2.2.13}$$

Finally, from these equations for the stopping power of particles, as described previously, it is possible to define an equation for the dose delivered. The energy deposited by the particles in the stopping medium will be dependent upon both the stopping power and also the fluence φ of the beam, as shown in equation 2.2.14.

$$D = \varphi \times \left(\frac{dT}{\rho dx} \right) \tag{2.2.14}$$

2.2.6 LET and RBE

In order to determine the quality of a type of radiation and its suitability for use, in a radiobiological sense, we can use values for LET and in turn the Relative Biological Effectiveness (RBE).

The LET of ionising radiation is defined as the average energy lost per distance traversed in a material (eqn 2.2.9). These values vary greatly depending upon the interactions undergone by the radiation in matter. Some common values of LET for different particles are shown in table 2.2.6 below.

Radiation	LET (keV/μm)
Cobalt-60 γrays	0.2
250 kV x-rays	2.0
10 MeV protons	4.7
150 MeV protons	0.5

From this it can be seen that LET decreases with increasing charged particle energy. For protons, LET also varies greatly along their path through matter, increasing with increasing distance traversed. This can be seen in figure 2.11, showing a typical variation of LET values. Using values obtained from Monte Carlo simulations along the central axis of the beam a variation of 0.8 - 0.9 keV/μm before the Bragg peak, 4.3 keV/μm in the top of the Bragg peak and 16 - 17 keV/μm in the back of the Bragg peak can be seen for 160 MeV protons [16].

Given the different interactions and effects as described, to be able to compare radiation types clinically, the endpoints of treatment are used. For this, values for RBE are used (eqn 2.2.15). The RBE is a value which allows the comparison of the absorbed dose of reference radiation (typically 250kV x-rays) compared to the absorbed dose of test radiation required to achieve the same biological outcome. It is therefore possible to compare the effects of, for example, x-rays and protons.

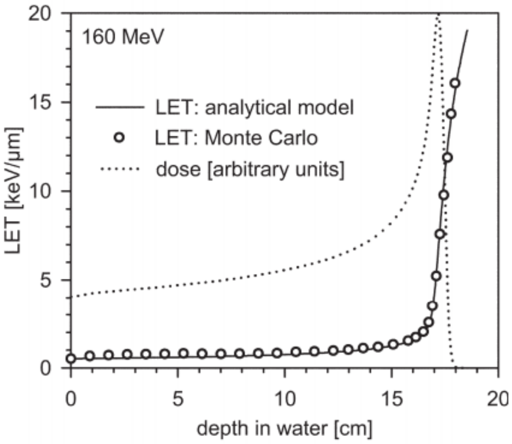

Figure 2.11: *Dose averaged LET vs depth for a 160 MeV, broad proton beam. The profile is shown along the central axis of the beam. The solid line and circles show an analytical model and Monte Carlo simulations respectively. Depth dose curve (dashed line) is shown in arbitrary units as a comparison ([16] using data from [17]).*

$$RBE = \frac{Dose_{x-rays}}{Dose_{particle}} \tag{2.2.15}$$

There are two assumptions associated with this formula (eqn 2.2.15), which make it clinically meaningful. First, it assumes the doses to be the macroscopic dose to the region of interest and secondly, it assumes this dose to be homogeneous. Clinically, a uniform RBE value of 1.1 is used in proton therapy [7] along the entire track of the beam. This therefore neglects variations due to LET [18], dose [19] and other additional factors [20].

2.2.7 Dosimetry

In both research and clinical use it is vital to be able to verify the dose delivered is that which was intended. The following sections shall describe the methods used in this work to determine the absorbed dose delivered. Although there are many different types of dosimeters available, the principle is the same for all. It is necessary to have a sensitive volume which undergoes changes when exposed to the type of radiation being investigated. This must be coupled with a device which is able to detect and measure these changes.

2.2.7.1 Ionisation Chambers

For ionisation chambers, the sensitive volume is a cavity filled with gas which, once ionised by incoming radiation, generates a current of charged particles. This current is measured by an electrometer, the output signal of which is taken to be proportional to the absorbed dose.

The chamber and electrometer must both be calibrated initially by a certified laboratory in order to determine their response to radiation. Such calibrations can be done by exposing the chamber to a known source of radiation. This is commonly done using Cobalt 60, which emits gamma rays of 1.173 MeV and 1.332 MeV. These sources are also typically used for quality control of treatment machines such as LINACs. Calibrations such as these will reduce potential systematic errors which could have serious consequences.

For dose measurements during radiotherapy treatments, a monitor chamber is typically used. These are parallel plate ionisation chambers which can be used to measure both beam flatness and symmetry [21]. Parallel plate dosimeters are composed of two electrodes as shown in figure 2.12.

2.2.7.2 Gafchromic EBT3 Films

For Gafchromic EBT3 radiochromic dosimetry films the senisitive volume is an active layer situated between two layers of 125 μm polyester. This active layer contains a marker dye and stabilisers. When exposed to ionising radiation the dye is activated, changing the optical density of the film, which can then be used as a marker for the dose delivered via equation 2.2.16.

$$d_x = -log\left(\frac{a + bD}{c + D}\right) \tag{2.2.16}$$

Unlike the ionisation chambers described previously, these films must be scanned in order to determine the dose value. This is done using an RGB flatbed scanner which measures the transparency of the film. This is then used to determine the amount of absorbed dose.

There are a number of limitations with this method; calibration of the film is re-

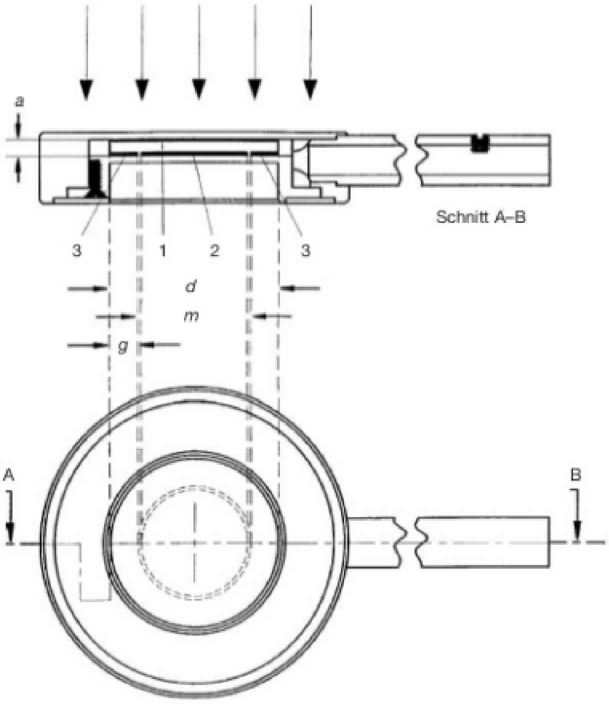

Figure 2.12: *Schematic diagram of a parallel plate ionisation chamber. Showing 1. Polarising electrode, 2. Measuring electrode, 3. Guard ring. The dimensions are shown by a. The electrode separation and height of the cavity, d. Diameter of the polarising electrode, m. Diameter of the collecting electrode and g. Width of the guard ring.*

quired for each radiation type used, variations in the orientation for both irradiation and analysis can impact the final readings.

2.3 Radio-biology

The following section builds on information from the book Radiobiology for the Radiologist, Eric J. Hall and Amato J. Giaccia [22].

2.3.1 Direct and Indirect Action of Radiation

It is well known that the most sensitive target within cells is the DNA [23],[24]. Damage to the DNA can result in both loss of function for the cell, or system and also cell death. Damage can be induced in two ways, either directly or indirectly.

Direct effects are seen when the incoming radiation interacts directly with the DNA molecule, thus damaging its structure via ionisation or excitation. This can either be through a break in the sugar phosphate backbone of the DNA or also a break in the hydrogen bonds between the DNA bases. This type of damage is the dominant process for particles, such as protons and alpha particles, which have high-LET.

For low-LET radiations, such as x-rays and electrons, indirect effects are dominant. Indirect damage occurs when radiation first interacts with organic molecules, such as water, surrounding DNA. A result of these interactions is the release of free radicals, which are extremely reactive atoms with an uncoupled outer shell electron. As water makes up around 80% of the cell contents, resulting reactions creating free radicals are as shown in equation 2.3.1, with $OH^{\cdot}$ being the most likely free radical to be produced.

If they are created close enough to the DNA within the cell, theses radicals become a risk. It is possible for oxidation to occur, where the free radical gains an electron from the DNA molecule. This process can result in a loss of function for the cell and ultimately cell death.

$$\begin{gathered} H_2O + Ionising\ radiation = H_2O^+ + e^- \\ H_2O^+ \rightarrow H^+ + OH^{\cdot} \\ e^- + H_2O \rightarrow OH^- + H^{\cdot} \end{gathered} \tag{2.3.1}$$

The potential resultant damage to bio-molecules (BM) are as shown below in equation 2.3.2. Where BMH is the undamaged bio-molecule, H is a hydrogen atom, and $H^{\cdot}$, $OH^{\cdot}$, $BM^{\cdot}$ and $BMHOH^{\cdot}$ are free radicals.

$$\begin{gathered} BMH + H^{\cdot} \rightarrow BMH_2 \\ BMH + H^{\cdot} \rightarrow BM^{\cdot} + H_2 \\ BMH + OH^{\cdot} \rightarrow BMHOH^{\cdot} \\ BMH + OH^{\cdot} \rightarrow BM^{\cdot} + H_2O \end{gathered} \tag{2.3.2}$$

2.3.2 Radiation Damage & Repair

Damage induced will be dependent on the type and energy of the interacting radiation. Studies have shown that survival of cells after proton irradiation is noticeably lower than after x-ray irradiation delivering the same dose [25]. This shows that the repair of damage caused by protons is less likely than the repair of that caused by x-rays. This is as expected when the interactions of these particles is considered in relation to the structure and distribution of DNA within the cells.

Different types of damage to DNA (fif. 2.13) includes damages to the bases, the sugar phosphate backbone and can also be in the form of strand breaks.

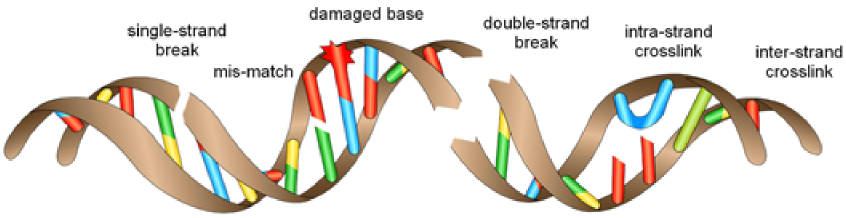

Figure 2.13: *Different potential types of DNA damage.*

Damage to DNA can be defined by single (SSBs) or double strand breaks (DSBs). DSBs can be the result of either two SSBs caused by different particles, but close enough in time and space to be considered a DSB. Or they can be produced by a single particle which produces a break in both strands of DNA. Considering these two possibilities it stands to reason that for higher LET particles, which deliver more energy per track length, the likelihood of a single particle inducing a DSB increases. Just as indirectly ionising radiation, which undergoes many smaller interactions the number of DSBs caused by two separate particles increases. The repair of these two types of damage varies greatly.

SSBs are typically repaired efficiently and without issue. Misrepair may cause problems, but these are usually of little consequence to the cell. Repair of SSBs takes advantage of the complementary nature of DNA, using the undamaged strand as a template to repair the damage. These repair mechanisms are base excision repair (BER), Nucleotide excision repair (NER) and Mismatch repair. BER involves faulty or damages bases being removed from the DNA helix and then being replaced. NER is used to repair more complex damages of the DNA double helix, this mechanism removed a section of the DNA strand and this is then repaired, using the second undamaged strand as a template.

DSBs can either be caused by a single event, or two separate events occuring extremely close in space and time. DSBs cause more issues as they require more complicated repair mechanisms, which in turn carry a greater risk of misrepair. DSBs can be repaired either by non-homologous end joining (NHEJ) or by Homologous recombination. NHEJ rejoin the two broken ends of DNA by ligation, this mechanism typically results in the loss of nucleotides at the repair site. Homologous recombination is typically initiated after DNA duplication, but before the division of the cell. This is a complicated process during which one DNA double helix acts as a template for a second indentical double strand.

The repair of DNA double strand breaks is initiated by the autophosphorylation of ATM (ataxia-telangiectasia mutated) kinase [26]. ATM then induces the phosphorlyation of the histone H2AX, which is then named γH2AX. These foci, of the phosphorylated histone H2AX, are formed quickly at the site of the DSB [27].These then signal for and recruit the necessary repair enzymes [28]. In order to increase the chances of repair of any damages the cells may also become arrested in the G2 phase.

Other complications associated with DSB repair include deletions, duplications and translocations. Finally, asymmetric chromosomal aberrations may also occur, as per figure 2.14, and are typically irreparable and result in the death of the cell when it enters mitosis.

The damages discussed can be divided into three different categories: lethal, potentially lethal and sublethal damage. Lethal damage is complex, irreparable damage, such as asymmetric choromosomal aberrations. These will therefore lead to the death of the cell. Potentially lethal damage becomes lethal to the cell if they are not repaired in time. This is such damages as DSBs. While sublethal damage is typically efficiently repaired, it becomes an issue if a number of sublethal damages occur close enough in space and time. The vast majority of SSBs can be considered to be sublethal damages and these will become potentially lethal if two occur close

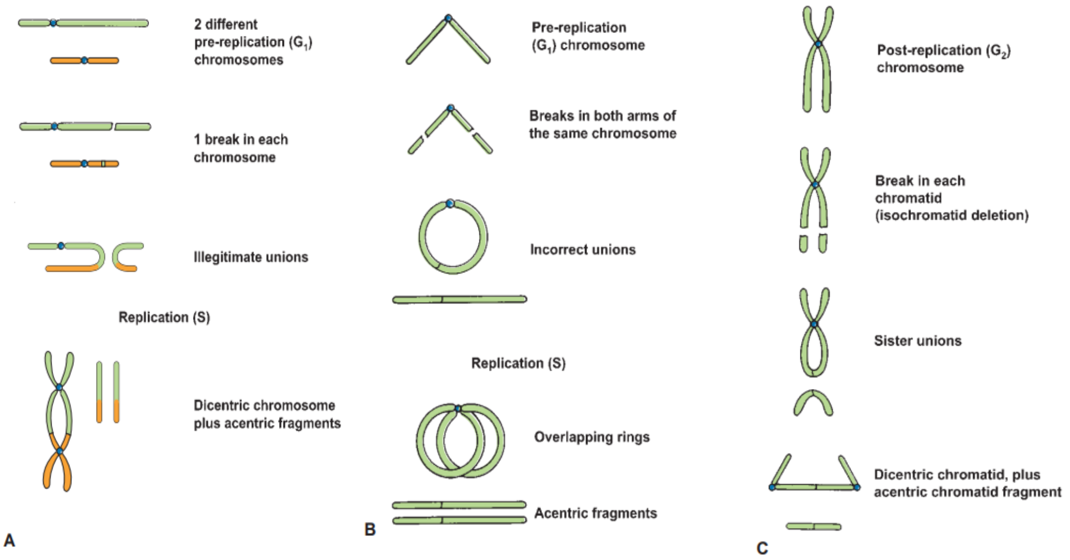

Figure 2.14: *Different types of chromosomal aberrations. A: Formed by irradiation of G1 chromosomes resulting in broken ends of chromosomes rejoining incorrectly and this being replicated in S phase. B: Formed by irradiation of G1 chromosome, causing a break in the arms of each chromosome which then join to form a ring. C: Formed by irradiation of G2 chromosomes, an anaphase bridge is the result of breaks in each chromatid joining together [22].*

enough for an interaction between them [29].

When repair of damage is not possible, or not favourable to the cell or system, programmed cell death may be initiated. This is named apoptosis and allows the constituents of the cell to be reused by the surrounding cells. This process is characterised by a number of physical changes to the structure of the cell. This includes cell shrinkage, irreversible condensation of chromatin within the nucleus and finally fragmentation of the nucleus itself [30] [31]. This differs from necrosis, which is the uncontrolled mechanism of cell death, which results in negative effects such as inflammation of the surrounding tissue.

2.3.3 Repair Kinetics

Typically, there are two phases of cell repair - an initial fast phase, in which simpler damages are repaired and a second slower phase, during which more complex damages are repaired as seen in figure 2.15. The initial steep slope of the curve demonstrates DSBs which have been quickly (2 - 6 hours) and efficiently repaired.

Whereas the second part shows the slow phase of repair (up to 24 hours) [32]. This slow phase is thought to be activated by ataxia-telangiectasia mutated (ATM) a protein which phosphorylates H2AX and also leads to arrest in the G2 phase [33] [34].

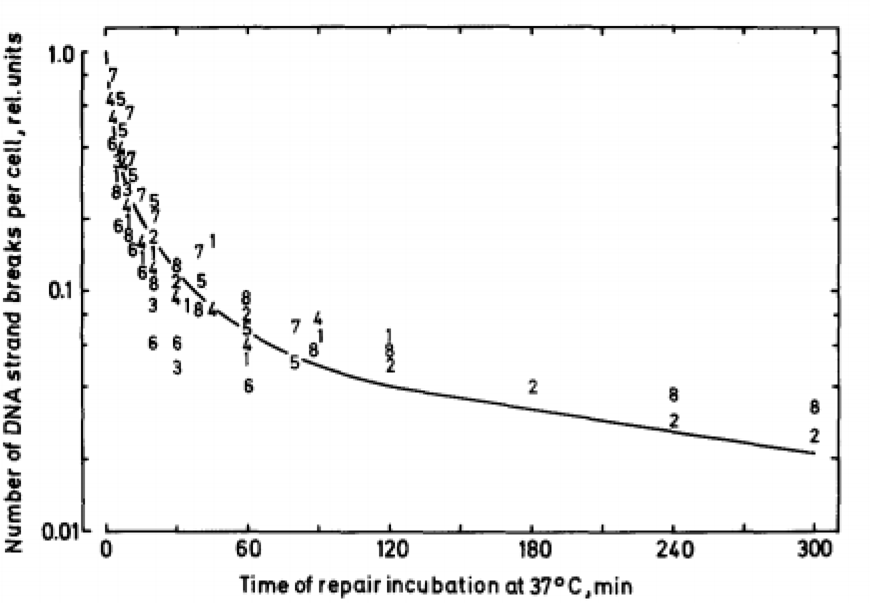

Figure 2.15: *Repair kinetics of X-ray induced DNA strand breaks, taken from [35]. Numbers represent experiments using different cell types and doses, while the solid line represents the repair kinetics after x-irradiation of Chinese hamster ovary cells. [36]*

The rate at which damages are repaired over time varies between cell types, types of damage induced and the repair mechanisms which are at work. For cells with deficient repair pathways, for example p53, the time taken for the slow phase of repair will be increased [32] [37].

2.3.4 Tumour biology

Considering the mechanisms discussed, it is important to understand the key differences between normal cells and cancer cells. These differences can be exploited during radiotherapy, but are also the root of a number of problems.

First, two key gene types associated with cancer will be discussed. These are oncogenes and tumour suppressor genes. In normal functioning cells, these genes are simply genes which encourage and halt progression through the cell cycle respectively. However, when these genes become mutated or malfunctioning they can drive abnormal proliferation of cells [30]. Oncogenes, such as the Ras genes, play a key role in signalling for cell proliferation, differentiation and survival. If these are over-expressed they can therefore initiate unnecessary cell proliferation.

The opposite is true of tumour suppressor genes such as p53, which is usually a key gene in the activation of apoptosis and cell cycle arrest [38][39]. If these are mutated or lost the damaged cells will again continue unwanted proliferation. It is this gene which is commonly lost or malfunctioning in cancer cell lines such as the T98G glioblastoma multiforme cells. This causes rapid proliferation of the mutated cells, leading to an aggressive tumour which is difficult to eradicate.

Due to these differences in the control of cell proliferation between normal and cancer cells, there will therefore be a difference in the effects of ionising radiation seen for the cell types. Normal cells will preferentially begin apoptosis or halt proliferation if extensive damage to DNA is detected. Whereas cancer cells, if the associated genes have been mutated or lost, will not have this control mechanism and are therefore more likely to continue through the cell cycle regardless of DNA damage.

2.3.5 Dose-Survival Measurements

2.3.5.1 Linear Quadratic Model

Clonogenic cell survival is often used as a way of predicting the sensitivity of cells to a certain radiation type. This quantity represents the fraction of surviving cells which are capable of forming colonies after irradiation compared to unirradiated cells. A semi-logarithmic plot of the surviving fraction of irradiated cells against absorbed dose values creates a commonly used clonogenic cell survival curve. The linear quadratic (LQ) model (eqn 2.3.3) is used to define these curves as shown in figure 2.16.

$$lnS = \alpha d - \beta d^2 \tag{2.3.3}$$

where α and β are the two components of cell killing. α is the coefficient rep-

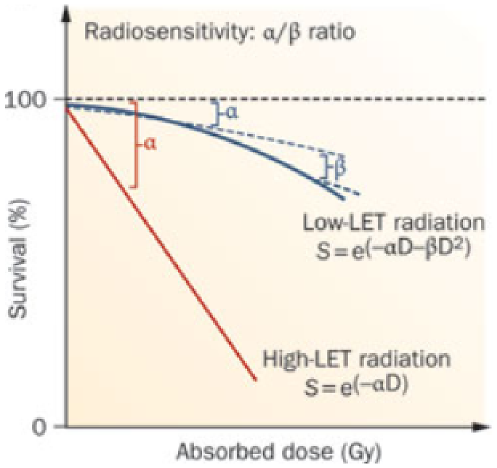

Figure 2.16: *Examples of the LQ model demonstrating expected cell survival after high and low LET irradiation. Where α and β represent single hit and double hit inactivation coefficients respectively, D is absorbed dose*

resenting DSBs caused by a single hit, while β is the coefficient of two single hits resulting in a DSB. The ratio of α/β can be used to describe the radio-sensitivity of a type of tissue. Studies have shown that this value varies greatly between late responding tissues such as the brain or spinal cord ($\alpha/\beta \approx 2$), early responding tissues ($\alpha/\beta \approx 5$ - 8) and malignant fast-growing tumours ($\alpha/\beta \approx 10$) [40]. The effects of these different values on the survival of the cells after irradiation are as shown in figure 2.17.

This model is used clinically to determine the end points for different types of treatment, taking into account normal tissue complication probabilities as well as the tumour control probabilities. From figure 2.16 it is possible to see that for high-LET radiation the β variable has been removed, due to the nature of the damages induced as discussed previously. It is much more probable that DSBs will be induced by a single particle interaction, rather that two interactions. Therefore for tumour irradiation high LET radiation would be optimal, but this introduces complications for normal cells.

Figure 2.17 shows a different shape of the survival curves for tumour and normal tissue. The extended "shoulder" seen for normal tissues is why fractionated treatments were introduced. By exploiting the mechanisms for repair within normal cells and simultaneously the hyper-sensitivity of tumour cells, it is possible to achieve

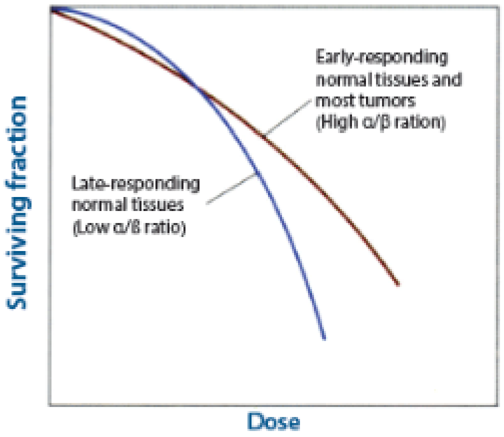

Figure 2.17: *Difference in surviving fraction for early responding normal tissues and most tumours (high α/β) compared to late responding normal tissues (low α/β) plotted using the LQ model [41]*

optimum therapeutic results. This type of treatment takes advantage of the visible shoulder for late responding tissues at low doses, therefore killing more tumour cells than normal cells per fraction. It will be in reference to this model that the results of this project will ultimately be presented.

2.4 Methods of Analysis

Multiple methods will be used in order to quantify the effects which have been discussed. With a clear understanding of the end points of radiotherapy as a whole, the damage to the cells can be investigated by looking into the G2 checkpoint arrest, DNA double strand breaks and apoptosis levels.

2.4.1 Flow Cytometry

Analysis of the irradiated cells will be done using flow cytometry, this technique detects light scattered by individual cells, giving an insight into their structural properties. For these experiments the cells will be stained with fluorescent dyes, used to detect changes induced by radiation damage. Propidium Iodide will also be used during the labelling of the cells. To give both information about the integrity of the cell wall and, after previous permeabilisation of the cell membrane, the DNA content of the cells.

A set up of the Flow cytometer can be seen in figure 2.18 below. Hydrodynamic focusing is used to create a single file of cells flowing through the system. (*MultiCycle AV manual*).

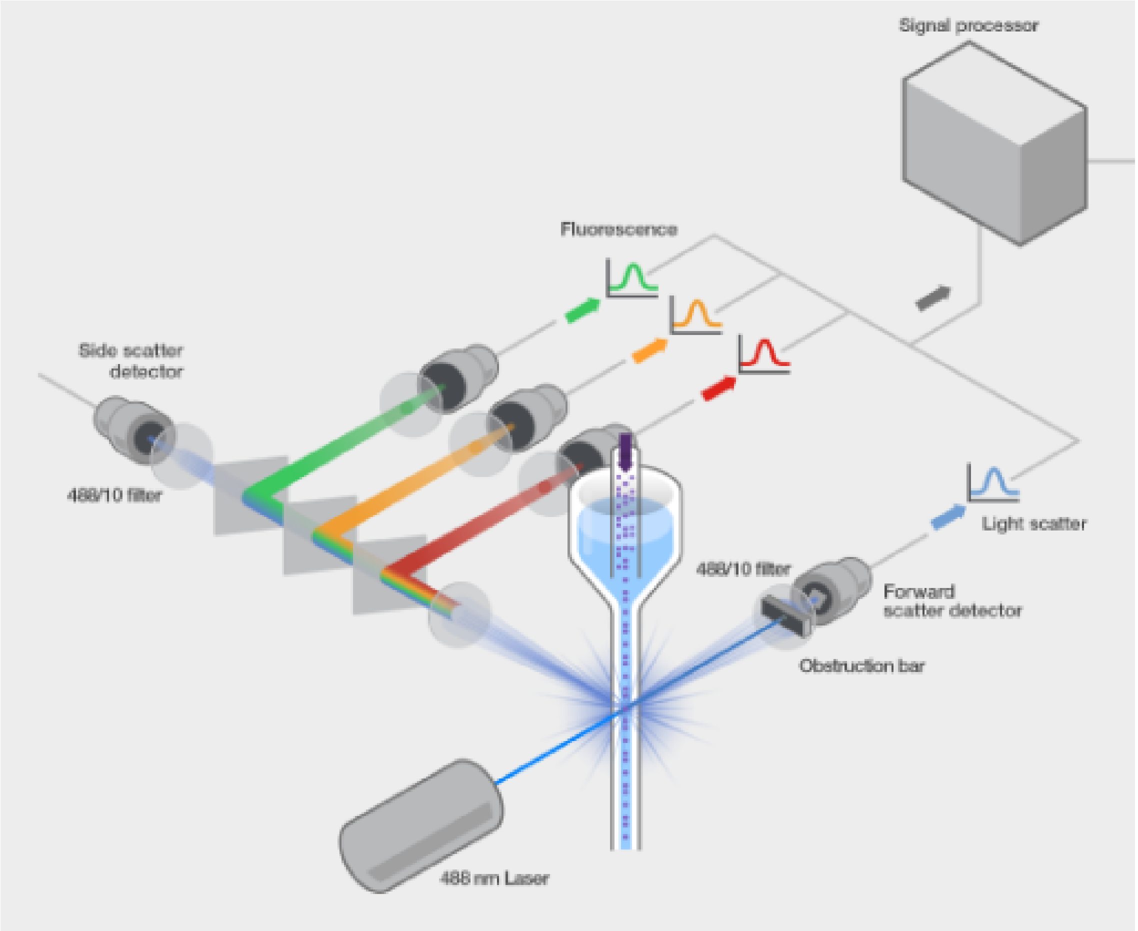

Figure 2.18: *Schematic diagram of a flow cytometer with examples of the resultant signals from cell analysis [42]*

Lasers are then used to excite the fluorochromes in the cells as they pass through the system. In addition the scattering of this light gives an insight into the structure and various properties of the cell. From the two main channels in the system, forward scatter (FSC) and side scatter (SSC), we gain information about the cell's size and internal structure of the cell respectively. Fluorescent dyes are used to stain a specific structure within cells, such as DNA or other proteins. The resultant excitation fluorescence can then be detected for each cell and this is considered to be directly proportional to the associated contents. The resultant signals from the cells generate a event in the Photo-multiplier tube (PMT) detectors. These events then produce an output signal which can then be plotted for analysis of the sample.

2.4.2 Cell assays

2.4.2.1 H2AX phosphorylation

In order to detect induced DNA damage within irradiated samples, the mechanism of H2AX phosphorylation was used for the work done in this thesis. H2AX is a histone of the H2A family and is responsible for signalling and recruiting response proteins to the site of DNA damage [43]. With increasing levels of DNA damage the level of detectable γH2AX (the phosphorlyated histone) increases. With the γH2AX assay, PI was introduced into the protocol after permeabilisation of the cell membranes. This was done in order to determine the DNA contents of the cells in order to gate for cells in G1. An example of this is shown below in figure 2.19b, the largest peak shows the cells in G1, this peak will always be the largest as this is where cells spend most of their time, the central part shows cells in S-phase, while the final section is cells in G2. This was a vital additional to the cell assay procedure, as when the cells pass through S phase to G2, the amount of DNA increases and therefore the uptake of γH2AX would also increase.

The variation of DNA content throughout the cell cycle can be investigated using Propidium Iodide (PI). PI is a fluorescent stain which binds to double stranded DNA and therefore can be used to measure the DNA content in a sample. When measured using Flow Cytometry it produces a clear DNA histogram as the cells have been permeabilised allowing PI to easily penetrate the cell wall. An example of one of these images is as shown in figure 2.19.

The mechanism of G2 arrest can therefore be visualised using this staining technique. It would be expected that higher LET protons would produce a greater amount of G2 arrest. Increased levels of complex damage will result in longer repair

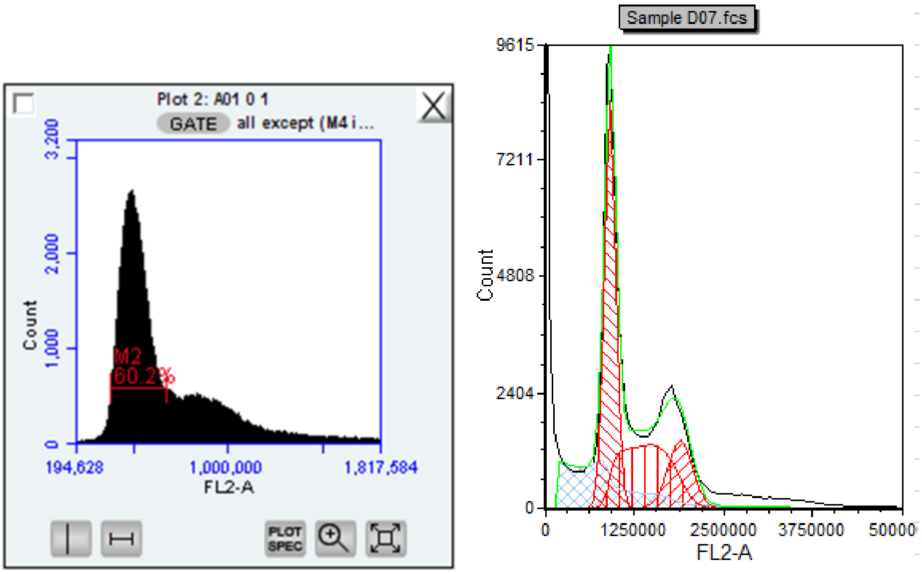

(a) *DNA histogram produced by the Flow Collect program.*

(b) *DNA histogram fitted using FCS express.*

Figure 2.19: *Example DNA histogram produced after x-ray irradiation, showing fluorescence of PI stained cells (detected by the FL2-A channel of the flow cytometer).*

times and therefore more cells halted in the G2 phase. This means not only that protons should show increased levels of arrest compared to x-rays, but also that cells irradiated in the back part of the Bragg peak will show higher levels in relation to before the Bragg peak.

2.4.2.2 Apoptosis Assay

As described previously, apoptosis is a mechanism through which cells protect the larger system to which they belong. Annexin V is a phoshpolipid binding protein which binds to Phosphatidylserine (PS) which becomes exposed during apoptosis. PS is typically contained within the membrane of the cell, however, during apoptosis as the membrane disintegrates PS translocates to the outside of the cell where it can be detected. This process can be seen in figure 2.20. In this assay, the cells are not permeabilised and therefore only PS which has translocated to the outside of the cell membrane will be targeted by Annexin V.

In addition, PI was used as a marker for the integrity of the cell wall. For cells with a defect membrane PI will be able to penetrate and stain the cell, thus distinguishing between viable and necrotic cells.

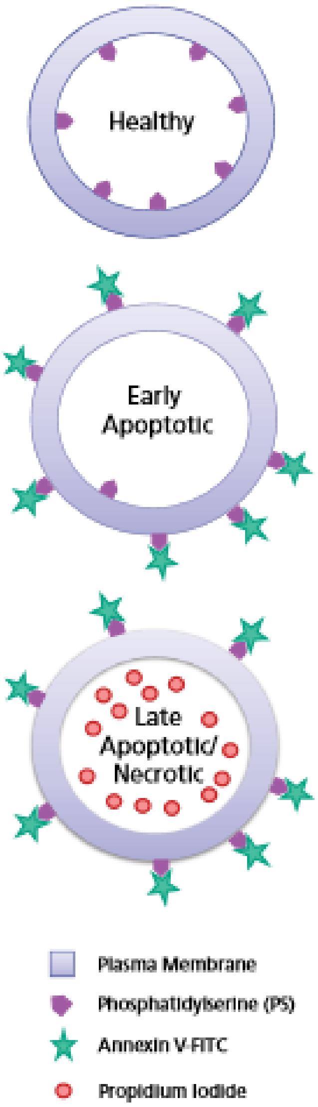

Figure 2.20: *PS translocation and Annexin V binding for different stages of apoptosis.*

Chapter 3

Materials and Methods

3.1 Materials

3.2 The Cell Line

For all of these experiments, cells from the T98G line were used. These are human glioblastoma multiform brain cancer cells, the most common type of malignant tumour seen in the central nervous system. This particular cell line originates from the tumour of a 61 year old Caucasian male [44]. All experiments were performed whilst the cells were undergoing exponential growth.

3.2.1 Cell cultivation

The cells were cultivated in flasks using sterile, filtered RPMI 1640 medium (*Lonza, Belgium*) with 2mM L-Glutamine (*Sigma, Saint Louis, USA*). In order to provide the cells with the necessary growth factors, the medium was supplemented with 10% fetal bovine serum (Euroclone, Devon, UK), 1% penicillin/streptomycin (Euroclone, Devon, UK) and 200 units/liter insulin (Sigma, Saint Louis, MO, USA). Additionally, the RPMI 1640 contained phenol red (Merck, Germany), which acts as a pH indicator, changing colour over the pH range of 6.6 to 8.0. This will simply be referred to as medium throughout the rest of this report. The flasks were all incubated at 37°C, 80% humidity and 5% CO_2 in either a Steri-Cult 200 CO_2 incubator (*Forma Scientific, USA*) or a Thermo Forma Series 2, Water Jacketed CO_2 Incubator (*Forma Scientific, USA*).

Cells were seeded into dishes with fresh medium and then incubated again for at least 24 hours before irradiation. Various cell dishes and flasks were chosen for the different experiments performed. These will be stated individually in the relevant experimental sections, but include 25 cm^2 (5 ml) sterile flasks, 8.8 cm^2 (3 ml) and 21.5 cm^2 (5 ml) sterile vent dishes (*All from Thermo Fisher Scientific Nunc A/S, Denmark*). The cells used were grown in the cell laboratory of the Biophysics group at the Department of Physics, University of Oslo (UiO). All reseeding and cell work was performed in the same laboratory.

All work, during which the cells were removed from the incubator and exposed to alternate environments, was performed in a Laminar Air Flow (LAF) bench. Two benches were used, a Class 100 Laminar Air Flow cabinet (*Gelaire, Australia*) - used for reseeding and harvesting - and a VB 2040 Laminar Air Flow cabinet (*Odd A. Simonsen, Norway*) - used during x-ray and proton irradiations. These benches were disinfected using 70% ethanol before and after use.

All equipment used during the experiments was sterile. Sterile pipettes and syringes (*Saarstedt, Germany*) were unpackaged within the LAF bench and disposed of after use. Any unpackaged equipment, such as the bottles of chemicals, were cleaned using 70% ethanol before being placed within the bench. Bottle caps and the top of the bottles were sterilised using a hand held propane blow torch after opening and prior to closing.

Additional equipment such as glass bottles and incubator trays were sterilised by being wrapped in double layers of aluminium foil and dry heated in a Termaks oven (*Termaks, Norway*) at 180°C for three hours. Cloths and lab coats were packed and sealed in autoclave paper bags and autoclaved (*Labo Autoclave, Sanyo*) at 121°C for 25 minutes. Sterile gloves were used for handling and transporting the dishes. Sterile coats were worn during irradiations and were also used to wrap trays of dishes in for transportation.

3.2.2 Maintenance of the Cell Line

Due to the growth and division of cells under the conditions of incubation it is necessary to re-culture the cells every 3 to 4 days. This is done in order to avoid confluence, which would lead to cell cycle arrest [45, 46]. Fresh medium is also given once a week, inbetween re-culturing, to ensure that the cells have sufficient nutrients and growth factors to maintain exponential growth. During this process the cell density within each dish is also checked, and if it is seen to be too low or high then an alternate schedule for sub-culturing is considered.

A combined mixture of Trypsin and EDTA is used to remove the cells from the surface of their dishes and place them into suspension. Trypsin is an enzyme used to detach cells while EDTA enhances the activity of Trypsin by removing calcium and magnesium from the cell surface, thus enabling Trypsin to hydrolyze specific peptide bonds [47]. This mixture is heated in a water bath up to 37°C before use.

When necessary an optical microscope x10 magnification (*Nikon TMS, Japan*) is used to check that sufficient separation of the cells had occurred.

3.3 Experimental Procedure

3.3.1 Preparations

A plan was made for each experiment performed, detailing the order of irradiation and the labels used for the samples. Paper copies of the relevant plans were given to those persons present for sample preparation and irradiation.

Due to strict time limitations, particularly during proton irradiations, the following procedure was followed before and after.

Before any experiment the following preparations were made:

- Steel dishes (x-ray experiments only) and incubator trays were sterilised.
- Cloths and coats were autoclaved.
- Parafilm (*Pechiney Plastic Packaging, Menasha*) was cut, soaked in surface disinfectant for minimum one hour, then left to dry over night in a LAF bench. The following day these were transferred into a sterile glass dish which was covered with a lid.
- Cell dishes labelled and ordered on the tray - placed in order of irradiation.
- LAF benches stocked with pipettes, sterile cloths, empty flask for waste liquids, sterilising wipes and gloves.
- Electronic pipettes (*Pipetus-akku Hirschmann Laborgeraete, Germany*) charged.

On the day of experiments:

- Sterile tape for sealing parafilm lids cut to size on LAF bench.
- Sample tubes for the centrifuge labelled to match the cell dishes.
- Medium added to tubes and stored on ice.
- Ensure settings (1400 rpm for 4 minutes) and attachments in centrifuge are correct. Both a Rotofix 32A (*Hettich, Germany*) and a MegaStar 600R (*VWR, USA*) centrifuge were used.
- Any mixtures needed for processing, mixed and stored in labelled tubes on ice.
- Cell samples transferred to incubator closest to x-ray machine/cyclotron.
- Trypsin and medium heated for use - Medium taken to LAF bench before irradiations begin.

For x-ray experiments:

- X-ray machine and water bath turned on
- Steel dishes cleaned with 70% ethanol and left to dry

For proton experiments:

- New EBT3 films (*Ashland, USA*) taken to cyclotron.
- Cell holder allowed to heat up.
- Switch on and set up ionisation and monitor chamber readers.

Dishes were sealed using parafilm and tape, depending on the experiment. For proton experiments the dishes were irradiated without medium, due to the horizontal beam which required the dishes to be positioned vertically. Care was taken to remove all of the medium from the dish as any remnants showed to provide protection to the cells which it covered[6]. Due to the time taken to reach the required doses using x-rays, the cells were irradiated with the medium on in order to maintain a more suitable environment. However, the effects of x-ray irradiations with and without medium were previously shown to have no significant effect on results for the doses used [6].

3.3.2 Irradiation

The cells were irradiated with either x-rays or protons. These irradiations were performed at the University of Oslo using an x-ray PANTAK PMC 1000 unit (*Pantak, USA*) or the Scanditronix MC-35 cyclotron (*Scanditronix, Uppsala, Sweden*) at the Oslo Cyclotron Laboratory.

3.3.2.1 X-ray Irradiation

The X-ray unit and water bath were switched on and allowed 30 minutes to warm up prior to the irradiations in order to maintain the temperature of the cells. The beam was filtered by both a 0.5 cm copper filter placed in front of the beam window and the lid of the steel chamber in which each sample was placed. With beam settings of 220 kV and 10 mA, and a dose rate of 1 Gy/2.3 minutes [6] the times were calculated for each desired dose.

After each sample was irradiated, it was immediately returned to the incubator, the time points were noted for both the start of each irradiation and when it was removed and returned to the incubator. Samples to be processed at 0.5 hours, as soon as possible after irradiation was complete, were treated with Trypsin and the flow cytometry procedure was begun.

3.3.2.2 Proton Irradiation

For proton irradiations the set up was as seen in Figure 3.1. The energy of the beam was found to vary from day to day. Due to the fluctuations of this value, the position of the Bragg peak was found each day by dosimetric measurements before each day of experiments. The shape and position of the beam were also noted and adjusted prior to beginning the experiments. This was using EBT3 film, taped in front of the exit window, as seen in Figure 3.1.

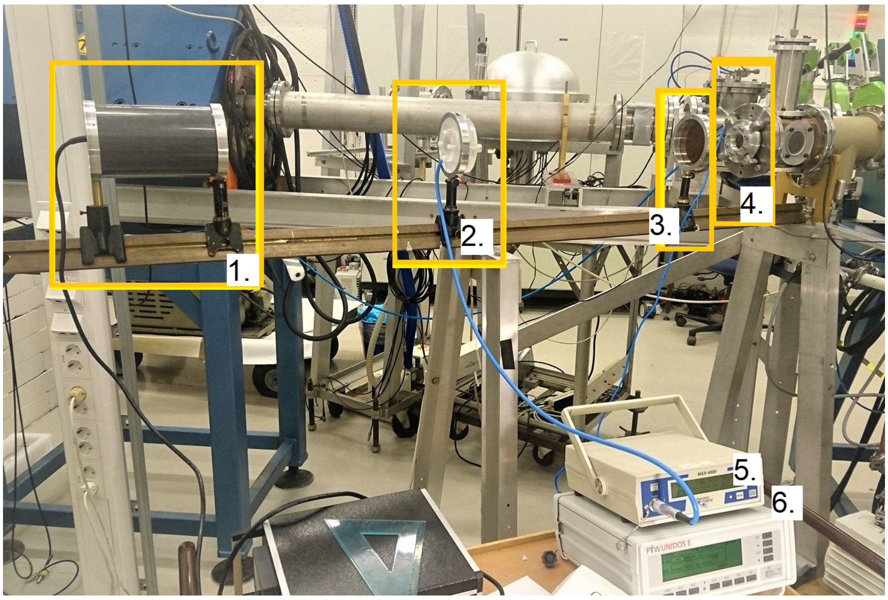

Figure 3.1: *Set up for proton irradiations showing the cell holder (1), ionisation chamber used for calibration and dosimetry (2), transmission chamber (3), beam exit window (4) and electrometers for the ionisation and transmission chambers (5 & 6).*

The position of the Bragg peak was determined at the beginning of each day of experiments. This was done by recording dose measurements to the ionisation chamber. The dose rate was calculated at different distances from the beam exit window and with varying thicknesses of absorber material. From these findings, the position of the holder for the cell dishes was adjusted for each experiment depending on the energy of the beam on that day. Once the positions for irradiation had been determined, a sheet of EBT3 gafchromic film was irradiated in position. After irradiation they were kept for 24 hours sealed in a thick envelope with no exposure to light and then scanned using a flatbed RGB scanner. The resultant images were then analysed using an IDL program to convert the optical density of the image to a value for the average dose across the surface of the film.

The scanner determined the transparency of the irradiated (and unirradiated control) films, in terms of the intensity of the light able to pass through. This light intensity value, I, was then converted to dose using the formula for optical density, OD, below (eqn 2.2.16).

$$OD = log_{10} \times I \tag{3.3.1}$$

Appendix D contains details of the positions used for each proton setup, with the tabulated results of the measurements done to determine the dose rate and position of the Bragg peak for each experiment. Also included are the relevant EBT3 Gafchromic film dose measurements.

Plots of calculated dose against depth in water have also been included. Depth of the proton interaction was converted into water equivalent thickness (WET) values, as this is used clinically due to the similarities between interactions in water compared to tissue.

The dishes were prepared in a sterile LAF bench. The medium was removed and a single sheet of parafilm taped over the dish before the dish was placed into a sample holder for irradiation. Due to the physical nature of the parafilm, care was taken to ensure the sheet was not stretched and placed flat across the surface. This procedure was followed for all dishes irradiated before the Bragg peak. For those to be irradiated within the Bragg peak (shown in Figure 3.2) the lid of the cell dish was used in place of the parafilm.

The samples were then transported, two at a time, to the cyclotron inside a sterilised polystyrene box containing heated flasks of water in order to maintain the temperature. The time each sample spent without medium was recorded. An effort was made to keep this time to a minimum in order to reduce the negative effects to the cells caused by the varying conditions, in particular the pH [48].

After irradiation, and with fresh medium added to the dishes, the samples were immediately returned to the incubator. The time out of incubation was also recorded for each sample in order to account for any anomalies seen after analysis. For transportation from one incubator to another the dishes were placed on a sterile metal tray and wrapped in a sterile cloth to minimise exposure to air.

Different positions along the proton track were investigated, these were defined as Front, Top and Back, in relation to the Bragg Peak. As shown in Figure 3.2.

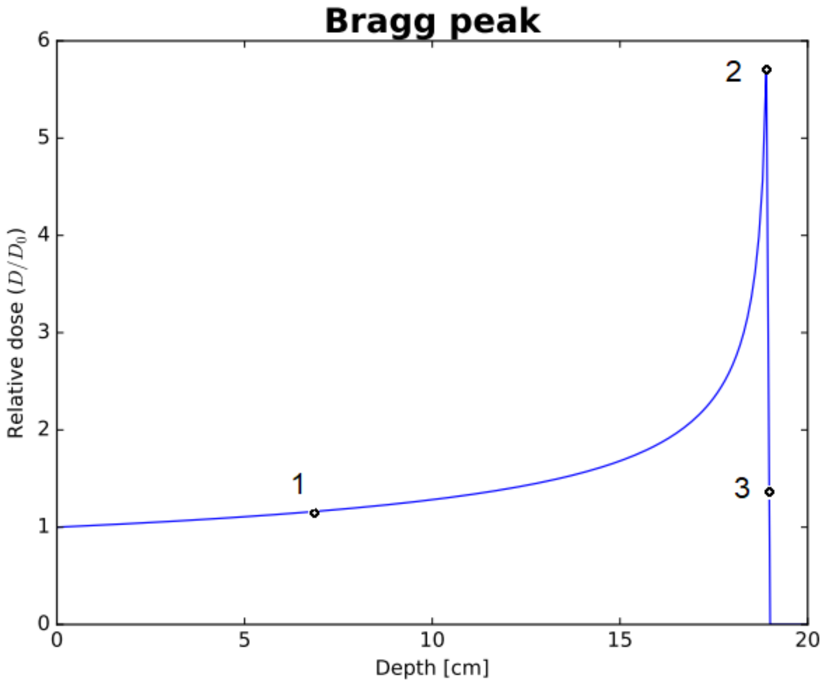

Figure 3.2: *Positions of irradiation along the proton track: Front (1), Top (2) and Back (3). The position in the back of the Bragg peak was adjusted in order to obtain the same dose rate as in the front.*

Position 1 is 'Front' a low LET position before the Bragg peak. 'Top' is shown as position 2, which has the highest dose rate in the very top of the Bragg Peak and position 3 shows 'Back' with the highest LET value, in the back of the Bragg peak with the same dose rate as position 1. The estimated values for LET at each position are as tabulated in below (table 3.3.2.2) using values from monte carlo simulations

[49] and previous experiments at UiO.

Position	LET (keV/μm)
Before	5 - 10
Top	23 - 28
Back	38 - 44

The LET of the x-ray beam at UiO has been found to be 3.6 keV/μm [50].

Control samples were used for all experiments, these dishes were removed from the incubator and placed in the LAF bench with or without medium, depending on the experiment type. They were left out for the average amount of time the corresponding irradiated samples spent out of the incubator.

3.3.3 Incubation and Fixation

The irradiated samples either processed at 0.5 hours after irradiation, or were incubated for the designated amount of time. This was either 24, 48 or 72 hours. Different time points were observed in order to test the ability of the irradiated cells to repair the damage which had been induced. During this incubation period the medium of the samples was not changed.

Prior to processing using flow cytometry, the cells were removed from the incubator. The dish or flask was trypsinised in order to release the cells from the base of the dish. A pipette was used to gently separate the cells while a microscope was used to ensure an appropriate amount of separation had been achieved. The suspension was then transferred into a tube containing fresh medium. Each sample was then fixed and stained using the appropriate kit and method as described in the following section.

3.3.4 Flow Cytometry

All samples were processed using a BD Accuri C6 flow cytometer (*Becton Dickinson, USA*). The detection system consists of a blue and red laser, two light scatter detectors (used for forward and side scatter) and four fluorescence detectors. These four fluorescence detectors are as listed below, with their associated excitation/emission wavelengths and also the fluorochrome which they were used to detect:

- FL1, 533/30 nm, Alexa Fluor 488 and FITC
- FL2, 585/40 nm, PI.
- FL3, 670 nm, not used in these experiments.
- FL4, FL4 675/25 nm, Dylight 650 dye.

FL1, FL2 and FL3 all detect fluorescence emitted by blue laser excited fluorescence, while the FL4 detector collects red laser-excited emissions.

The forward and side scatter detector signals (FSC and SSC repsectively) were used in order to remove fragments and dead cells. FSC gives an indication of the cell size while SSC shows the granularity of the cells. Fragments tend to have both low FSC and low SSC and were therefore removed from the population to be investigated. Before processing using flow cytometry, the directions were followed for the two assay kits used, with slight alterations made due to previous experiments done at UiO using the same procedure with T47D cells [N. Edin, personal communication]. For detection of DSBs, the FlowCollect Histone H2A.X Phosphorylation Assay Kit was used (*EMB Millipore, Germany*) while the TACS Annexin V-FITC Apoptosis Detection Kit (*Trevigen, USA*) was used for apoptosis detection.

3.3.5 γH2AX Assay

For detection of DSBs the phosphorylation of the histone H2AX was studied. This was done by staining irradiated samples with an antibody which detects phosphorylated H2AX histones. The antibody used was Alexa Fluor 488 conjugated, and it was the fluorescence of this fluorochrome which was detected during flow cytometry.

Along with this conjugated antibody, the cells were also stained with Propidium Iodide (PI) and treated with RNase. As PI stains not only DNA, but also double stranded RNA, RNase was included in order to remove RNA during processing.

One key alteration to the procedure for the H2AX assay was the introduction of freezing of the samples in their permeabilisation buffer. This was done in order to allow for all of the samples for a single experiment to be processed together. This helped to ensure that the same concentration of dye was used for each sample.

After finding it difficult to determine the base level of damage and repair for the cells a fluorescent cell barcoding control was introduced into the procedure. This used Dylight 650 NHS Ester dye (*Thermo Scientific, USA*) to stain control samples, a small concentration of which was then added to the irradiated samples before processing. This allowed for detection by a separate detector in the flow cytometer, providing an internal standard for each experiment.

This procedure helped to more effectively normalise the results from each experiment and to minimise the inherent effects of drifting caused by the flow cytometer. The full procedure for this is as shown in Appendix A.3.

3.3.5.1 DSB detection

Procedure from Flow Collect Histone H2A.X Phosphorylation Assay Kit was followed in order to fix, permeabilise and stain the cells before analysis by flow cytometry. Prior to processing, the mixtures required were prepared and stored on ice, in tubes wrapped in tin foil in order to minimise their exposure to light.

The detailed procedure followed for each experiment can be found in Appendix A.1.During the collection of results the cells were gated as shown schematically in Figure 4.4.

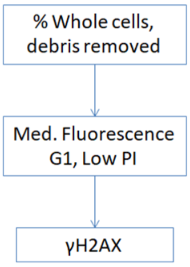

Figure 3.3: *Gating for samples processed with γH2AX kit*

Using the PI fluorescence signal in FL2 detector, viable cells in the G1 phase of the cell cycle were selected. These cells were selected as cells in this phase have a single set of DNA and therefore the fluorochrome fluorescence required no normalisation. If fluorescence from cells in the S or G2 phase were to be a used, a correction factor would be required due to the increased DNA levels [51]. This gate was then applied to the cells stained with H2AX seen in the FL1 detector signal.

For cell barcoding this procedure varied slightly to the initial experiments. Using the FL4 detector it was possible to gate for the cells stained with the Dylight and the irradiated samples separately. These two populations were then gated and used to separate the PI fluorescence detected by the FL2 detector. It was then possible to subtract the median or mean fluorescence values of the dyed controls, as a way of normalisation. Thus reducing the effects of the variations in signal caused by the flow cytometer and allowing for clearer interpretation of the final values.

The final corrected values of the mean and median γH2AX fluorescence were taken to be directly proportional to the number of DSBs present in each sample.

Histograms produced, showing the uptake of PI in the cells, made it possible to clearly see cells in the various stages of the cell cycle. This allowed for the possible cell cycle arrest in the G2 phase to be investigated. This was done using the FCS express program to determine the relative percentage of cells in the different phases of the cell cycle for different time points and doses.

3.3.5.2 Annexin V-FITC Assay

For detection of levels of apoptosis induction after irradiation the Annexin V-FITC cell assay was used. The samples were stained with Annexin V, a protein which binds to Phosphatidylserine (PS) which is exposed during early apoptosis, conjugated with FITC (Fluorescein isothiocyanate). As seen in 2.20, PS translocates to the outside of the cell membrane during the early stages of apoptosis. Again, it was the fluorescence of the FITC fluorochrome which was detected during flow cytometry.

PI was also used during this procedure, but in this case the cell membrane was not permeabilised. PI staining was therefore used as a way of determining the viability of the cell membrane. The selection of the final data used was again done by gating the signals collected by the different detectors, as shown schematically in Figure 4.13.

The fluorescence of FITC was measured by the signal collected by the FL1 detector and PI by the FL2 detector. It was initially thought that the four final

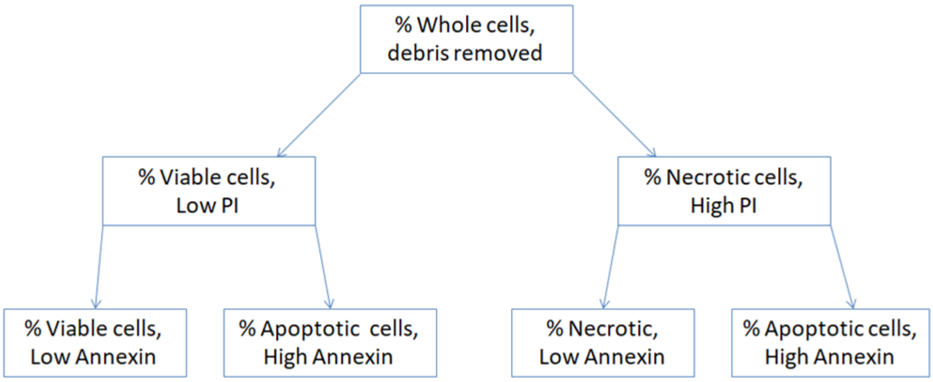

Figure 3.4: *Gating for samples processed with Annexin V-FITC kit*

populations would be easily distinguishable. However, a number of different methods were attempted for analysis of the results from the apoptosis data. With the kit it was expected that there would be distinct populations visible after processing. An example of the expected results, taken from the manual for the kit, is as shown in Figure 3.5. Figure **??** has been included as a reference of the gating attempted in this study. Due to the spillover between the detectors, colour compensation was attempted in order to separate the populations more clearly. Due to the manual nature of this method the results were not considered reproducible and were therefore abandoned.

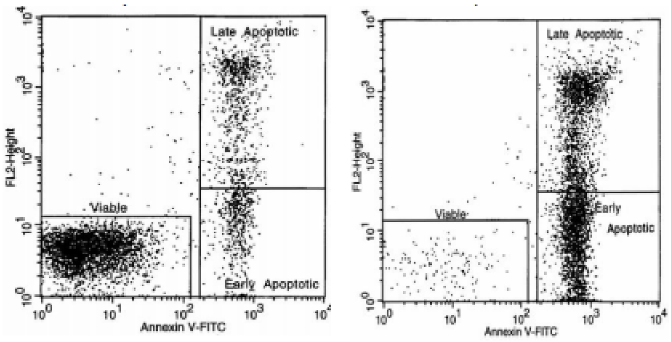

Figure 3.5: *Example of gated populations before treatment (left) and after treatment (right) showing increased apoptotic cell population.*

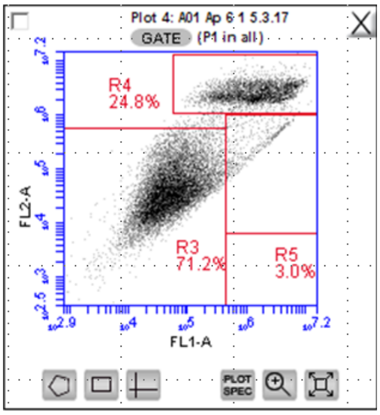

Figure 3.6: *Example of attempted gating on Annexin V sample 6 hours after proton irradiation*

3.3.6 Presentation of Data

Each experiment was performed in triplicate. The results presented for each time point, dose and radiation type will therefore be an average value with the standard deviation.

3.3.6.1 DSBs

Using the detected γH2AX fluorescence in the viable G1 population for each sample, plots will be presented showing the variation of fluorescence over time for each dose and radiation type. This will give an indication of the rate of repair occurring in the cell samples.

The flow cytometer offers both median and mean values of the detected fluorescence for each sample. A number of studies have shown to preferentially use the median values from this program and therefore the average median values will be presented in this report. However, for completeness corrected mean values of the γH2AX fluorescence values over time for 5 and 10 Gy are included in Appendix B.

3.3.6.2 Apoptosis

The apoptosis data will be presented in a table showing average percentage of whole cells for each sample along with the percentage of necrotic cells stained with PI. Appendix C contains tables of results containing percentage of whole cells, viable (V), early apoptotic (EA), late apoptotic (LA) and necrotic (N) populations. Each value will be noted with it's associated error.

3.3.6.3 Errors

For all calculations using averaged median values, the associated error has been calculated using the formula for standard deviation of the samples. However, in Appendix B, the errors on the mean have been calculated as the standard error of the sample. This is due to the small number of samples for each data point and therefore the expected greater distribution of values.

The propagation of errors, in cases where the fluorescence of the barcoded population has been taken away from the irradiated sample fluorescence, were calculated using Equation 3.3.2.

$$\begin{aligned} X &= Y \pm Z \\ \delta X &= \sqrt{\delta Y^2 + \delta Z^2}, \end{aligned} \tag{3.3.2}$$

where X is either the sum of Y and Z or the difference between the two. The error on X, δX, is therefore the quadrature sum of the errors on Y and Z, δY and δZ respectively.

For results which were obtained by multiplying or dividing values by one another, the following formula was used to calculate the errors.

$$\begin{aligned} X &= \frac{Y}{Z} \quad or \quad X = Y \times Z \\ \delta X &= \sqrt{(\frac{\delta X}{\delta Y} \times dY)^2 + (\frac{\delta X}{\delta Z} \times dZ)^2}, \end{aligned} \tag{3.3.3}$$

Chapter 4

Results

4.1 Developing Method

This section will be divided into the different phases of the experimental procedure. For each of these phases, the changes and developments which were made along the course of the project will be described and explained. These were made at different stages throughout the project in response to issues which arose and according to new findings from the obtained results and literature.

4.1.1 Cell Seeding

Seeding of the cells was always done by the same person in order to minimise potential variations. After initial experiments, and using the method developed previously at UiO [6], large dishes were used for both X-ray and proton irradiations.

4.1.2 Preparation

As the experiments progressed the levels of sterile practice were increased in order to prevent infections. After a number of infections, the different stages of the experimental procedure were investigated in order to determine the cause of the infections. The most likely solutions were considered to be the transportation method or perhaps a fault with a filter in either LAF bench. The results of this test were inconclusive, but the introduction of stricter methods for maintaining a sterile environment at all steps seemed to remove infections.

4.1.3 Irradiation

4.1.3.1 Dosimetry

Dosimetry for proton irradiations was performed using an ionisation chamber, the readings from which were used to calculate the dose being delivered to the cells in the three positions. Additional dosimetry was performed using EBT3 Gafchromic films. As the radius of the ionisation chamber was smaller than that of the dishes, the irradiated films were used to calculate the average value and homogeneity of the dose across the cell dish. These were irradiated in position one (the front of the Bragg peak) at the beginning of each experiment. Figure 4.1 shows an example of one of scanned films and the corresponding plot of the measured dose across the film. Appendix D contains the results of calculated dose from these films. These all showed acceptable levels of homogeneity and will not be discussed further.

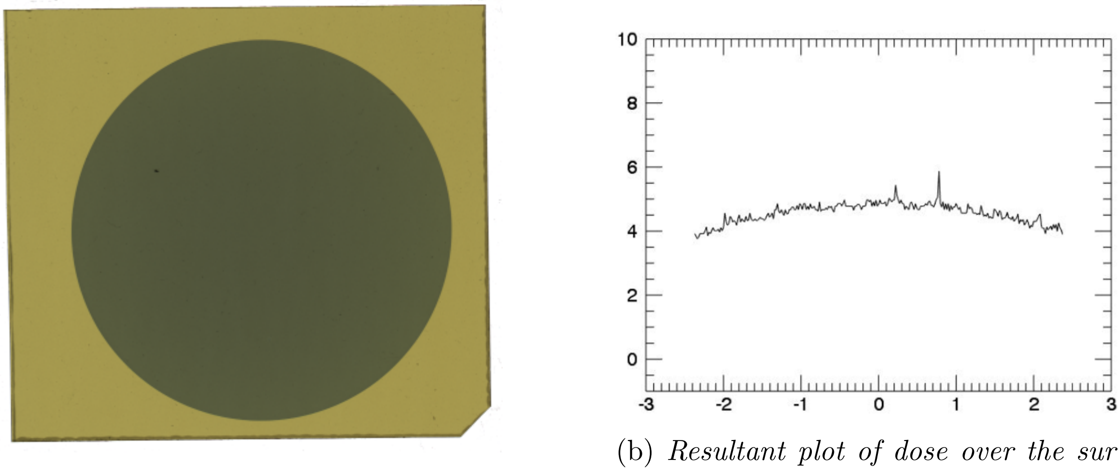

(a) *Scanned film from the Proton 3* experiment, irradiated with 5 Gy.*

(b) *Resultant plot of dose over the surface of the film.*

Figure 4.1: *Examples of an irradiated EBT3 film used for dosimetry and the resultant plot of dose over the surface of the film.*

4.1.4 Flow Cytometry Assays

4.1.4.1 Freezing

The following plot shows a test done to measure the effects of freezing the samples between processing. This method was introduced in order to make it possible to process all samples on the same day. Being able to do this increased the reliability of the method, allowing the same reagent mixes to be used for all samples in an experiment.

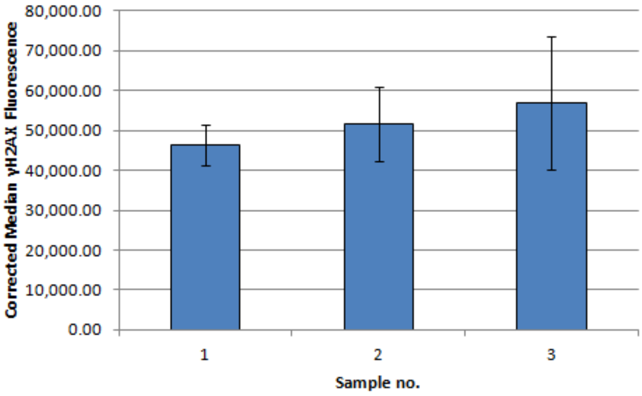

Figure 4.2: *Results from freezing experiment, testing procedure for γH2AX experiments. Irradiated with 5 Gy x-rays. 1 - Samples were fully processed immediately after irradiation. 2 and 3 - Samples processed up until step 9 in 6, then frozen in the permeabilisation buffer for two and five days respectively before the procedure was completed.*

It is important to note that after this experiment testing the method, the maximum number of days future samples were frozen for was 3 days.

4.1.4.2 Barcoding

Due to the drifting of the channels of the flow cytometer between experiments, fluorescent cell barcoding was introduced in order to provide an internal standard for normalisation of fluorescence data. Figure 4.10b shows an example of the signal produced for this additional population. The fluorescence of these barcoded controls was subtracted from the irradiated and control sample signals as an internal control.

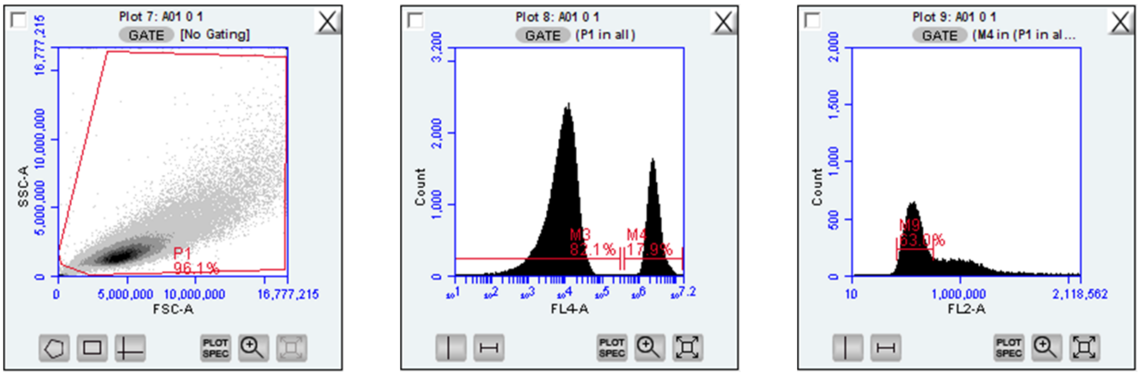

(a) *Viable whole cells from total mixed sample* (b) *Irradiated sample (left) and FCB control (right)* (c) *FCB control cells in G1 phase*

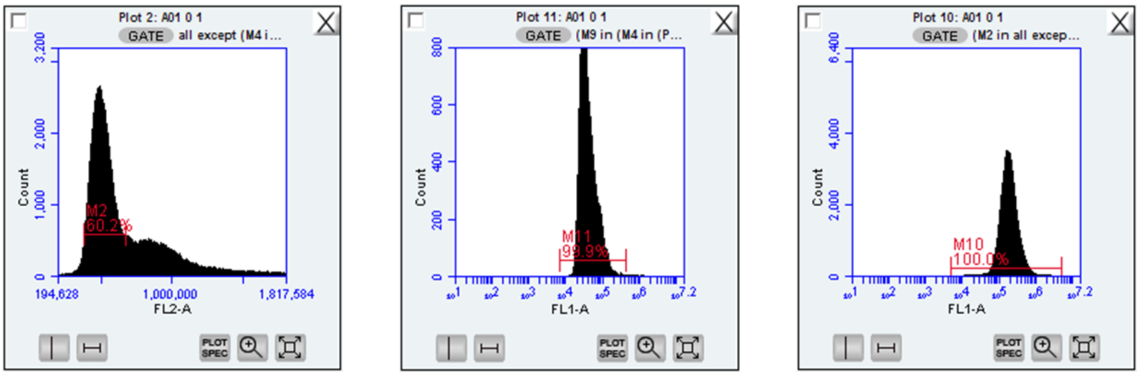

(d) *Irradiated cells in G1 phase* (e) *γH2AX fluorescence of FCB cells in G1* (f) *γH2AX fluorescence of irradiated cells in G1*

Figure 4.3: *Flow cytometry gating for γH2AX assay using fluorescent cell barcoding.*

4.2 Results

Table 4.1 shows a table of the experiments used for the final analysis in this study, showing radiation method, dose and the time points of the usable data. If applicable, any errors or additional information has been included in the notes column. These reasons will be explained in more detail in the discussion section of the report with considerations for future experiments.

1. Proton 1, the dishes and lids for 48 and 72 hours were mixed up during irradiation. This led to improved methods of labelling for future experiments.
2. X-ray 1, the samples for 72 hours were infected and had to be discarded. This led to testing of the different stages of the procedure to find cause of infections. More rigorous sterile techniques were introduced.
3. Proton 2, the wrong dish lid was used for calibration calculations, resulting in irradiation behind the Bragg peak. The unirradiated samples were then

Radiation	Dose (Gy)	Time points (Hrs)	Notes
Proton 1	10	0, 24	Front & back of BP
X-ray 1	10	0, 24, 48	N/A
Proton 2	5	0, 24, 48	Front of BP
X-ray 2*	2, 5, 10, 15	0, 48	Barcoding - doubled
X-ray 3*	5	0, 24, 48, 72	N/A
X-ray 4*	10	0, 24, 48, 72	N/A
Proton 3*	5	0, 24, 48, 72	Top & back of BP
Proton 4*	10	48, 72	Front & back of BP

Table 4.1: *Table of experiments used to obtain the final results for DSB measurements. Where * represents barcoded experiments using the larger cell dishes.*

used as an additional control group. Samples at 72 hours were infected and therefore discarded.

4. Proton 4*, the beam energy was changed inbetween experiment sets which meant that the 48 and 72 hour samples were irradiated with an unkown dose and were not included.
5. An additional proton experiment was run, but due to a faulty γH2AX antibody the subsequent results were unusable.

Each experiment was performed in triplicate, the results presented are therefore the average values with associated standard deviation values.

4.2.1 DSB Measurements

The raw data obtained from the flow cytometer for the fluorescence of the detected γH2AX was used in a number of ways. The uptake of γH2AX is expected to be proportional to the number of DSBs present in a sample. Figures 4.5a and 4.5b show the γH2AX fluorescence of the samples at different time points after irradiation.

It was expected that these values would decrease over time as repair of non-lethal damage is completed. Due to the nature of the damage induced by high and low LET radiations it was expected that the samples irradiated with high LET protons would have much higher initial and residual damages compared to low LET protons and x-rays.

Gating of the raw data, produced by the Flow Collect program was done as shown in Figure 4.4. Results show the values of corrected median γH2AX fluorescence for G1 cells with low PI fluorescence.

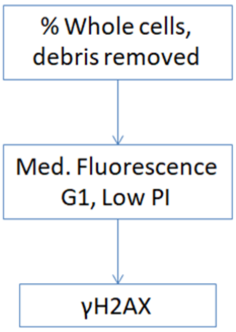

Figure 4.4: *Gating for samples processed with* γ*H2AX kit*

4.2.2 γH2AX Fluorescence

Figure 4.5 shows the results obtained for 5 Gy (4.5a) and 10 Gy (4.5b) irradiations. X-ray values for each time point were averaged for clarity.

There is a significant difference between the fluorescence seen for both the top and back of the Bragg peak in comparison to results for the front of the Bragg peak and x-ray. This is as expected as the higher dose rate and LET values cause a greater number of DSBs and induce more complex damage. Considering the similar results of γH2AX fluorescence for the top of the Bragg peak (dose = 22 Gy) compared to the back of the Bragg peak (dose = 5 Gy) an RBE value of at least 4.4 can be determined. This may be a slight underestimation as the fluorescence values for the back were higher than those for the top.

The increase in fluorescence seen at 72 hours for some of the experiments was unexpected and possible reasons for this will be discussed in more detail in the proceeding section.

In order to visualise the repair kinetics in the cells, the values for γH2AX floures-cence per Gy were normalised for each time point to the 0.5 hour results. These are as shown below in figure 4.6. It can again be seen from this plot the clear increase in fluorescence values for most experiments after 48 and 72 hours, with the back of the Bragg peak being the only one to continue to decrease.

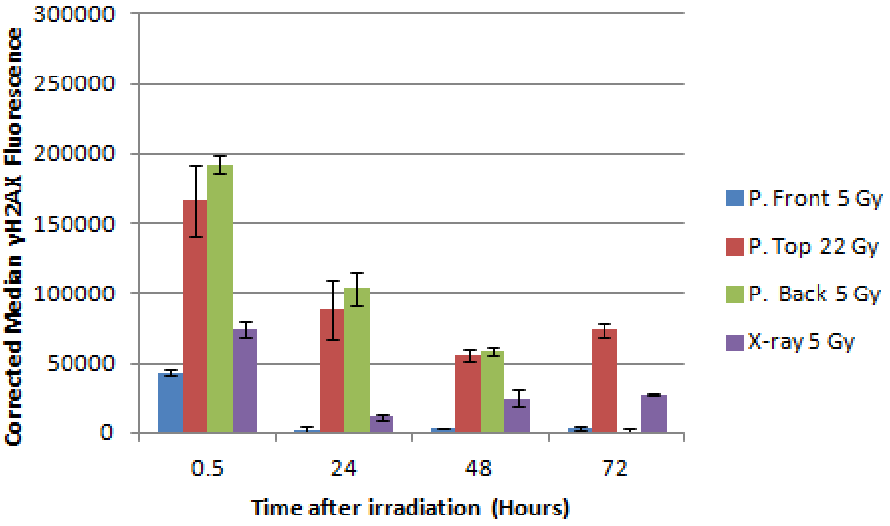

(a) *Plot of median γH2AX fluorescence for different time points after 5 Gy proton and x-ray irradiation. It is important to note that the dose at the top of the Bragg peak (P. Back) was infact 22 Gy, not 5 Gy. X-ray values are the average fluorescence from X-ray 2* and 3*.*

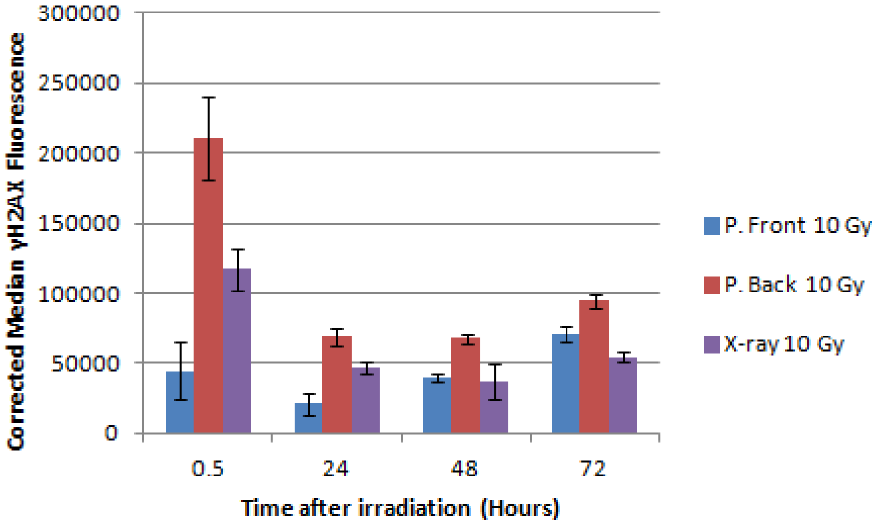

(b) *Plot of median γH2AX fluorescence for different time points after 10 Gy proton and x-ray irradiation. X-ray values are the fluorescence from X-ray 2* and 4*. Proton Front values are taken from two different experiments. Fluorescence values for 0.5 and 24 hours are taken from Proton 1, while the 48 and 72 hour values are taken from Proton 4*.*

Figure 4.5: *Plot of median γH2AX fluorescence for different time points after a) 5 Gy and b) 10 Gy proton and x-ray irradiation. Corrections were made to remove both background fluorescence and baseline fluorescence as per control samples for each time point. Errors shown are calculated using the standard deviation of the group. As shown in Table 4.1, each number refers to the date of the experiment and * defines experiments which used cell barcoding.*

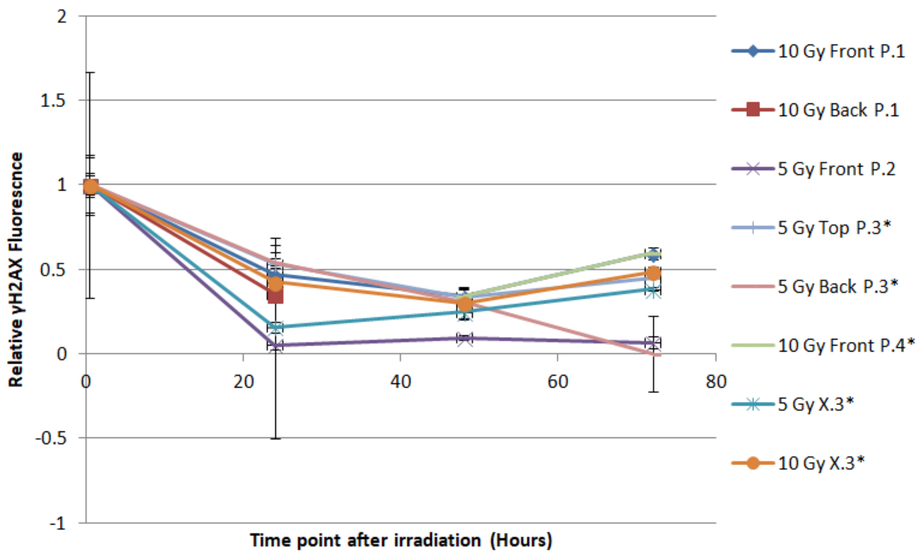

Figure 4.6: *Median γH2AX fluorescence per Gy, over time, for proton and x-ray experiments. Values have been normalised to the 0.5 hour values seen in Figure 4.7.*

4.2.3 γH2AX Fluorescence per Gy

From this raw data, values for the average fluorescence per Gy of dose given was investigated, corresponding to the number of DSBs per 1 Gy of dose for each radiation type, position and time point. Figure 4.7 shows that while the results for the front of the Bragg peak and x-rays give similar results, the values of fluorescence per Gy for the top and back of the Bragg peak are much higher, indicating a higher staining efficiency of the higher LET damages.

For cells irradiated in the back of the Bragg peak, there is a noticeably larger γH2AX fluorescence signal per Gy, compared to the low LET results at the same dose. Results obtained from the front of the Bragg peak appear to be consistent with the x-ray fluorescence values which, given the similar LET values, is understandable.

The fluorescence per dose was found to decrease with increasing dose. This is surprising and will be discussed later. However, the ratio between the high LET and low LET samples appears to remain roughly constant. This ratio of fluorescence per Gy, between the fluorescence for high LET compared average low LET values (protons in front of the Bragg peak and x-rays), was calculated. This was found to be 2.6 ± 0.5 for 5 Gy and 2.8 ± 0.6 for 10 Gy.

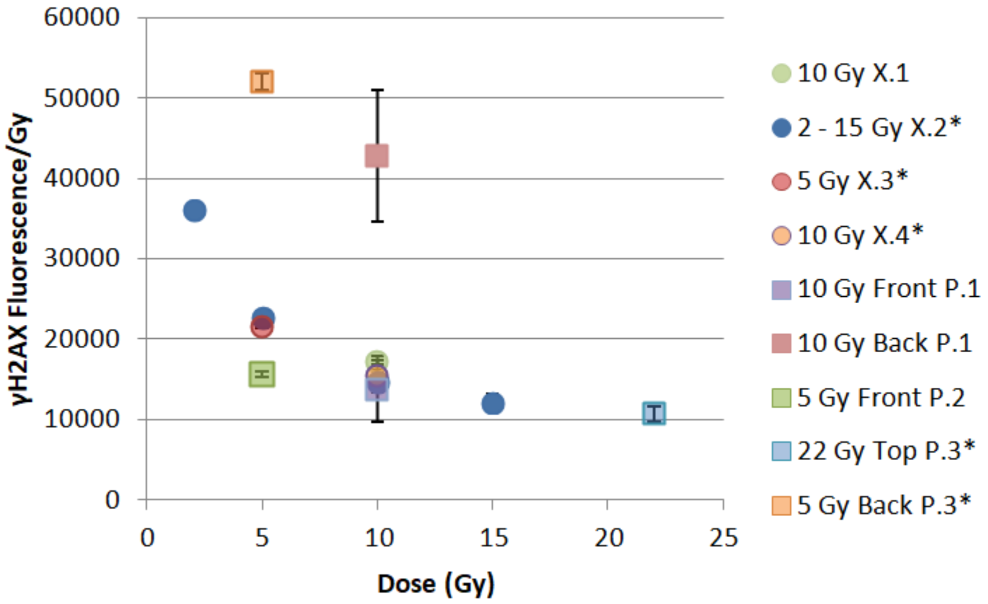

Figure 4.7: *Median γH2AX flourescence per Gy for proton and x-ray experiments at 0.5 hours after irradiation.*

4.2.3.1 γH2AX Peak Width Distribution

Considering the use of Median or Mean fluorescence for the H2AX data led to further investigation of the shape of the peaks in the obtained plots for this data. This was investigated by using the coefficient of variation percentages (CV%) values taken from the raw data collected on the Flow cytometer. The equation for this value is as defined below in Equation 4.2.1.

$$CV\% = \frac{S}{X} \times 100, \tag{4.2.1}$$

where S is the standard deviation of the fluorescence of the population and X is the mean channel number. This value therefore gives an indication of the variation in fluorescence values per cell within the samples. The results of this investigation are as plotted below, in Figure 4.8.

The shape of the plots were also investigated using calculated values for skewness. This was done using Pearson's equation for skewness,as described in Equation 4.2.2,

$$Skew = \frac{3(X - Md)}{S}, \tag{4.2.2}$$

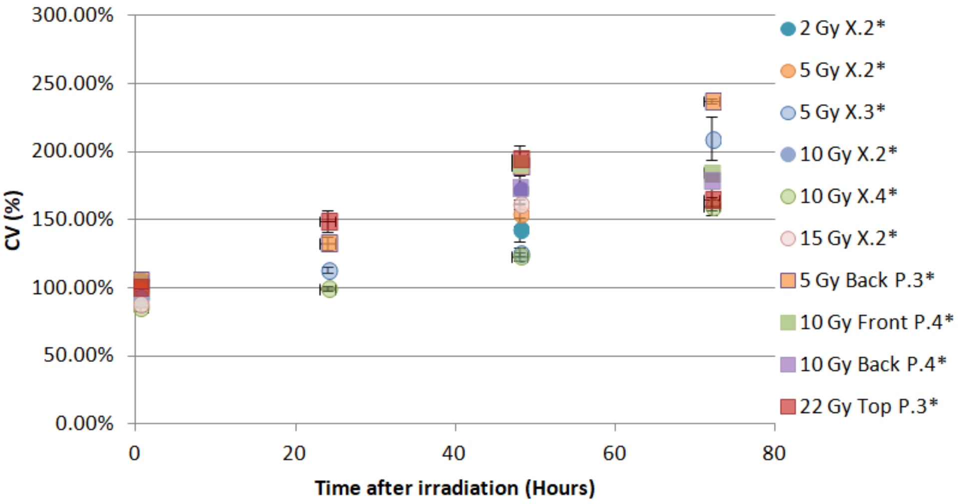

Figure 4.8: *Coefficient of variation percentage values*

where X is the mean of the population, Md is the median and S is the standard deviation of these values.

The results of these calculations return a quantitative measure how skewed the population is relative to the normal value. Negative results show a negative skew which is defined by a larger tail on the left of the population, while positive results show the opposite and are defined by a larger tail on the right of the population.

The results obtained are as shown in Figure 4.9 below, clearly showing a large positive skew for all samples. Little variation can be seen from these values across experiments.

4.2.3.2 G2 arrest

From the obtained histograms showing PI fluorescence it was possible to see the variations in the cell cycle distribution for the different time points across experiments. Figure **??** shows example histograms, obtained from 5 Gy proton irradiation for each time point. From these there is a clear variation in the percentage of cells in the different stages of the cell cycle.

In order to investigate this effect, analysis of the figures was done using the FCS express program. This models the DNA histograms in order to determine the percentage of cells in each stage of the cell cycle. Due to variations between experiments and the quality of the histograms produced this method proved difficult and was

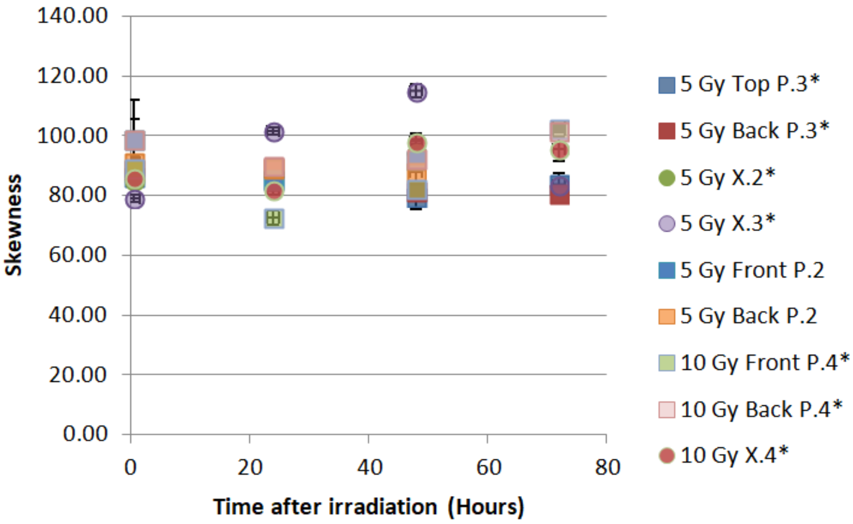

Figure 4.9: *Plot of calculated values for skewness for data from x-rays (X) and protons (P) over time. Values shown are the averages for each data set and error bars represent the standard deviation.*

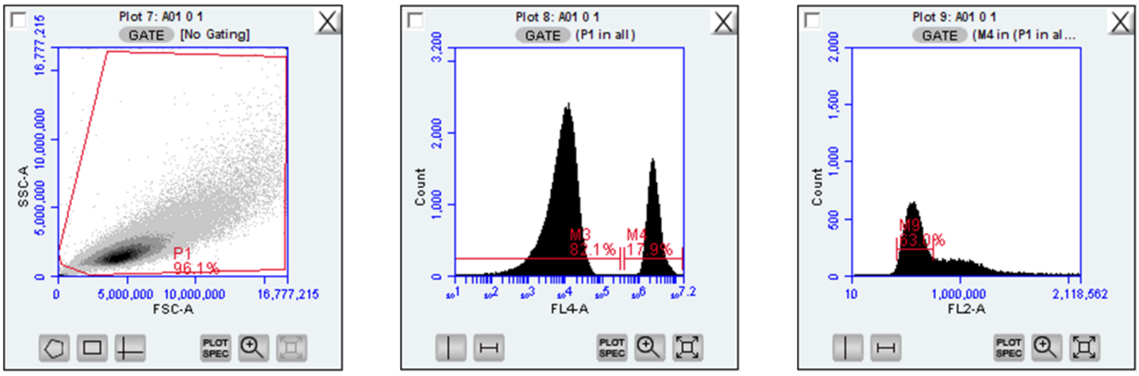

(a) *Viable whole cells from total mixed sample*

(b) *Irradiated sample (left) and FCB control (right)*

(c) *FCB control cells in G1 phase*

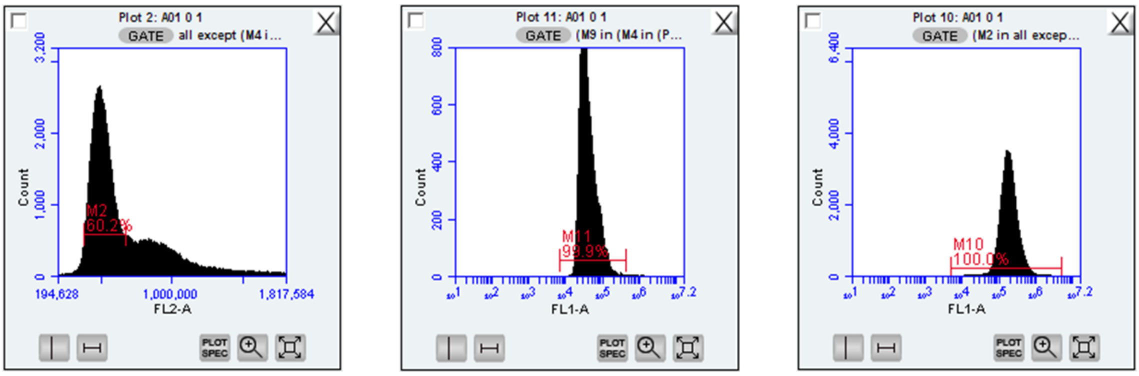

(d) *Irradiated cells in G1 phase*

(e) *γH2AX fluorescence of FCB cells in G1*

(f) *γH2AX fluorescence of irradiated cells in G1*

Figure 4.10: *Flow cytometry gating for γH2AX assay using fluorescent cell barcoding.*

not considered accurate enough to be used for all data. Figure 4.11 demonstrates example fits produced by this program for 5 Gy proton irradiation for each time point analysed. Figure 4.12 shows a plot of the percentage of cells in G2 phase after 5 Gy irradiation.

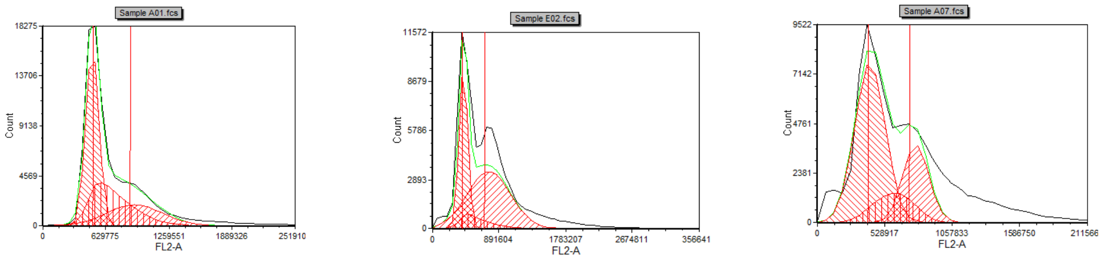

(a) *0.5 Hours* (b) *24 Hours* (c) *48 Hours*

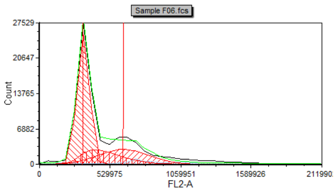

(d) *72 Hours*

Figure 4.11: *FSC analysis of cell cycle distribution after 5 Gy irradiation with protons in the back of the Bragg peak.*

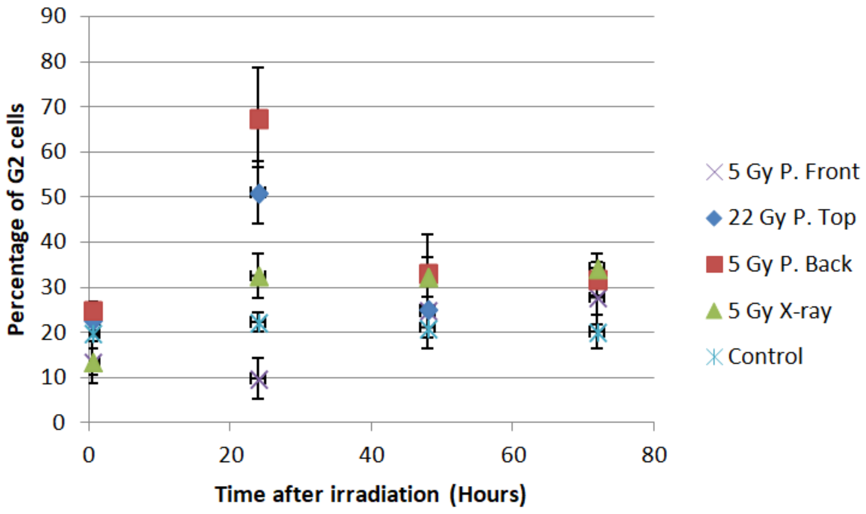

Figure 4.12: *Average percentage of cells in the G2 phase of the cell cycle for the analysed time points after irradiation with 5 Gy protons and x-rays. Note that the dose from the top of the Bragg peak was 22 Gy.*

From this a clear correlation can be seen for LET values and dose and G2 arrest at 24 hours after irradiation.

4.2.4 Apoptosis Measurements

For the Annexin V assay, each experiment was gated, as per Figure 4.13. This gave values for the percentage of viable, early apoptotic (low PI and high Annexin), necrotic and late apoptotic (high PI and high Annexin) cells. However, the number of experiments done to investigate the apoptosis levels in irradiated T98G cells were cut short due to very low apoptosis measurements. The possible reasons for this will be discussed in Section 5.3. Discounting the results for Annexin V-FITC staining, the data obtained for these experiments has instead focused on the uptake of PI as an indication of cell viability.

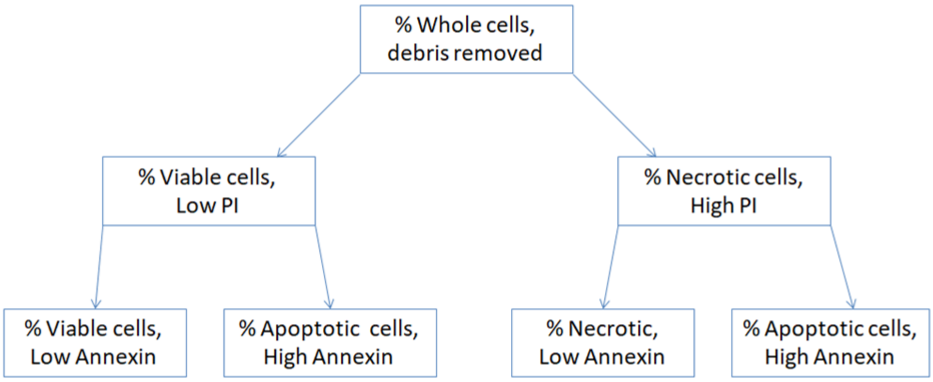

Figure 4.13: *Gating for samples processed with Annexin V-FITC kit*

Using the percentage of whole cells with high PI fluorescence to represent necrotic cells, the results are as tabulated below in Tables 4.2 and 4.3 for 5 Gy and 10 Gy experiments respectively, where each value is the percentage of whole cells. Viable cells were considered to be cells with both low PI and low Annexin fluorescence, indicating an intact cell membrane and no PS exposure. Apoptotic cells were taken to be those with low PI and high Annexin fluorescence. Finally, the necrotic population was taken as that with both high PI and Annexin fluorescence. Full tabulated results from these experiments can be found in Appendix C.

Radiation	Time (H)	Whole cells (%)	High PI (%)
Control	6	74.7 ± 4.5	4.6 ± 0.2
P Front	6	82.1 ± 1.3	4.2 ± 2.1
P Back	6	83.2 ± 2.2	3.2 ± 1.2
Control	24	57.6 ± 5.1	10.7 ± 2.0
P Front	24	71.2 ± 0.6	5.3 ± 1.1
P Back	24	75.6 ± 3.5	3.8 ± 1.2
Control	48	79.2 ± 2.9	5.2 ± 1.6
P Front	48	71.3 ± 4.0	8.5 ± 1.8
P Back	48	76.6 ± 2.2	2.9 ± 0.4
Control	72	76.3 ± 4.2	4.8 ± 1.3
P Front	72	69.2 ± 2.7	10.7 ± 1.5
P Back	72	77.5 ± 2.3	5.7 ± 0.3

Table 4.2: *Tabulated values for percentage of viable cells remaining after 5 Gy irradiation. Values shown are the average percentage of whole cells in each sample with low PI uptake. Errors are the values of standard deviation for each data set.*

Radiation	Time (H)	Whole cells (%)	High PI (%)
Control	6	64.1 ± 5.5	6.5 ± 1.2
P Front	6	31.72 ± 25.8	29.1 ± 20.3
P Back	6	50.2 ± 7.7	15.5 ± 1.4
P Front	24	44.1 ± 4.0	34.3 ± 7.8
P Back	24	39.0 ± 14.7	23.9 ± 5.4
P Front	48	34.5 ± 10.1	41.7 ± 20.0
P Back	48	28.0 ± 8.8	55.2 ± 6.2
Control	72	65.3 ± 4.1	11.6 ± 0.3
P Front	72	22.7 ± 5.3	52.5 ± 1.2
P Back	72	16.7 ± 4.2	49.6 ± 2.8
Control	3	37.3 ± 3.6	24.2 ± 0.3
X-ray	3	33.9 ± 1.8	24.5 ± 3.8
Control	24	39.6 ± 2.0	13.8 ± 1.0
X-ray	24	38.4 ± 6.3	15.1 ± 3.9
Control	48	43.4 ± 4.3	16.1 ± 1.0
Control	3	37.3 ± 3.6	24.2 ± 0.3
X-ray	3	34.0 ± 1.8	24.5 ± 3.8
Control	24	39.6 ± 2.0	13.8 ± 1.0
X-ray	24	38.4 ± 6.3	15.1 ± 3.9
Control	48	43.4 ± 4.3	16.1 ± 1.0

Table 4.3: *Tabulated values for percentage of viable cells remaining after 10 Gy irradiation. Values shown are the average percentage of whole cells in each sample with low PI uptake. Errors are the values of standard deviation for each data set.*

4.3 Additional Experimental Results

A number of additional experiments were performed in order to test unexpected results seen during initial analysis and to test the procedure being used.

Due to the increase in γH2AX fluorescence seen at 72 hours it was thought that there was perhaps an insufficient amount of antibody available to the cells. This fluorescence increase coincided with a greater number of viable cells surviving after processing. Due to inexperience with the handling of cells a large percentage of the samples were lost during processing in the initial experiments. Improvement in the procedure along with increased cell dish size resulted in a much larger number of cells remaining in the final experiments.

If too little antibody was being used for staining of the samples the full extent of the damage would not be detected. Therefore for the initial time points, with the greatest number of damages, the signal produced would be an underestimation of the true extent of DSBs.

This theory was tested by performing an experiment using samples irradiated with x-rays at 5 Gy. Processed after 30 minutes, half were given the usual amount of γH2AX (sample 2) and the other half were given double (sample 3). The results of this are as shown plotted in Figure 4.14. An additional group was included, these samples were placed on ice immediately after irradiation and then processed straight away. This was done in order to test the reliability of the 0.5 hour time point. 0.5 hours was used in order to allow time for the formation of γH2AX foci, but also allowed time for repair of sublethal damage.

The results regarding dye concentration were inconclusive, one sample in the group with normal antibody concentration was significantly lower than the other two, this resulted in the large error as shown in Figure 4.14. It would be useful to repeat this experiment again for a larger sample group and more time points in order to test this theory further. However, the sample placed on ice, verified that the time point of 0.5 hours ensured that the γH2AX foci had sufficient time to form.

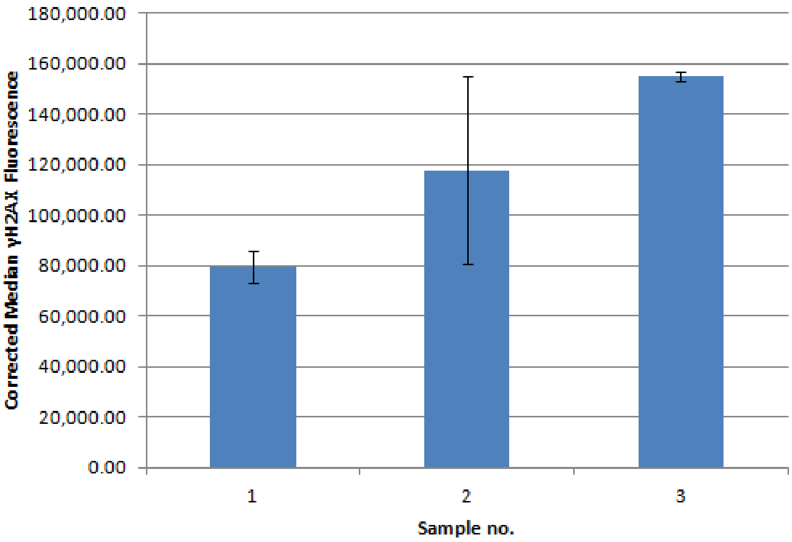

Figure 4.14: *Results from final experiment testing procedure for* γ*H2AX experiments. Irradiated with 5 Gy x-rays. 1 - Samples were placed on ice and processed immediately after irradiation. 2 - Samples were processed 30 minutes after irradiation using the usual amount of antibody. 3 - Samples were processed 30 minutes after irradiation using double the usual amount of antibody. Corrections were made to remove both background fluorescence and baseline fluorescence as per control samples for each time point. Errors shown are calculated using the standard deviation of the group.*

4.3.0.1 Control procedure

Control samples underwent the same procedure as irradiated samples before processing. For example, control samples in proton experiments were removed from the incubator and had the medium removed for the average amount of time of the samples for that time point. Preferably the entire procedure of transport to and from the cyclotron would have been reproduced for the controls, but due to time restraints this was impractical. However, from proton experiment number 2, where the cells were placed out of range of the beam, we can see that the unirradiated samples, which were taken through the entire procedure, were extremely similar to the controls which were not, as seen in Figure 4.15 and all within the error bounds.

It can be concluded from this that the method used for the unirradiated control samples in the different experiments was accurate enough to model the full procedure undergone by the radiated samples.

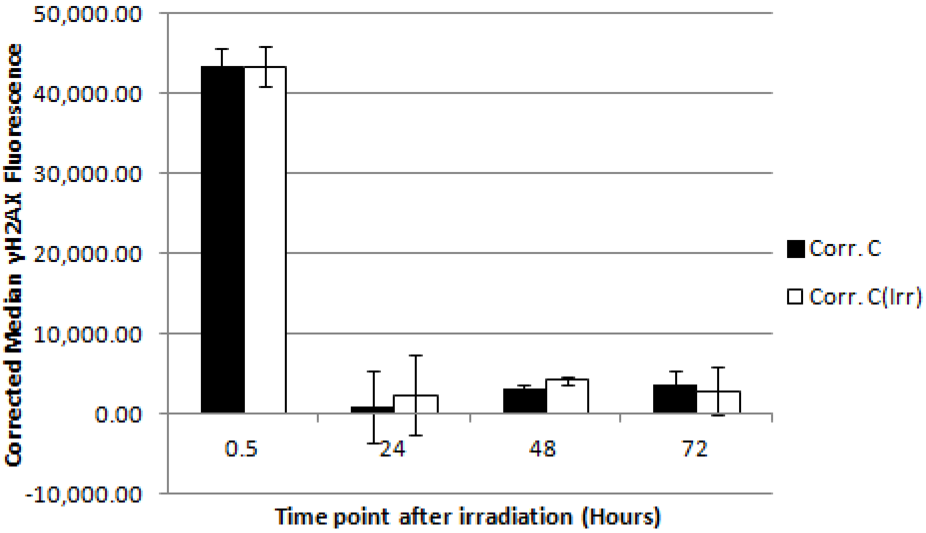

Figure 4.15: *Comparison of typical control samples (Corr. c) vs. samples which underwent full procedure (Corr. C(Irr)). Showing the corrected median γH2AX values with their associated standard deviation.*

Chapter 5

Discussion

5.1 Methodological Considerations

5.1.1 Cellular Variations

Working with living cells presents a range of uncontrollable uncertainties. It is extremely difficult to exactly replicate the same conditions for the samples from week to week. Once unfrozen, the cells can have varying growth rates, which can result in different cell numbers for experiments. Due to these variations the results for each experiment have been calculated with respect to the unirradiated control samples for each time point and dose same day.

For proliferating cells, small uncertainties due to the different stages of the cell cycle may also occur. It is known that the induction of DSBs, and their subsequent repair, will vary depending on the phase of the cell cycle in which the damage occurs [52].

Every effort was made to ensure the specified times after irradiation were as accurate as possible. However, due to the limitations in number of samples which could be processed at a time and the increasing number of samples to be processed each day after irradiation, some variation in these timings was unavoidable. Therefore, some samples may have had a slightly longer amount of time to initiate repair than others.

Whilst every care was made to maintain the temperature of the cells during experiments, there were a number of factors which made this challenging, particularly transportation of the dishes. In order to maintain the temperature, the dishes were transported along with sterilised flasks of water heated to 37°C. During x-ray irradiation steel dishes were placed onto a preheated surface while a heated cell dish holder was used for all proton experiments.

Changes in environment may cause proliferating cells to go into cell cycle arrest. As non-cycling cells have more time to repair damage, it was important to minimse the time each sample spent without medium. For samples which had the medium removed prior to irradiation there will be some increase in pH over time. If left without medium for too long this change in pH may lead to cell death. Previous experiments at UiO showed that the time taken to irradiate cells using x-rays without medium had a negative effect on survival results compared to those conducted with medium [6]. As proton experiments had to be performed without medium, due to the vertical irradiation position, the time the cells spent without medium was noted for each sample. Therefore if any unusual effects were seen in the flow cytometry results it was possible to consult this information. There were no samples which proved to be affected by this time point.

5.1.2 Proton Irradiations

Dosimetry was performed prior to each proton experiment, each day, in order to assess the dose rate and find the position of the Bragg peak. From these calculations, results of the number of monitor chamber units to be delivered and the positioning of samples can be found tabulated in Appendix D. In is important to note that care was taken to deliver the same number of monitor chamber units to all positions during irradiation.

Due to the steepness of the back of the Bragg peak, positioning of the samples was extremely important. Any alteration to the position of the cells would result in a considerable difference in dose rate relative to the presumed value. Simulations of the experimental setup of proton setups at UiO have been modelled using Monte Carlo [49] and are as demonstrated in Figure 5.1.

Due to the steepness of the back of the Bragg peak, the dose rate will vary significantly for slight changes in position. From the thorough dosimetric results obtained from proton experiment 3, dose rate measurements were calculated for 3 mm increments in the back of the Bragg peak. These showed that a change in depth of air of 3 mm resulted in an average variation in the dose rate of 8 %.

Therefore if the holder was moved slightly, or the dish wasn't fully placed inside the holder or even if the parafilm was stretched too tight or not secure it could result in the sample receiving too much or too little dose. During one of the proton experiments we saw the effects of slight discrepancy of positioning. A systematic error in distance of 0.2 mm was implemented for all dishes irradiated in position two. This was due to the wrong type of dish lid being used to calculate the position. Due to this difference in positioning all of the cells irradiated in this position were outside of the Bragg peak and received effectively no dose. These dishes were therefore used as an additional control group and were compared to the control dishes as per Figure 4.15. From Figure 5.1 it is also important to note the effect of increasing proton energy on both the LET and energy spectrum.

The temperamental proton beam from the OCL resulted in a sometimes significant variation in beam intensities during experiments. In order to later account for this the monitor chamber units were noted for each irradiated sample in order to more accurately calculate the precise dose given. It is however impossible to determine any changes in beam energy during irradiations and these changes can only be observed after analysis of the results.

For one experiment, proton 4*, the beam intensity dropped mid experiment and in an attempt to correct this, the energy was unintentionally decreased. This resulted in the loss of results for the 0.5 and 24 hour samples, as the dose rate was unknown for the remaining irradiations. This emphasised the importance of performing thorough dosimetry before the experiments. It was not possible to deliver the exact doses planned during these experiments. However, the exact beam flux delivered to each sample was known, as the monitor chamber reading was noted for each sample. These values were then converted into a delivered dose value for each sample.

As well as the human error associated with these experiments there will also be

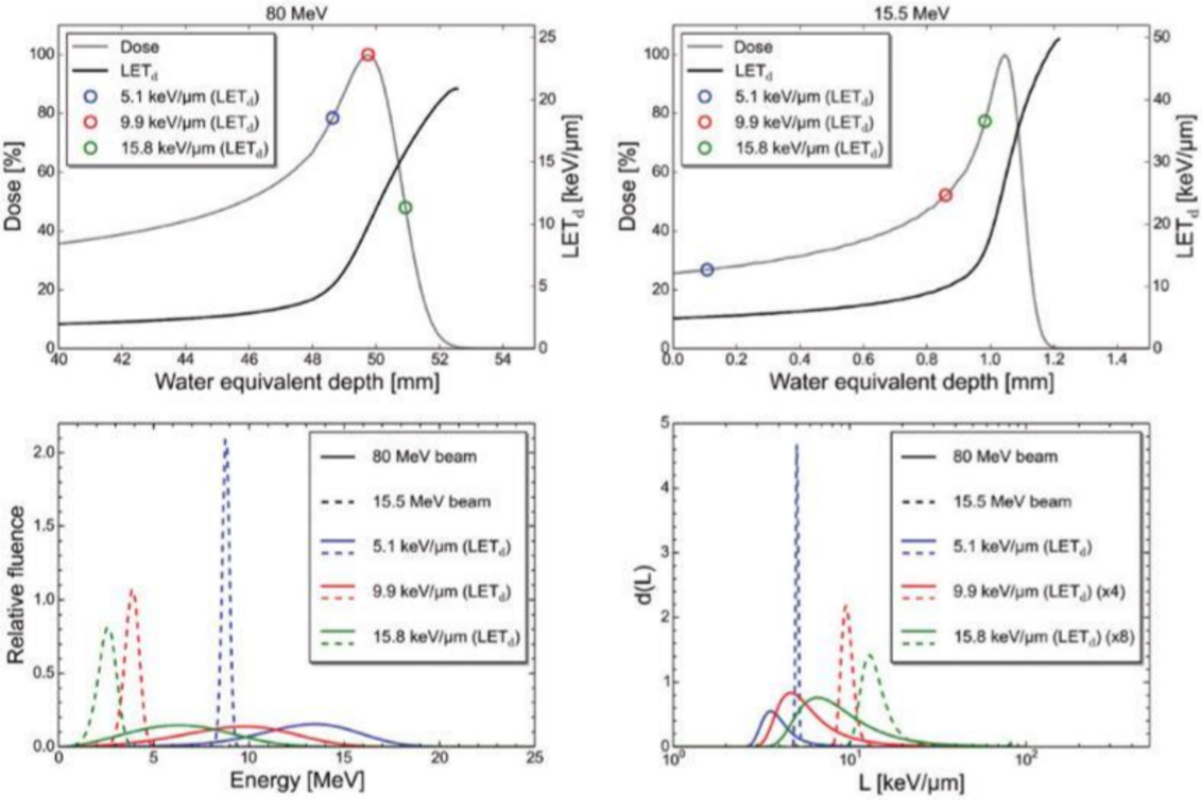

Figure 5.1: *Monte Carlo model of the experimental proton set up at UiO [49]. Showing dose and* LET_d *values as a function of water equivalent depth for 15.5 MeV and 80 MeV protons. Circles mark the location of three specific* LET_d *values at the defined depth dose profiles (upper panels). Energy spectra (lower panels, left) and dose weighted LET spectra (lower panels, right) corresponding to the three marked* LET_d *values, for both beams. Scaling of some of the LET spectra is shown in parenthesis in the legend.*

errors associated with the equipment used. Errors in the fluctuating dose rate, but mainly the positioning of the samples will be the contributing factor. Systematic errors from the electrometers were not considered to be important, as these will be much smaller than those already discussed.

Film irradiations showed that the homogeneity of the beam was reduced significantly in the back of the Bragg peak [6]. This effect was due to shielding by parafilm and the dish lids. Therefore the variation of the average dose to the cells may be slightly larger than suggested by the film irradiations with no shielding.

5.1.3 Flow Cytometer Assays

With the many different stages of aspiration, washing, incubation of samples in the relevant antibodies and then filtering, there will inevitably be some variation between experiments. The utmost care was taken to ensure that the samples processed on the same day were treated identically, but human error would result in small variations.

As experiments were processed over a number of time points there would also be some error in between the different days of processing. To minimise this error, each time point was part processed and then frozen so that the final antibody staining and flow cytometer analysis was performed on the same day. This allowed the antibody mixes to be prepared for all samples in an experiment simultaneously, thus reducing errors in variation in antibody concentration and variation. This also reduced potential differences in the flow cytometry analysis as the channel assignments are known to shift from day to day.

Variations between experiments will be caused by degradation of the quality of the antibodies and other reagents. Due to the time period over which the experiments were performed, this error was unavoidable, but due to the control samples used for each time point it was considered to be of little importance.

It is important to note that the signals obtained using the flow cytometer do not accurately show the results for the entire sample. Trypsinisation and washing of the samples will result in the removal of some necrotic cells and debris. It has been shown that higher doses and higher LET irradiation results in decreased cell survival, as shown in Figure 5.2, with values taken from Anne-Marit Rykkelid's Master thesis [6]. The following values of surviving fraction after 5 Gy and 10 Gy were taken from Figure 5.2.

Radiation	SF (5 Gy)	SF (10 Gy)
X-ray	0.5	9×10^{-2}
Proton Front	7×10^{-2}	2×10^{-3}
Proton Back	8×10^{-4}	9×10^{-7}

Table 5.1: *Calculated values for the surviving fraction of T98G cells after irradiation with protons at x-rays at UiO [6].*

Therefore, it is to be expected that samples receiving a higher dose or irradiated

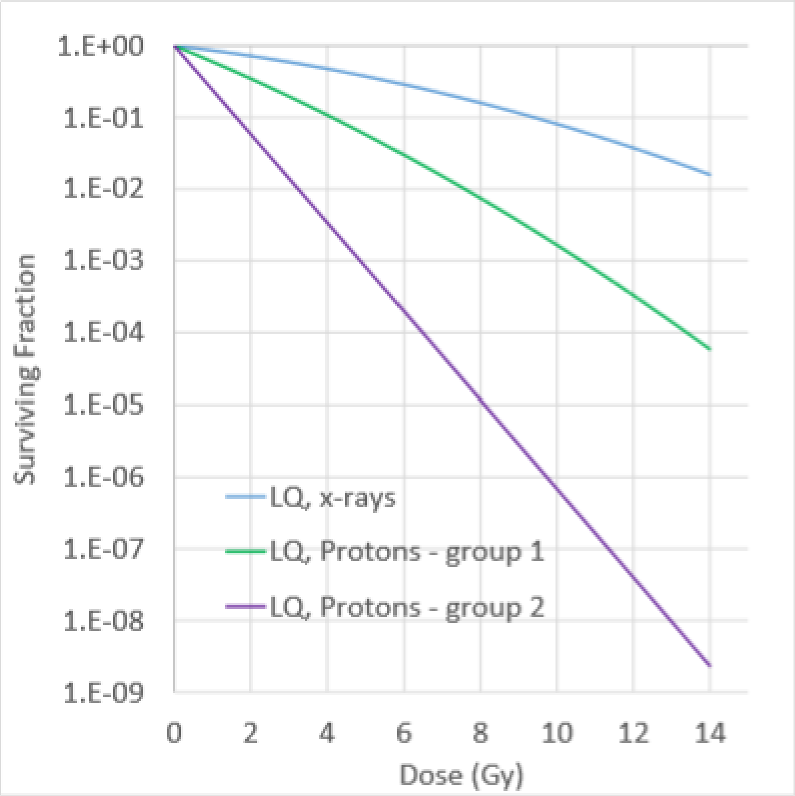

Figure 5.2: *LQ fit of clonogenic surviving fractions of T98G cells after irradiation with 220 keV x-rays (Blue), front of the proton Bragg peak (Green) and back of the proton Bragg peak (Purple). Front and back of the Bragg peak had an average LET of 7.5 and 41 keV/μm respectively.*

with a higher LET value will lose a greater number of cells compared to those subjected to low dose or low LET radiation. There will also be less proliferation within the population due to cell cycle arrest for these cells. Thus, at later time points, the amount of whole cells compared to debris might have been used as a measure of cell survival. The experiments done using the Annexin assay were expected to reflect this. However, in some cases the percentage of whole cells was greater for irradiated samples than for the control samples. This indicates that the washing procedures of the assay remove varying amounts of debris. This did not appear to have an impact on the γH2AX assay results, but must be considered as an additional source of error.

5.2 γH2AX experiment results

In order to investigate the effects of proton irradiation on T98G cells, two different doses, 5 Gy and 10 Gy, were used. For 5 Gy irradiation, cells were irradiated either before the Bragg peak (LET = 5 - 10 keV/μm), in the top of the Bragg peak (LET = 22 - 28 keV/μm) or the back of the Bragg peak (LET = 38 - 44 keV/μm). Utmost care was taken in order to obtain the same dose rate for irradiations done before the Bragg peak and in the back of the Bragg peak. This was done by adjusting the distance in air. Monitor chamber readings were then calibrated by the ionisation chamber measurement in order to deliver the exact dose. This value, which defines the flux delivered to the cells, was also used when irradiating cells at the top of the Bragg peak. Due to the higher dose rate of this position, this resulted in a dose of 22 Gy to cells in this position compared to 5 Gy for the other positions. These results were all compared to 220 kV x-ray irradiations of the same dose, with an LET of 3.6 keV/μm [50].

5.2.1 Initial γH2AXluorescence (0.5 hours)

The first time point chosen to perform the analysis of induced damage was 0.5 hours after irradiation. This time point was chosen for practical reasons - some time was needed after irradiation to transport the samples and prepare for processing. Also, from literature, it is possible to see that at 0.5 hours γH2AX should have reached a plateau value [53]. As the formation of γH2AX foci begins just a few minutes after DSB induction (within 1 - 3 minutes) it was considered that at 0.5 hours there would have been sufficient time for the repair of some sublethal damages. Therefore this time point was tested, as demonstrated in Figure 4.14, by placing samples onto ice immediately after irradiation and processing as soon as possible. This test showed that the fluorescence signal was increased for samples processed in the usual way, at 0.5 hours, compared to those placed onto ice and processed immediately. This verifies that the phosphorylation of γH2AX takes time to reach a maximum, making 0.5 hours a suitable time point for DSB analysis.

From the plot of γH2AX fluorescence after 5 Gy irradiation (fig 4.5a). It is possible to see the differences produced for different LET values. Higher LET values clearly produced more DSBs compared to the lower LET radiation. The results for the front of the Bragg peak are comparable to those of the x-rays. Figure 4.7 reinforces this, showing the much greater impact of LET on induction of DSBs compared to dose. The DSBs for high LET 5 Gy irradiation were even greater than the number caused by 22 Gy irradiation (also with relatively high LET). High LET irradiation results in much greater γH2AX fluorescence per Gy of dose.

From Figure 4.5b it is possible to see the same effect for the results obtained after 10 Gy irradiation. It could be expected that doubling the dose delivered to the samples would double the amount of damage induced. Even though it was higher for 10 Gy, it was not double the values obtained for the 5 Gy fluorescence. However, this could be due to time period over which the experiments were obtained. The results for 10 Gy are taken from initial experiments and therefore have much fewer surviving cells. They were also processed with a different batch of the assay kit. These factors could contribute to differences in the experiments which would mean they cannot be compared directly.

It can also be seen that results obtained for the front of the Bragg peak for both groups are extremely similar to x-ray fluorescence results for the same dose. It can be seen that the x-ray results generally seem to be slightly higher than those from before the Bragg peak. It was expected that this would be the opposite, due to the higher LET value of the protons (5 - 10 keV/μm compared to 3.6 kev/μm for x-rays in this setup [50]). However, these variations were considered to be insignificant and were perhaps due to variations in the setup of the experiments.

It stands to reason that the fluorescence of both the top and the back of the Bragg peak will be greater than the other results. The higher dose and dose rate in the top and the higher LET value in the back of the Bragg peak should induce more DSBs. The front of the Bragg peak and x-rays have significantly lower LET values. Due to clustering of the energy deposited by higher LET radiations the damages induced will be more complex [54].

5.2.1.1 γH2AX Fluorescence per Gy

Using the raw data for the detected γH2AX fluorescence, the median fluorescence per Gy was calculated. This was done by dividing the γH2AX fluorescence values by the delivered dose. The differences in these values indicate the effects of different doses and LET values on the induction of DSBs.

At 0.5 hours after irradiation there will have been little repair or cell death. Therefore these results can be taken as a representation of the number of DSBs caused by the different types of radiation. The highest values of fluorescence produced per Gy can be seen for the back of the Bragg peak for both 5 and 10 Gy. Figure 4.7 shows that the ratio of high and low LET results, at both 5 and 10 Gy, is roughly the same. This was found to be 2.6 ± 0.5 at 5 Gy and 2.8 ± 0.6 for 10 Gy. These values demonstrate how much more damage is induced by higher LET radiation.

Considering the mechanisms at work it was expected that the γH2AX signal produced per Gy would have been relatively linear for each type of radiation. From the results of the X.2* experiment in particular, which consisted of 2 - 15 Gy x-ray irradiations, it was expected that the results obtained 0.5 hours after irradiation would show similar fluorescence values per Gy. However, this was not the case and a decrease in γH2AX fluorescence per Gy was seen with increasing dose (fig 4.7).

The concentration of γH2AX antibody was originally tested with T-47D cell [N. Edin, personal communication]. In the first experiments with T98G cells, some samples ended up with very few cells, but no difference in the position of the fluorescence peak was seen. However as the experiments improved, and with the introduction of larger dish sizes, the cell number per sample may have exceeded a threshold for the antibody concentration. Thus, not all γH2AX foci would have been dyed. To test this theory an experiment was done with double the initial amount of γH2AX antibody. However this proved to be inconclusive and requires further investigation.

5.2.2 γH2AX Fluorescence at 24 Hours

For the second time point, 24 hours after irradiation, it is expected that the cells will be arrested in the G2 checkpoint as confirmed by Figure 4.12. Therefore, cells should not have been lost to other processes such as apoptosis or necrosis. The decrease in γH2AX fluorescence at this time point therefore gives an indication of the repair of the initial DSBs.

5.2.3 γH2AX Fluorescence at 48 Hours

At 48 hours the variation between fluorescence signals from varying LET and dose is greatly reduced. For both 5 Gy and 10 Gy, signals from different positions in the proton track are much closer to the x-ray fluorescence signals. At 48 hours the G2 arrest of the cells, seen at 24 hours (fig 4.12), is seen to have diminished, indicating that the majority of cells have begun proliferation again. This may result in both a loss of cells with irreparable damages and also possible induction or replication of DSBs in the progeny of damaged cells. This could explain the less significant decrease in signal seen between 24 and 48 hours compared to that of 0.5 to 24 hours. It is also reasonable to consider that any reparable damage has been repaired and this signal at this time point represents residual, irreparable damage.

5.2.4 γH2AX Fluorescence at 72 Hours

The plots of γH2AX fluorescence over time for both the 5 Gy and 10 Gy data groups show an increase in DSBs at 72 hours. This was an unexpected result as we would expect either continued repair of DSBS to further decrease the signal, or a stagnation of the signal seen at 48 hours. A number of reasons for this increase in fluorescence have been considered.

5.2.4.1 Increased γH2AX Fluorescence at 72 Hours

In order to compare these results it is important to consider the relative number of cells being analysed in each experiment. The initial proton experiments were performed using small dishes whereas the latter used larger dishes. This, coupled with the noticeable improvements in the experimental procedure over time, resulted in a much greater number of viable cells in the final experiments. Therefore, looking at the percentages of whole cells analysed and the counts in each experiment gives an indication of the quality of the procedure.

Also the cells were gated to remove the debris and thereby only include the expected viable cells. Therefore, the plotted values are not absolute values for the levels of γH2AX phosphorylation, but simply the values for that percentage of the viable population remaining.

With fewer surviving cells at 72 hours the hypothesis of too low dye concentration is relevant here, as discussed in Section 5.2.1.1. However, the experiment to test this theory was inconclusive (fig 4.14). If the observation is not an experimental artefact then other explanations should be considered.

One explanation considered was that the increase in signal seen at 72 hours was due to saturation of damage. The number of detectable DSBs is limited in this method by the saturation of DSBs on one strand of DNA. If a strand of DNA receives many hits in one place, the phosphorylation will only occur once, and therefore be detectable at one site [55, 56]. It can therefore be understood that the amount of γH2AX would be under-reported for higher LET or higher doses as the damage would quickly reach a so called saturation limit. Once this limit is reached for a sample, any further damage would effectively be unnoticed in the obtained results. This could explain the discrepancy between the signals detected for 10 Gy compared to 5 Gy.

Other potential reasons for an increase in the number of DSBs at this point could be due to residual foci from the initially damaged cells. If the repair of the chromatin structure is incorrect or incomplete there may be some residual γH2AX foci [57]. These are not necessarily indicative of true DSBs, but merely poor restoration of the chromatin structure. It has been found that large residual γH2AX foci form several hours after irradiation [55] and it may be the proliferation of cells with such foci which result in this apparent signal increase.

It would also be reasonable to believe that there would be an increase in damages within the population at this time point. Stress within the cells after irradiation can cause the formation of additional γH2AX foci up to 48 hours after irradiation [58]. Such stress causes increased production of reactive oxygen species (ROS) by mitochondria [59] the resultant DSBs from this process could then contribute to the fluorescence detected. The effects of this on mitochondrial DNA is dependent on the LET properties of the radiation [60] as well as the duration of exposure [61] and the mechanism of G2 arrest [62].

The delayed effect of genomic instability after ionising radiation has been widely studied and could also contribute to this fluorescence increase. After high LET radiation the surviving population of irradiated cells will contain a large amount of damage which will be propagated to their progeny [63]. This will appear as persisting damage and it is such damages which are connected to potential malignancy [64, 65]. This effect is therefore to be expected and coincides with the known aggressiveness of this type of tumour. It is also possible for γH2AX foci to form during stalled replication [66] and if the G2 arrest seen is reliable, increased levels of γH2AX after this point would be expected.

Finally, it was considered that this could have been an effect of the freezing procedure, as the 72 hour samples were the only ones which had not been frozen. However, from Figure 4.2 it can be seen that the samples which were frozen for the longest period of time actually had a slight increase in fluorescence compared to those processed immediately. This therefore discounts the theory of this increase being an artefact caused by the 72 hours not being frozen before processing and supports the hypothesis that new DSBs are formed over time, even in frozen cells. Freezing could also make the cells more susceptible to genomic instability and more detailed investigations should be done into these effects.

5.2.5 Peak Width and Skewness

From the differences in fluorescence, seen for the different radiation types, two methods were used in order to analyse the distribution of γH2AX fluorescence for different doses. The first method was analysis of the coefficient of variation (CV) percentage values, indicating the variation within the peaks. The second was the calculation of the skewness of the peaks, giving a quantitative value for the distribution of each

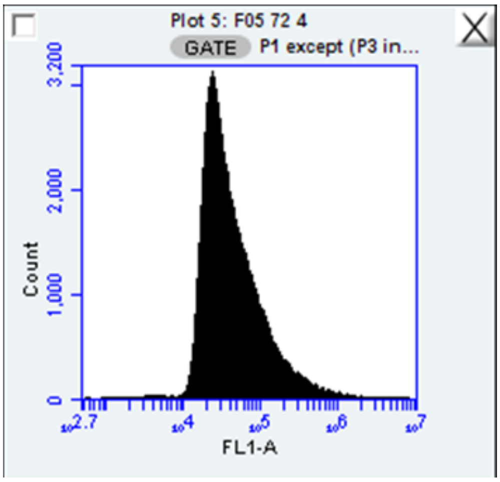

Figure 5.3: *Example plot of visible positive skew of γH2AX fluorescence peak.*

sample fluorescence.

The CV percentage values were found to increase over time. This reflects a larger distribution of DSBs per cell which could be caused by a number of processes, including replication of DNA with DSBs due to genomic instability and increased ROS production as described above. In addition to these mechanisms inducing further damages, some repair may take place which would also affect the distribution of signals.

The results for the calculated skew values showed very little variation between time points or radiation types. All showed a high positive skew, generally between 60 and 100. This shows that all fluorescence peaks had a larger tail on the right of the peak as demonstrated by Figure 5.3. This could be an indication into the detection capabilities of the flow cytometer or the γH2AX assay as these higher fluorescence values could be caused by the combining of signals from separate foci. However, it could also arise from including some S-phase cells in the G1 gating of the samples as the Flow Collect gates do no account for an overlap between phases.

It was thought that these values could give an insight into the distribution of the levels of γH2AX fluorescence over different time points, but this proved inconclusive. As the values for the controls were all within the same range as the irradiated samples it was concluded that the symmetry of the peaks provides no useful information regarding changes due to radiation induced damage. However, due to the very small variation between experiments, these results suggest that the method of gating and detection was consistent. It was considered that the shape of the peaks could potentially be explained by cells which had not been separated. These would therefore exhibit increased fluorescence compared to single cells. This was tested by gating of the populations in the flow cytometer, but was not found to be the answer.

5.2.6 Cell cycle arrest

After analysis of the DNA histograms produced by the Flow Collect program during data collection, it appeared as though there was varying amounts of G2 arrest for different time points in experiments. This was expected as radiation induced G2 arrest has been seen in this cell line previously [67].

This mechanism was investigated using the FCS express program in order to model the cell cycle data for the histograms of PI fluorescence for each sample. Modelling of the data proved difficult, with large variations in results between the different possible models. It was suspected that this problem arose due to the other reagents used during processing these experiments.

Compared to the initial distribution of cells within the different phases of the cell cycle seen at 0.5 hours, a particular increase in G2 cells can be seen at 24 hours for the high LET position at the back of the Bragg peak and a smaller effect can be seen at the same time point for x-rays. Cells irradiated in the front of the Bragg peak appear to react slower and show an increase after in G2 arrest at 48 hours. The percentage of cells in the G2 phase for 48 and 72 hours can be seen to decrease again, to a level only slightly higher than that of 0.5 hours. Thus indicating that the normal cell cycle is resumed.

Due to the issues associated with modelling in the FCS express program, a second attempt at analysis of these plots was done in the Flow Collect program directly. This was done by gating the visible G1 and G2 peak, but as this did not account for the overlap of cell in S phase the results merely gave a rough indication of the percentages of cells in these two phases. This showed the same pattern of G2 arrest at 24 hours for high LET irradiation, therefore verifying the results obtained. The results from this analysis can be found in Appendix B.

This mechanism of arrest could explain the increase in γH2AX fluorescence seen for the later time points as discussed previously. It can be deduced that at 24 hours, after high LET irradiation, cells are arrested in G2 phase in order to facilitate the repair of complex DSBs [68]. From 48 hours it appears as though the cells have resumed proliferation. This accounts for an increase in the detected DSBs at 48 and 72 hours, due to proliferating cells passing residual damages on to their progeny [69].

5.3 Apoptosis experiment results

The low levels of apoptosis seen in these results could mean that this cell line does not undergo apoptosis. For many tumour cells, pathways such as the p53 pathway, which lead to repair or apoptosis are non functional [70]. This could be the case in these experiments, meaning that this cell assay will not give the results anticipated. This could be further investigated using different types of cell assay to investigate the mechanisms and pathways which are at work.

It was considered that these results could be used as an indication of cell survival after irradiation, by investigating the viable population of whole cells across experiments. However, a number of the control samples had a lower percentage of viable cells compared to their corresponding irradiated samples. This effect can be used as an indication of the quality of the experimental procedure used in these experiments. Poor technique when processing the cells will result in an increased amount of debris and increase loss of cells. Debris will be lost during the initial wash and trypsinisation of the dishes, throughout the different stages of the cell assay procedure and with use of the centrifuge.

Improvements in the method seen during the γH2AX assay could perhaps have accounted for some of these issues, however the low Annexin V-FITC staining efficiency is still indicative of no apoptosis. In conclusion, these experiments did not produce sufficient evidence for the induction of apoptosis in these cells.

5.4 Data Analysis

5.4.1 Flow Cytometry Analysis

Variations in detector efficiency will occur between experiments. For this reason control samples for both the antibodies were processed each day in order to calibrate the system. Sensitivity of the flow cytometer to detect foci will also vary with the flow speed. The reagents prepared had an optimal fluorescence over 2 hours, after preparation. This, plus the large number of samples to be processed at a time meant that time was somewhat limited. Therefore a higher flow speed was selected for experiments after the freezing procedure was implemented. This could lead to the combining of signals from different cells.

The heterogeneous nature of γH2AX foci, could also be an issue with this method of analysis, as the fluorescence detected may not be an accurate representation of the true number of foci. Large and small foci will coexist within the same nucleus and if these are situated close to one another their fluorescence may be counted as a single foci [56]. This effect will be particularly prominent for samples after high LET irradiation and may lead to an underestimation of the number of DSBs.

Using a second technique for analysing results, such as immunoblotting or immunofluorescence microscopy could remove some of these uncertainties. Due to the nature of manual analysis for these techniques this would provide less statistics, but a much more precise method. Manually visualising and counting the number of foci in the cell samples offers a much higher analytical sensitivity compared to flow cytometry [71]. Individual analysis of the cells could also provide a more detailed insight into the effects varying LET, such as clustering. Therefore additional experiments utilising both flow cytometry and a second, more precise, foci counting method could be beneficial.

5.4.2 LET and RBE

Variations in dose and LET values at the various positions along the proton track are of key interest in treatment planning for proton therapy. A so called spread out Bragg peak (SOBP) technique is used, which in principle is a succession of Bragg peaks spread accross the tumour volume (Section 2.2). This exploits the specific dose distribution of protons, by repeating irradiations for which the maximum of the Bragg peak is positioned at different depths within the tumour. This technique therefore ensures the full tumour receives the high doses afforded by protons, but also delivers high LET radiation to the full volume.

Clinically, an average value for RBE of 1.1 is used. This therefore averages the effect of the proton beam across the tissue with which it is interacting. However, an important effect of high LET irradiation of matter is the induction of densely clustered damages compared to lower LET radiation. It is known that higher LET results in a more clustered deposition of energy, which results in more complex damage to cells, leading to compromised repair [72]. By investigating the extent of this effect in irradiated cells it is possible to review the idea of an average RBE value for proton therapy.

It is important to note that due to the much lower energies used in this study (16 MeV) compared to the energies of clinical beams (70 - 230 MeV [73]), the LET values studied will be much higher than those in patient treatments. These higher LET values will therefore produce greater levels of damage than expected during patient treatments. Although the energies of these beams are extremely different, the relationship between the high LET and low LET effects produced will be relevant in clinical treatment planning.

RBE values can be used in order to quantitatively assess the effects of different LET radiations. The dose of a given radiation required to achieve a specified clinical endpoint, such as cell death, is compared to a second radiation dose achieving the same result. The end point in this study was seen as the induction of γH2AX fluorescence. Typically high LET radiation, such as that delivered by the back of the Bragg peak would be compared to 220 kV x-rays. However, due to the limitations of achievable x-ray dose in these experiments, this was not possible. Instead, the levels of γH2AX fluorescence induced by the high LET back of the Bragg peak was compared to that induced by the top of the Bragg peak. For the 5 Gy proton experiment the initial values of γH2AX fluorescence were very similar. Given that the dose from the back of the Bragg peak was 5 Gy, compared to 22 Gy delivered by the top of the Bragg peak, an RBE value of at least 4.4 was obtained.

It was found in our group previously that the RBE of protons in the back of the Bragg peak varied between 4 and 10. Although very similar, it is important to note that these results were calculated to x-rays and to different end points.

The γH2AX signals produced per Gy of high and low LET radiation were also compared. The ratio of high to low LET signal was found, giving values of 2.6 ± 0.5 and 2.8 ± 0.6, for 5 and 10 Gy respectively. The similarity between these values for the two doses shows a clear linearity in the signals produced. Although this ratio cannot be considered an RBE value, it is representative of the effect of LET on γH2AX phosphorylation. As the ratio is almost the same for both 5 and 10 Gy, this again emphasizes the significance of high LET effects compared to dose.

The high RBE of proton therapy is a key advantage of this treatment technique compared to x-ray therapy for achieving tumour control [74]. However, the clinical value used is only 1.1, which is most likely an underestimation of the effects produced by protons. This could lead to serious implications for patients [75]. The present results, even though they were obtained with a much lower energy, would suggest the need for a much higher average RBE value than the 1.1 being used today.

The possibility to incorporate LET optimisation into treatment planning is becoming increasingly plausible [2]. However, more extensive research into the potential benefits are needed to justify the introduction of LET or RBE-based treatment plans.

5.4.3 Cell Survival

With data taken from previous clonogenic cell survival studies at UiO [6] it is possible to compare the damages induced and repaired in these cells to the expected survival levels (5.1). These results showed drastically reduced cell survival after proton irradiations in the back of the Bragg peak compared to both x-ray and low LET proton irradiation. Cell survival was found to decrease from 7 % in the front of the Bragg peak to just 0.08 % in the back of the Bragg peak for 5 Gy irradiation. For x-ray irradiation at this dose, the cell survival was 50 %.

This correlates to the increased initial number of DSBs seen for high LET protons irradiated in the back of the Bragg peak, compared to the other types of irradiation, as shown by detected γH2AX fluorescence (fig 4.5a).

5.4.4 Future Considerations

Ideally, it would be possible to directly measure the actual dose given to the cell samples at OCL, this would allow for a drastic improvement in both the reproducibility and reliability of the results obtained.

Previously at UiO, the method of using γH2AX assays for DSB detection was only used with the T-47D cell line. Therefore it would be beneficial to perform additional experiments testing the effects of varying γH2AX concentrations over time with the T98G cell line. This could perhaps show an optimal amount of the antibody to be used with this cell line in order to discount the theory of saturation completely.

In order to further investigate the pathways at work resulting in the loss of cells after irradiation it would be useful to investigate alternative pathways or an alternative cell line. Repeating these experiments on a cell line which is known to undergo apoptosis would allow a comparison of DSB induction compared to cell death. This would give a greater insight into the mechanisms behind cell survival after irradiation.

The arrest of these cells in the G2 phase could be investigated more thoroughly with an experiment dedicated to this mechanism. The resultant histograms for PI uptake from these experiments will not be as precise as for experiments performed solely with PI. This is due to the other reagents, used in the processing and staining of the cells, for the γH2AX assay. The Vindelov method is widely used in flow cytometry in order to examine the DNA profiles in the nuclei of cells [76, 77]. As the quality of the histograms produced is vital for the use of the FSC program for analysis, a more specific experiment could greatly improve the accuracy of the results. It would also be beneficial to develop a more effective method for analysis of the histograms, to reduce the human error associated with the results obtained.

In order to calculate more accurate values for the RBE of protons at different LET positions, a comparison to x-ray fluorescence would be optimal. From these results it can be deduced that much higher doses of x-ray irradiation would be required in order to achieve comparable levels of γH2AX fluorescence. Therefore a method of delivering high doses of x-ray irradiation, without compromising the cells, could be extremely beneficial to this research.

Chapter 6

Conclusion

A successful study into effects of varying LET on the induction of DSBs and repair of T98G cells after proton and x-ray irradiation was performed. The irradiation of cells was investigated at three different positions, with varying LET values, along the proton track. The experimental procedure for γH2AX cell assay was adapted over the course of this project in order to optimise the detection of DNA DSBs. As expected, T98G cells showed increased levels of γH2AX phosphorylation after high LET irradiation compared to low LET irradiation at the same doses.

From these findings, an RBE value of at least 4.4 was found to describe the differences in effect seen by irradiation in the back of the Bragg peak (LET = 38 - 44 keV/μm) compared to the top (LET = 23 - 28 keV/μm). Further investigations into these values for different cell lines, after irradiation with various LET values, would enable improved predictions for the variation of RBE. This could allow for improved treatment planning for patients in the future.

A ratio for the amount of damage induced for high LET irradiation compared to low LET irradiation was also found. After 5 Gy this was found to be 2.6 $\pm$ 0.5 compared to 2.8 $\pm$ 0.6 for 10 Gy. These values demonstrate how much more damage is induced by the higher LET in the back of the Bragg peak compared to the front of the Bragg peak.

An unexpected finding was the increase in γH2AX fluorescence seen at 72 hours. The potential reasons behind this have been discussed and could be further investigated. Flow cytometric analysis of the DNA content in the different phases of the cell cycle revealed a distinct arrest of cells in G2 phase at 24 hours post irradiation. This was particularly significant for cells irradiated with higher LET values.

Contrary to expectations, it was found that this line of T98G cells do not undergo apoptosis. A different cell line should therefore be used for future studies in order to determine a relationship between this mechanism of cell death and the induction of DSBs after irradiation.

Bibliography

1. (PTCOG), P. T. C.-O. G. *Particle therapy facilities in operation. @ONLINE* `https://www.ptcog.ch/index.php/facilities-in-operation`.
2. Haas-Kogan, D. *et al.* National Cancer Institute Workshop on Proton Therapy for Children: Considerations Regarding Brainstem Injury. *International Journal of Radiation Oncology*Biology*Physics* **101,** 152–168. ISSN: 0360-3016 (2018).
3. M., L. M., M., M. S. & A., T. S. Proton therapy for central nervous system tumors in children. *Pediatric Blood & Cancer* **65,** e27046.
4. Kjellberg, R. N., Davis, K. R., Lyons, S., Butler, W. & Adams, R. D. Bragg Peak Proton Beam Therapy for Arteriovenous Malformation of the Brain. *Neurosurgery* **31,** 248–290 (1984).
5. Kleihues, P. & K. Cavenee, W. Pathology and genetics of tumors of the nervous system (Jan. 2000).
6. Rykkelid, A. M. Method for in vitro cell irradiation with low energy protons (Nov. 2017).
7. Paganetti, H. *et al.* Relative biological effectiveness (RBE) values for proton beam therapy. *International Journal of Radiation Oncology*Biology*Physics* **53,** 407–421. ISSN: 0360-3016 (2002).
8. Panawala, L. Difference Between Chromosome and Chromatid (Feb. 2017).
9. Et al., B. A. *Molecular Biology of The Cell 6th Edition* (Garland Science, Taylor and Francis Group, 2015).

10. Bortfeld, T. & Schlegel, W. An analytical approximation of depth-dose distributions for therapeutic proton beams. **41,** 1331–9 (Sept. 1996).

11. Frame, P. *Coolidge X-ray Tubes* `https:/www.orau.org/ptp/collection/xraytubescoolidge/coolidgeinformation.htm`. (accessed: 12.05.2018).

12. Attix, F. H. *Introduction to Radiological Physics and Radiation Dosimetry* (John Wiley and Sons, Inc., 1986).

13. Podgorsak, E. *Radiation Oncology Physics: A Handbook for Teachers and Students* `https://www-pub.iaea.org/mtcd/publications/pdf/pub1196$%5C_$web.pdf` (2005). (accessed: 12.05.2018).

14. El-Saftawy, A. *Regulating the performance parameters of accelerated particles* `https://www.researchgate.net/publication/280722233$%5C_$Regulating$%5C_$the$%5C_$performance$%5C_$parameters$%5C_$of$%5C_$accelerated$%5C_$particles`. (accessed: 12.05.2018).

15. (https://physics.stackexchange.com/users/23816/denver-dang), D. D. *Dose-depth curve of photons vs. protons* `https://physics.stackexchange.com/q/169665`.

16. J Wilkens, J. & Oelfke, U. Three-dimensional LET calculations for treatment planning of proton therapy. **14,** 41–6 (Feb. 2004).

17. J., W. J. & Uwe, O. Analytical linear energy transfer calculations for proton therapy. *Medical Physics* **30,** 806–815.

18. Wilkens, J. & Oelfke, U. A phenomenological model for the relative biological effectiveness in therapeutic proton beams. **49,** 2811–25 (Aug. 2004).

19. Wouters B. G., e. a. Measurements of Relative Biological Effectiveness of the 70 MeV Proton Beam at TRIUMF Using Chinese Hamster V79 Cells and the High-Precision Cell Sorter Assay. *Radiation Research.* **146,** 159fffdfffdfffd170 (1996).

20. Zuofeng, L. Prescribing, Recording, and Reporting Proton-Beam Therapy. *International Journal of Radiation Oncology Biology Physics* **73.** doi:`10.1016/j.ijrobp.2008.10.084` (2009).

21. M., K. F. *et al.* Clinical electronfffdfffdfffdbeam dosimetry: Report of AAPM Radiation Therapy Committee Task Group No. 25. *Medical Physics* **18,** 73–109.

22. Hall, E. J. & Giaccia, A. J. *Radiobiology for the Radiologist, Seventh Edition* (Lippincott Williams and Wilkins, 2012).

23. Feinendegen, L. E. Biological damage from the Auger effect, possible benefits. *Radiation and Environmental Biophysics* **12,** 85–99. ISSN: 1432-2099 (June 1975).

24. Hofer, K. G. e. a. Biological toxicity of Auger emitters: molecular fragmentation versus electron irradiation. *Current Topics in Radiation Research.* **12,** 335–354 (1978).

25. Wfffdfffdra, A.-C., Heuskin, A.-C., Riquier, H., Michiels, C. & Lucas, S. Low-LET Proton Irradiation of A549 Non-small Cell Lung Adenocarcinoma Cells: Dose Response and RBE Determination. **179** (Jan. 2013).

26. Weyemi, U. S. *et al. Histone H2AX deficiency causes neurobehavioral deficits and impaired redox homeostasis* in *Nature Communications* (2018).

27. D.M.S., P. & A., F. Structure and Function of Histone H2AX. *Subcellular Biochemistry* **50,** 55–78 (Dec. 2009).

28. Pinto, D. M. S. & Flaus, A. in *Genome Stability and Human Diseases* (ed Nasheuer, H.-P.) 55–78 (Springer Netherlands, Dordrecht, 2010). ISBN: 978-90-481-3471-7. doi:`10.1007/978-90-481-3471-7_4`. `https://doi.org/10.1007/978-90-481-3471-7_4`.

29. Bedford, J. S. Sublethal damage, potentially lethal damage, and chromosomal aberrations in mammalian cells exposed to ionizing radiations. *International Journal of Radiation Oncology*Biology*Physics* **21,** 1457–1469. ISSN: 0360-3016 (1991).

30. Harms-Ringdahl, M., Nicotera, P. & Radford, I. R. Radiation induced apoptosis. *Mutation Research/Reviews in Genetic Toxicology* **366.** Special Issue Radiation Induced Chromosomal Aberrations, 171–179. ISSN: 0165-1110 (1996).

31. Verheij, M. & Bartelink, H. Radiation-induced apoptosis. *Cell and Tissue Research* **301,** 133–142. ISSN: 1432-0878 (July 2000).

32. Zheng, H. & Chen, J. Abstract 1772: p53 promotes repair of heterochromatin DNA by regulating JMJD2b and SUV39H1 expression. *Cancer Research* **73,** 1772–1772. ISSN: 0008-5472 (2013).

33. Zhao, J. *et al.* pATM and fffdfffdH2AX are effective radiation biomarkers in assessing the radiosensitivity of 12C6+ in human tumor cells. **17** (Dec. 2017).

34. Gelot, C., Magdalou, I. & Lopez, B. S. Replication Stress in Mammalian Cells and Its Consequences for Mitosis. *Genes* **6,** 267–298. ISSN: 2073-4425 (2015).

35. Dikomey, E. & Franzke, J. DNA repair kinetics after exposure to X-irradiation and to internalβ-rays in CHO cells. *Radiation and Environmental Biophysics* **25,** 189–194. ISSN: 1432-2099 (Sept. 1986).

36. Short, S. C. *et al.* DNA repair after irradiation in glioma cells and normal human astrocytes. *Neuro-oncology* **9 4,** 404–11 (2007).

37. Frankenberg-Schwager, M. Review of repair kinetics for DNA damage induced in eukaryotic cells in vitro by ionizing radiation. *Radiotherapy and oncology : journal of the European Society for Therapeutic Radiology and Oncology* **14 4,** 307–20 (1989).

38. Symonds, H. *et al.* p53-Dependent apoptosis suppresses tumor growth and progression in vivo. *Cell* **78,** 703–711. ISSN: 0092-8674 (1994).

39. Lowe, S. *et al.* p53 status and the efficacy of cancer therapy in vivo. *Science* **266,** 807–810. ISSN: 0036-8075 (1994).

40. V Williams, M., Denekamp, J. & F Fowler, J. A review of alpha/beta ratios for experimental tumors: Implications for clinical studies of altered fractionation. **11,** 87–96 (Feb. 1985).

41. J Eblan, M., A Vanderwalde, N., Zeman, E. & Jones, E. Hypofractionation for breast cancer: Lessons learned from our neighbors to the north and across the pond. **28,** 536–46 (June 2014).

42. Scientific, T. F. *How a Flow Cytometer Works* `https://www.thermofisher.com/no/en/home/life-science/cell-analysis/cell-analysis-learning-center/molecular-probes-school-of-fluorescence/flow-cytometry-basics/flow-cytometry-fundamentals/how-flow-cytometer-works.html`.
43. Srivastava, N., Gochhait, S., de Boer, P. & Bamezai, R. N. Role of H2AX in DNA damage response and human cancers. *Mutation Research/Reviews in Mutation Research* **681,** 180–188. ISSN: 1383-5742 (2009).
44. Martin, O., Rogakou, E., Panyutin, I. & M Bonner, W. Quantitative Detection of 125 IdU-Induced DNA Double-Strand Breaks with fffdfffd-H2AX Antibody. **158,** 486–92 (Nov. 2002).
45. Chassot, A.-A. *et al.* Confluence-induced cell cycle exit involves pre-mitotic CDK inhibition by p27Kip1 and cyclin D1 downregulation. *Cell Cycle* **7.** PMID: 18604165, 2038–2046 (2008).
46. Hannan, K. *et al.* RNA polymerase I transcription in confluent cells: Rb downregulates rDNA transcription during confluence-induced cell cycle arrest. **19,** 3487–97 (Aug. 2000).
47. Baird, T. T., Jr. & Craik, C. S. in *Handbook of Proteolytic Enzymes* (eds Rawlings, N. D. & Salvesen, G.) 2594–2600 (Academic Press, 2013). ISBN: 978-0-12-382219-2. doi:`https://doi.org/10.1016/B978-0-12-382219-2.00575-5`. `https://www.sciencedirect.com/science/article/pii/B9780123822192005755`.
48. Capuano, P. & Capasso, G. [The importance of intracellular pH in the regulation of cell function]. *Giornale italiano di nefrologia : organo ufficiale della Societa italiana di nefrologia* **20,** 139fffdfffdfffd150. ISSN: 0393-5590 (2003).
49. Dahle, T. J. *et al.* Monte Carlo simulations of a low energy proton beamline for radiobiological experiments. *Acta Oncologica* **56.** PMID: 28464743, 779–786 (2017).

50. Edin, N. J., Olsen, D. R., Sandvik, J. A., Malinen, E. & Pettersen, E. O. Low dose hyper-radiosensitivity is eliminated during exposure to cycling hypoxia but returns after reoxygenation. *International Journal of Radiation Biology* **88,** 311–319 (2012).

51. Huang, X. & Darzynkiewicz, Z. Cytometric Assessment of Histone H2AX Phosphorylation: A Reporter of DNA Damage. *Methods in molecular biology* **314,** 73fffdfffdfffd80 (2006).

52. Shibata, A. & Jeggo, P. DNA Double-strand Break Repair in a Cellular Context. *Clinical Oncology* **26.** Advances in Clinical Radiobiology (Part 2), 243–249. ISSN: 0936-6555 (2014).

53. Martin, O., Rogakou, E., Panyutin, I. & M Bonner, W. Quantitative Detection of 125 IdU-Induced DNA Double-Strand Breaks with fffdfffd-H2AX Antibody. **158,** 486–92 (Nov. 2002).

54. K. Psonka-Antonczyk Th. Elsaesser, E. G.-N. & Taucher-Scholz, G. Distribution of Double-Strand Breaks Induced by Ionizing Radiation at the Level of Single DNA Molecules Examined by Atomic Force Microscopy. *Radiation Research* **172,** 288–295. ISSN: 3 (2009).

55. Banáth, J. P., MacPhail, S. H. & Olive, P. L. Radiation Sensitivity, H2AX Phosphorylation, and Kinetics of Repair of DNA Strand Breaks in Irradiated Cervical Cancer Cell Lines. *Cancer Research* **64,** 7144–7149. ISSN: 0008-5472 (2004).

56. Neumaier, T. *et al.* Evidence for formation of DNA repair centers and dose-response nonlinearity in human cells. *Proceedings of the National Academy of Sciences* **109,** 443–448. ISSN: 0027-8424 (2012).

57. Kinner, A., Wu, W., Staudt, C. & Iliakis, G. fffdfffd-H2AX in recognition and signaling of DNA double-strand breaks in the context of chromatin. *Nucleic Acids Research* **36,** 5678–5694 (2008).

58. Burdak-Rothkamm, S., Short, S. C., Folkard, M., Rothkamm, K. & Prise, K. M. ATR-dependent radiation-induced fffdfffdH2AX foci in bystander primary human astrocytes and glioma cells. *Oncogene* **26,** 993–1002 (2007).

59. Kawamura, K., Qi, F. & Kobayashi, J. Potential relationship between the biological effects of low-dose irradiation and mitochondrial ROS production. *Journal of Radiation Research* **59,** ii91–ii97 (2018).

60. I Azzam, E., Jay-Gerin, J.-P. & Pain, D. Ionizing radiation-induced metabolic oxidative stress and prolonged cell injury. **327,** 48–60 (Dec. 2011).

61. Shimura, T. *et al.* A comparison of radiation-induced mitochondrial damage between neural progenitor stem cells and differentiated cells. *Cell Cycle* **16.** PMID: 28118061, 565–573 (2017).

62. Yamamori, T. *et al.* Ionizing radiation induces mitochondrial reactive oxygen species production accompanied by upregulation of mitochondrial electron transport chain function and mitochondrial content under control of the cell cycle checkpoint. *Free Radical Biology and Medicine* **53,** 260–270. ISSN: 0891-5849 (2012).

63. Lorimore, S. A. & Wright, E. G. Radiation-induced genomic instability and bystander effects: related inflammatory-type responses to radiation-induced stress and injury? A review. *International Journal of Radiation Biology* **79,** 15–25 (2003).

64. A Lorimore, S., Coates, P. & G Wright, E. Radiation-induced genomic instability and bystander effects: Inter-related nontargeted effects of exposure to ionizing radiation. **22,** 7058–69 (Nov. 2003).

65. Little, J. B., Nagasawa, H., Pfenning, T. & Vetrovs, H. Radiation-Induced Genomic Instability: Delayed Mutagenic and Cytogenetic Effects of X Rays and Alpha Particles. *Radiation Research* **148,** 299–307. ISSN: 00337587, 19385404 (1997).

66. Ward, I. M. & Chen, J. Histone H2AX Is Phosphorylated in an ATR-dependent Manner in Response to Replicational Stress. *Journal of Biological Chemistry* **276,** 47759–47762 (2001).

67. Kiseleva, L. N., Kartashev, A. V., Vartanyan, N. L., Pinevich, A. A. & Samoilovich, M. P. The Effect of Fotemustine on Human Glioblastoma Cell Lines. *Cell and Tissue Biology* **12,** 93–101. ISSN: 1990-5203 (Mar. 2018).

68. Shibata, A. *et al.* Factors determining DNA double-strand break repair pathway choice in G2 phase. *The EMBO Journal* **30,** 1079–1092. ISSN: 0261-4189 (2011).

69. Aypar, U., F Morgan, W. & Baulch, J. Radiation-induced genomic instability: Are epigenetic mechanisms the missing link? **87,** 179–91 (Nov. 2010).

70. Venere, M., De, K., Yoo, J. Y. & Kaur, B. in *Handbook of Brain Tumor Chemotherapy, Molecular Therapeutics, and Immunotherapy (Second Edition)* (ed Newton, H. B.) Second Edition, 291–303 (Academic Press, 2018). ISBN: 978-0-12-812100-9. doi:`https://doi.org/10.1016/B978-0-12-812100-9.00020-6`. `https://www.sciencedirect.com/science/article/pii/B9780128121009000206`.

71. Rothkamm, K. & Horn, S. Gamma-H2AX as protein biomarker for radiation exposure. **45,** 265–71 (Jan. 2009).

72. Asaithamby, A., Hu, B. & Chen, D. J. Unrepaired clustered DNA lesions induce chromosome breakage in human cells. *Proceedings of the National Academy of Sciences of the United States of America* **108 20,** 8293–8 (2011).

73. NHS. *How Proton Beam Therapy is Delivered.* `http://www.christie.nhs.uk/services/i-to-q/protons/how-proton-beam-therapy-is-delivered/`.

74. Durante, M. & S Loeffler, J. Charged particles in radiation oncology. **7,** 37–43 (Dec. 2009).

75. Jones, B., McMahon, S. & Prise, K. The Radiobiology of Proton Therapy: Challenges and Opportunities Around Relative Biological Effectiveness. *Clinical Oncology* **30.** Proton Beam and Particle Therapy, 285–292. ISSN: 0936-6555 (2018).

76. Vindelfffdfffdv, L. & Christensen, I. J. in *Flow Cytometry* (eds Darzynkiewicz, Z. & Crissman, H. A.) 127–137 (Academic Press, 1990). doi:`https://doi.org/10.1016/S0091-679X(08)60519-1`. `http://www.sciencedirect.com/science/article/pii/S0091679X08605191`.

77. Krueger, S. A. & Wilson, G. D. in *Cancer Cell Culture: Methods and Protocols* (ed Cree, I. A.) 359–370 (Humana Press, Totowa, NJ, 2011). ISBN: 978-1-61779-080-5. doi:`10.1007/978-1-61779-080-5_29`. `https://doi.org/10.1007/978-1-61779-080-5_29`.

Appendix A

Method

A.1 γH2AX Assay

1. Spin down the samples at 1400 rpm for 4 minutes
2. Wash cells once with 1 mL of Wash Buffer
3. Spin down cells at 1400 rpm for 4 minutes and discard buffer
4. Resuspend cells in 250 μL of Fixation Buffer
5. Incubate for 20 minutes on ice
6. Spin down cells at 1400 rpm for 4 minutes and discard buffer
7. Resuspend cells in 500 μL of Assay buffer
8. Spin down cells at 1400 rpm for 4 minutes and discard buffer
9. Add 250 μL of Permeabilisation Buffer and incubate on ice for 20 minutes
10. Spin down cells at 1400 rpm for 4 minutes and discard buffer
11. Wash cells with 5 mL of Assay Buffer
12. Spin down cells at 1400 rpm for 4 minutes and discard buffer
13. Repeat last two steps twice more - three washes in total
14. Resuspend cells in 95 μL of Assay Buffer and add 5 μL Anti-Histone H2A.X-Alexa Fluor 488 to each sample
15. Incubate cells for 30 minutes in the dark at room temperature
16. Add 100 μL of Assay Buffer to the 100 μL of antibody stained cells
17. Spin down cells at 1400 rpm for 4 minutes and discard supernatant
18. Wash with 1 mL of Assay buffer

19. Spin down cells at 1400 rpm for 4 minutes and discard buffer
20. Resuspend cells in 500 μL of 1X Assay buffer
21. Filter samples into flasks suitable for flow cytometry
22. Perform flow cytometry analysis

A.2 Apoptosis Assay

10 microliters of 10X Binding buffer, 10 microliters of PI, 1 microliter of Annexin V-FITC, 79 microliters MilliQ water Reagent is stable for at least 2 hours

Flow Cytometry Procedure

1. 3ml of medium into flasks
2. Medium removed from the irradiated cells
3. Washed with 1.5ml of Trypsin, which is then removed
4. 3ml of Trypsin added, left to stand for around 5 minutes, washed around flask using small pipette
5. Checked in microscope for sufficient amount single cells
6. Contents of dish transferred into the flask containing fresh medium
7. Centrifuge and begin cell assay procedure as shown in Appendix A.1

1. Trypsinize + Medium (1.5ml, 3ml + 3ml medium)
2. Centrifuge 1400 rpm for 4 minutes
3. Wash once in 500 microliters of PBS, centrifuge
4. 400 microliters of Binding buffer per sample
5. 100 microliters of Annexin V incubation reagent - per samples of 10^5 to 10^6 cells
6. Gently resuspend cells in the Annexin V Incubation Reagent at a concentration of 10^5 to 10^6 per 100 microliters prepared
7. Incubate in the dark for 15 minutes at room temperature
8. Add 400 microliters 1X Binding buffer to samples (per 100 microliters reaction)
9. Filter into flow cytometer vials
10. Process within one hour for maximal signal

A.3 Cell Barcoding

For experiments in which fluorescent cell barcoding was used the procedure below was followed for the staining of the flasks of control cells.

Using 0.6 μl/ml for barcoding - 45 μl of stocksolution added to each of the FF-samples To prepare - 50 μg is dissolved into 200 μl DMSO - divided into vials containing 10 μl. Then stored in the -80 degree freezer until needed. To prepare flasks, 3.6 μl from a frozen vial is added into 50 μl of DMSO 45 μl of this mixture is then added to the prepared FF samples.

1. Prepare labelled vials containing 5 ml of fresh medium and keep on ice before removing samples from the incubator
2. Remove flask from incubator and remove medium with a pipette
3. 5 ml of Trypsin added to the flask and allowed to incubate for around 5 minutes, in this time use a pipette to ensure the Trypsin is fully distributed around the flask and to begin separating the cells
4. Check the flask to determine the separation of the cells into single cells, gently pipette to ensure the maximum number of single cells
5. Remove from the flask and add to a labelled tube containing 5 ml of cold, fresh medium
6. Immediately spin down at 1400 rpm for 4 minutes.
7. Wash with 3 ml of PBS
8. Spin down and remove supernatant before adding 750 l of Fixation buffer
9. Incubate for 20 minutes on ice
10. Spin down
11. Wash with with 1.5 ml of PBS
12. Spin down
13. Add 750 μl of Permeabilisation buffer
14. Incubate for at least 5 minutes
15. Add 45 μl of dye mixture, vortex
16. Add 750 μl of PBS
17. Incubate for 30 minutes on ice

18. Wash 3 x with 1.5 ml of Assay Buffer
19. Add 300 μl of H2AX mix
20. Incubate for 30 in the dark at room temperature
21. Add 300 μl of Assay Buffer to sample
22. Spin down
23. Wash with 750 μl Assya Buffer
24. Spin down and remove supernatant
25. Resuspend in 1.5 ml of PI mixture
26. Incubate for around 30 minutes in the dark before filtering
27. Add 50 μl to samples

Appendix B

Additional Results

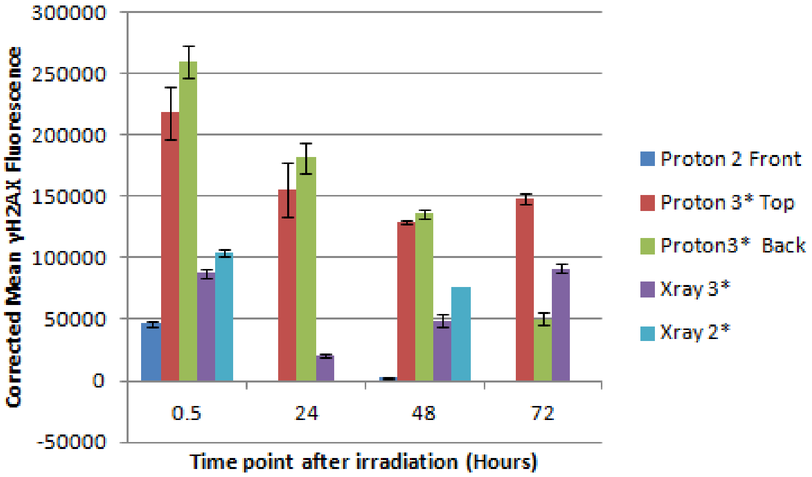

Figure B.1: Mean values of γH2AX fluorescence at different time points after irradiation with 5 Gy.

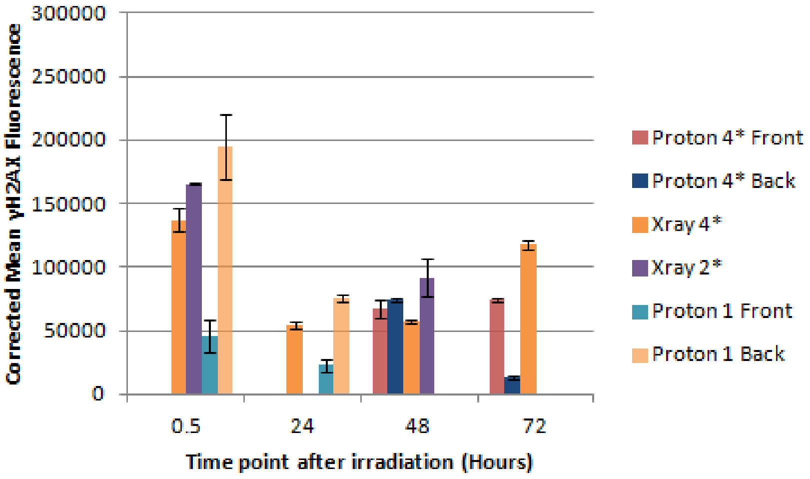

Figure B.2: *Mean values of γH2AX fluorescence at different time points after irradiation with 10 Gy.*

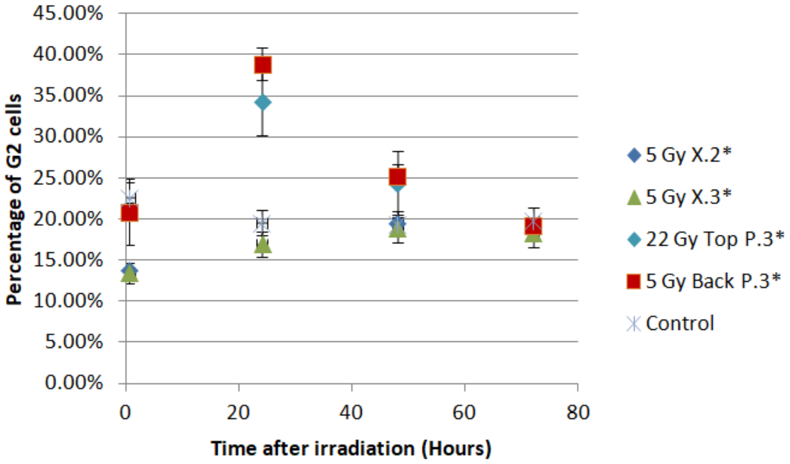

Figure B.3: *Values for G2 arrest obtained by manual gating of the DNA histograms in the flow collect program.*

Appendix C

Annexin V-FITC Assay

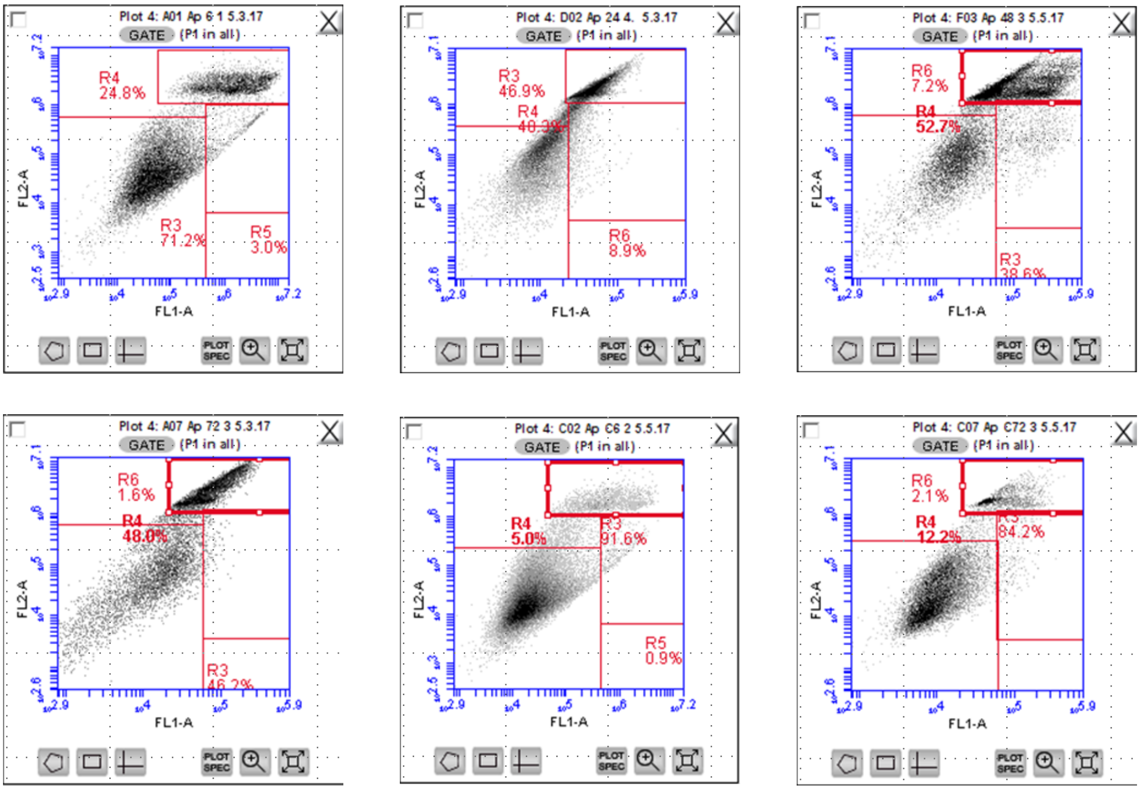

Figure C.1: *Attempts at gating flow cytometry results from the Annexin V FITC apoptosis assay*

Due to the drifting in the channels colour compensation was attempted in order to separate the populations more clearly. Due to the manual nature of this method the results were not considered reproducible and were therefore abandoned.

			Whole cells		Low PI		High PI	
Radiation	Time (H)	Whole cells (%)	High PI (%)	Low PI (%)	V (%)	EA (%)	LA (%)	N (%)
Control	6	74.7 ± 4.5	4.6 ± 0.2	91.9 ± 1.0	99.8 ± 0.0	0.4 ± 1.0	38.9 ± 9.4	62.7 ± 8.8
P Front	6	82.1 ± 1.3	4.2 ± 2.1	93.3 ± 2.5	99.9 ± 0.0	0.1 ± 2.5	19.8 ± 11.0	80.7 ± 10.7
P Back	6	83.2 ± 2.2	3.2 ± 1.2	95.1 ± 1.1	99.9 ± 0.1	0.2 ± 1.1	28.8 ± 4.2	72.4 ± 4.1
Control	24	57.6 ± 5.1	10.7 ± 2.0	87.1 ± 1.8	99.9 ± 0.1	0.1 ± 1.8	29.1 ± 6.5	71.7 ± 5.9
P Front	24	71.2 ± 0.6	5.3 ± 1.1	91.4 ± 1.0	99.9 ± 0.0	0.1 ± 1.0	29.6 ± 2.5	70.4 ± 2.5
P Back	24	75.6 ± 3.5	3.8 ± 1.2	94.6 ± 1.2	99.9 ± 0.0	0.2 ± 1.2	40.4 ± 4.5	60.0 ± 5.0
Control	48	79.2 ± 2.9	5.2 ± 1.6	92.2 ± 2.0	100.0 ± 0.0	0.0 ± 2.0	37.5 ± 5.8	63.8 ± 5.4
P Front	48	71.3 ± 4.0	8.5 ± 1.8	88.6 ± 1.5	100.0 ± 0.0	0.0 ± 1.5	25.3 ± 11.8	75.7 ± 11.5
P Back	48	76.6 ± 2.2	2.9 ± 0.4	95.5 ± 0.3	100.0 ± 0.0	0.1 ± 0.3	46.8 ± 5.6	54.0 ± 6.1
Control	72	76.3 ± 4.2	4.8 ± 1.3	93.8 ± 1.3	100.0 ± 0.0	0.1 ± 1.3	42.2 ± 4.0	59.9 ± 3.8
P Front	72	69.2 ± 2.7	10.7 ± 1.5	87.3 ± 1.6	100.0 ± 0.0	0.0 ± 1.6	21.7 ± 5.7	79.4 ± 5.8
P Back	72	77.5 ± 2.3	5.7 ± 0.3	93.0 ± 0.3	100.0 ± 0.0	0.1 ± 0.3	39.6 ± 5.8	61.1 ± 6.4

Table C.1: *Tabulated values for percentage of viable cells remaining after 5 Gy irradiation. Values shown are the average percentage of whole cells in each sample with low PI uptake. Errors are the values of standard deviation for each data set.*

			Whole cells		Low PI		High PI	
Radiation	Time (H)	Whole cells (%)	High PI (%)	Low PI (%)	V (%)	EA (%)	LA (%)	N (%)
Control	6	64.1 ± 5.5	6.5 ± 1.2	90.3 ± 1.6	99.2 ± 0.3	0.9 ± 1.6	78.5 ± 6.5	22.5 ± 6.3
P Front	6	31.72 ± 25.8	29.1 ± 20.3	68.8 ± 21.6	94.2 ± 6.8	6.0 ± 21.6	83.1 ± 25.3	17.8 ± 26.0
P Back	6	50.2 ± 7.7	15.5 ± 1.4	84.0 ± 1.4	98.6 ± 0.4	1.6 ± 1.4	69.2 ± 3.5	30.8 ± 3.5
P Front	24	44.1 ± 4.0	34.3 ± 7.8	63.4 ± 7.5	100.0 ± 0.0	0.0 ± 7.5	0.00 ± 0.0	100.0 ± 0.00
P Back	24	39.0 ± 14.7	23.9 ± 5.4	73.5 ± 6.5	100.0 ± 0.0	0.0 ± 6.5	0.0 ± 0.0	100.0 ± 0.0
P Front	48	34.5 ± 10.1	41.7 ± 20.0	56.5 ± 20.0	96.1 ± 3.3	4.2 ± 20.0	20.8 ± 5.0	77.1 ± 4.1
P Back	48	28.0 ± 8.8	55.2 ± 6.2	44.5 ± 6.1	93.4 ± 3.1	7.2 ± 6.1	30.4 ± 9.5	72.6 ± 9.3
Control	72	65.3 ± 4.1	11.6 ± 0.3	88.5 ± 0.3	99.3 ± 0.1	0.8 ± 0.3	8.3 ± 0.7	93.7 ± 0.7
P Front	72	22.7 ± 5.3	52.5 ± 1.2	46.9 ± 1.2	99.9 ± 0.1	0.2 ± 1.2	6.0 ± 1.5	95.6 ± 1.1
P Back	72	16.7 ± 4.2	49.6 ± 2.8	49.7 ± 3.0	99.6 ± 0.3	0.5 ± 3.0	8.1 ± 1.0	94.0 ± 0.8
Control	3	37.3 ± 3.6	24.2 ± 0.3	70.3 ± 0.9	100.0 ± 0.1	0.1 ± 0.9	65.5 ± 3.1	34.5 ± 3.1
X-ray	3	33.9 ± 1.8	24.5 ± 3.8	72.4 ± 3.8	99.8 ± 0.1	0.3 ± 3.8	37.7 ± 4.1	63.3 ± 4.1
Control	24	39.6 ± 2.0	13.8 ± 1.0	81.5 ± 1.4	99.8 ± 0.0	0.1 ± 1.4	39.3 ± 24.0	51.8 ± 9.1
X-ray	24	38.4 ± 6.3	15.1 ± 3.9	79.5 ± 5.1	99.8 ± 0.1	0.2 ± 5.1	73.0 ± 18.5	25.7 ± 20.0
Control	48	43.4 ± 4.3	16.1 ± 1.0	76.6 ± 2.5	99.8 ± 0.0	0.2 ± 2.5	57.7 ± 11.8	42.3 ± 11.8
Control	3	37.3 ± 3.6	24.2 ± 0.3	70.3 ± 0.9	100.0 ± 0.1	0.1 ± 0.9	65.5 ± 3.1	34.5 ± 3.1
X-ray	3	34.0 ± 1.8	24.5 ± 3.8	72.4 ± 3.8	99.8 ± 0.1	0.3 ± 3.8	37.7 ± 4.1	63.3 ± 4.1
Control	24	39.6 ± 2.0	13.8 ± 1.0	81.5 ± 1.4	99.8 ± 0.0	0.1 ± 1.4	39.3 ± 24.0	51.8 ± 9.1
X-ray	24	38.4 ± 6.3	15.1 ± 3.9	79.5 ± 5.1	99.8 ± 0.1	0.2 ± 5.1	73.0 ± 18.5	25.7 ± 20.0
Control	48	43.4 ± 4.3	16.1 ± 1.0	76.6 ± 2.5	99.8 ± 0.0	0.2 ± 2.5	57.7 ± 11.8	42.3 ± 11.8

Table C.2: *Tabulated values for percentage of viable cells remaining after 10 Gy irradiation. Values shown are the average percentage of whole cells in each sample with low PI uptake. Errors are the values of standard deviation for each data set.*

Appendix D

Dosimetry

In order to determine the homogeneity of the beam for each proton experiment, EBT3 Gafchromic films were irradiated and the resultant exposure was converted into dose values as tabulated below. The small error values seen indicate an acceptable level of homogeneity in proton experiments.

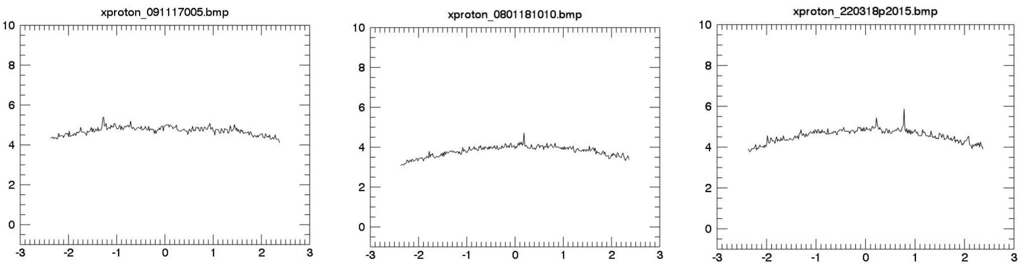

(a) *Film results irradiated 5.05.17* (b) *Film results irradiated 9.11.17* (c) *Film results irradiated 22.03.18*

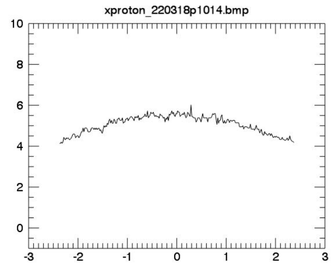

(d) *Film results irradiated 23.03.18*

Figure D.1: *Scanned EBT3 Dosimetry films*

Dose calculation

Date	Dose (Gy)
5.05.17	4.82 ± 0.52
9.11.17	3.69 ± 0.32
22.03.18	4.63 ± 0.56
23.03.18	5.05 ± 0.38

Table D.1: *Tabulated results for the average dose to EBT3 Gafchromic film used as a test of beam homogeneity in the front of the Bragg peak. Each dose represents the average dose delivered with its standard deviation. Variations in dose value are due to the dose rate and time of irradiation.*

$$Dose \quad rate = \frac{M.C}{I.C \times 1.411} \tag{D.0.1}$$

Date	Dose (Gy)	Pos. 1 (cm)	Monitor units 1 (μC)	Pos. 2 (cm)	Monitor units 2 (μC)
5.05.17	10	114 (PF)	4820	114 (L)	5090
9.11.17	5	104.5 (PF)	4350	104.5 (L)	4648
22.03.18	10	83.9 (PF)	3050	93.5 (L)	3050
23.03.18	5	95.7 (PF)	6280	95.7 (L)	6490

Table D.2: *Tabulated results of positions of irradiation for each proton experiment used for final data analysis. Position 1 describes the front of the Bragg peak (and the top of the Bragg peak for 22.03.18). Position 2 describes the back of the Bragg peak. Use of parafilm to cover the dish is denoted by (PF) while dish lids are denoted by (L). Monitor chamber units are the desired numbers to deliver the dose expected.*

Where M.C is the monitor chamber reading (units), I.C is the ionisation chamber reading (units) and 1.411 is the dose calibration constant for the ionisation chamber.

D.1 Finding the Bragg peak

Water equivalent thickness (WET) was used to normalise the distance in air and thickness of absorbers as this value is biologically the most relevant. For each proton experiment the position of the bragg peak was determined, by measuring the dose to the ionisation chamber at different distances from the beam exit window and using various thicknesses of absorber. The following tables show the raw data, taken from the ionisation chamber and monitor chamber readings. Along with the measured distance from the beam exit window, time of irradiation and thickness of absorber. These have been used to calculate the dose rate per minute. Care was taken to closely match the monitor chamber readings for dose rate for the three positions in order to minimise potential errors.